



NAVAL POSTGRADUATE SCHOOL

MONTEREY, CALIFORNIA

THESIS

**MODTRAN RADIANCE MODELING OF MULTI-ANGLE
WORLDVIEW-2 IMAGERY**

by

Samuel I. Marshall

September 2013

Thesis Co-Advisors:

Richard C. Olsen
Fred A. Kruse

Approved for public release; distribution is unlimited

THIS PAGE INTENTIONALLY LEFT BLANK

REPORT DOCUMENTATION PAGE			<i>Form Approved OMB No. 0704-0188</i>	
Public reporting burden for this collection of information is estimated to average 1 hour per response, including the time for reviewing instruction, searching existing data sources, gathering and maintaining the data needed, and completing and reviewing the collection of information. Send comments regarding this burden estimate or any other aspect of this collection of information, including suggestions for reducing this burden, to Washington headquarters Services, Directorate for Information Operations and Reports, 1215 Jefferson Davis Highway, Suite 1204, Arlington, VA 22202-4302, and to the Office of Management and Budget, Paperwork Reduction Project (0704-0188) Washington DC 20503.				
1. AGENCY USE ONLY (Leave blank)		2. REPORT DATE September 2013	3. REPORT TYPE AND DATES COVERED Master's Thesis	
4. TITLE AND SUBTITLE MODTRAN RADIANCE MODELING OF MULTI-ANGLE WORLDVIEW-2 IMAGERY			5. FUNDING NUMBERS	
6. AUTHOR(S) Samuel I. Marshall				
7. PERFORMING ORGANIZATION NAME(S) AND ADDRESS(ES) Naval Postgraduate School Monterey, CA 93943-5000			8. PERFORMING ORGANIZATION REPORT NUMBER	
9. SPONSORING /MONITORING AGENCY NAME(S) AND ADDRESS(ES) N/A			10. SPONSORING/MONITORING AGENCY REPORT NUMBER	
11. SUPPLEMENTARY NOTES The views expressed in this thesis are those of the author and do not reflect the official policy or position of the Department of Defense or the U.S. Government. IRB Protocol number ____ N/A ____.				
12a. DISTRIBUTION / AVAILABILITY STATEMENT Approved for public release; distribution is unlimited			12b. DISTRIBUTION CODE A	
13. ABSTRACT (maximum 200 words) <p>The WorldView-2 satellite, launched in 2010 by DigitalGlobe, provides researchers with the ability to collect high resolution, multi-angle, 8-band multispectral imagery. This offers a unique opportunity to investigate the reflectance properties—including the bidirectional reflectance distribution function—of surfaces detected from a space-based remote sensing platform. Eight images were collected over Rio de Janeiro on January 19, 2010, at approximately 1000 local time. Solar geometry during the collect remained constant while sensor geometry ranged from approximately 10 degrees off-nadir to 60 degrees off-nadir, fore and aft. To enhance understanding and provide comparison data with the multi-angle imagery data, radiance models were generated using the Moderate Resolution Atmospheric Transfer code. General models, using surface albedos ranging from 1% to 100%, and comparison models, using properties as close as possible to that found in the imagery, were built. Using data derived from all sources, variations were readily apparent that could be attributed to the multi-angle geometry of the collect, the wavelength of the light sensed and reflectance</p>				
14. SUBJECT TERMS Remote Sensing, WorldView-2, Multispectral, MODTRAN, MODO, ENVI, BRDF, Bidirectional Reflectance Distribution Function, Multi-angle, Reflectance, Radiance, Rio de Janeiro.			15. NUMBER OF PAGES 105	
			16. PRICE CODE	
17. SECURITY CLASSIFICATION OF REPORT Unclassified	18. SECURITY CLASSIFICATION OF THIS PAGE Unclassified	19. SECURITY CLASSIFICATION OF ABSTRACT Unclassified	20. LIMITATION OF ABSTRACT UU	

NSN 7540-01-280-5500

Standard Form 298 (Rev. 2-89)
Prescribed by ANSI Std. Z39-18

THIS PAGE INTENTIONALLY LEFT BLANK

Approved for public release; distribution is unlimited

**MODTRAN RADIANCE MODELING OF MULTI-ANGLE WORLDVIEW-2
IMAGERY**

Samuel I. Marshall
Commander, United States Navy
B.S., Ursinus College, 1993

Submitted in partial fulfillment of the
requirements for the degree of

MASTER OF SCIENCE IN SPACE SYSTEMS OPERATIONS

from the

**NAVAL POSTGRADUATE SCHOOL
September 2013**

Author: Samuel I. Marshall

Approved by: Richard C. Olsen
Thesis Advisor

Fred A. Kruse
Thesis Co-Advisor

Rudolf Panholzer
Chair, Space Systems Academic Group

THIS PAGE INTENTIONALLY LEFT BLANK

ABSTRACT

The WorldView-2 satellite, launched in 2010 by DigitalGlobe, provides researchers with the ability to collect high resolution, multi-angle, 8-band multispectral imagery. This offers a unique opportunity to investigate the reflectance properties—including the bidirectional reflectance distribution function—of surfaces detected from a space-based remote sensing platform. Eight images were collected over Rio de Janeiro on January 19, 2010, at approximately 1000 local time. Solar geometry during the collect remained constant while sensor geometry ranged from approximately 10 degrees off-nadir to 60 degrees off-nadir, fore and aft. To enhance understanding and provide comparison data with the multi-angle imagery data, radiance models were generated using the Moderate Resolution Atmospheric Transfer code. General models, using surface albedos ranging from 1% to 100%, and comparison models, using properties as close as possible to that found in the imagery, were built. Using data derived from all sources, variations were readily apparent that could be attributed to the multi-angle geometry of the collect, the wavelength of the light sensed and reflectance

THIS PAGE INTENTIONALLY LEFT BLANK

TABLE OF CONTENTS

I.	INTRODUCTION	1
A.	PURPOSE OF RESEARCH	1
B.	SPECIFIC OBJECTIVE.....	1
II.	BACKGROUND	3
A.	CHARACTERIZATION OF LIGHT	3
1.	The Interaction of Light and Matter	3
2.	Quantification of Light	5
a.	<i>The Electromagnetic Spectrum, Wavelength and Frequency.....</i>	<i>5</i>
b.	<i>Blackbodies, Energy and Solar Irradiance.....</i>	<i>7</i>
c.	<i>Radiometric Terms.....</i>	<i>9</i>
d.	<i>Understanding Reflectance.....</i>	<i>11</i>
B.	ATMOSPHERIC EFFECTS ON LIGHT	16
1.	Atmospheric Composition.....	17
2.	Atmospheric Absorption	18
3.	Atmospheric Scattering.....	19
4.	Target and Path Radiance.....	22
C.	PREVIOUS RESEARCH.....	25
1.	Naval Postgraduate School.....	25
a.	<i>McConnon Thesis (McConnon, 2010).....</i>	<i>25</i>
b.	<i>High Spatial Resolution Bidirectional Reflectance Retrieval Using Satellite Data (Olsen, Kim, and McConnon, 2011).....</i>	<i>25</i>
c.	<i>Lee Thesis (Lee, 2012)</i>	<i>26</i>
2.	Other Research.....	26
a.	<i>MISR.....</i>	<i>26</i>
b.	<i>CHRIS</i>	<i>28</i>
III.	DATA AND METHODS	29
A.	DATA	29
1.	Source and Data	29
a.	<i>Worldview-2 Satellite</i>	<i>29</i>
b.	<i>Rio de Janeiro Imagery.....</i>	<i>30</i>
2.	Tools	32
a.	<i>ENVI.....</i>	<i>32</i>
b.	<i>MODTRAN and MODO</i>	<i>32</i>
B.	IMAGE PREPARATION	34
1.	Image Organization and Multi-Angle Assessment	34
2.	Spatial Sub-setting	35
3.	Top-of-Atmosphere Radiance Correction	38
4.	Image Registration.....	38
5.	Regions of Interest and Statistical Outputs.....	39
C.	ATMOSPHERIC MODELING.....	41

1.	Model Parameters	41
a.	<i>Atmospheric Values</i>	41
a.	<i>Surface Reflectance Inputs</i>	43
b.	<i>Frequency Range and Resolution</i>	44
c.	<i>WorldView-2 Sensor Characteristics</i>	44
2.	MODTRAN Input Template Creation.....	45
a.	<i>Input Template Organization and Batch Processing</i>	45
b.	<i>Albedo Calculations</i>	45
c.	<i>Surface Reflectance Calculations</i>	46
3.	Model Outputs and Processing	46
a.	<i>Outputs and Processing</i>	46
IV.	RESULTS AND ANALYSIS	47
A.	MODTRAN ALBEDO MODELS	47
1.	WV-2 Spectral Band and Image Geometry Plots	47
2.	Path Scattered and Ground Reflected Radiance Plots	50
B.	COMPARISON OF WV-2 IMAGERY TO MODTRAN MODELS, BY BAND.....	55
1.	Asphalt	55
a.	<i>Analysis–Radiance vs. Band</i>	56
b.	<i>Analysis–Radiance vs. Image Geometry</i>	57
2.	Sand.....	58
a.	<i>Analysis–Radiance vs. Band</i>	59
b.	<i>Analysis–Radiance vs. Image Geometry</i>	60
3.	GRASS	61
a.	<i>Analysis–Radiance vs. Band</i>	62
b.	<i>Analysis–Radiance vs. Image Geometry</i>	63
V.	CONCLUSIONS	65
A.	SUMMARY OF ANALYSIS AND RESULTS	65
B.	CONCLUSIONS	65
C.	FUTURE WORK POSSIBILITIES.....	67
1.	MODTRAN Modeling using BRDF Algorithms.....	67
2.	MODTRAN Modeling of Hyperspectral Data	67
3.	Further Investigation of MODTRAN-modeled Radiance Elements.....	67
4.	Investigate WorldView-2 BRDF Phenomena using NEFDS Applications	67
	APPENDIX.....	69
A.	ENVI STATISTICS FILE.....	69
B.	MODTRAN RADIANCE PLOTS: RADIANCE VS. BAND AND RADIANCE VS. IMAGE GEOMETRY FOR VARYING ALBEDO.....	70
C.	MODTRAN RADIANCE PLOTS, 380–1100 NM	75
D.	IMAGERY HISTOGRAMS BY BAND	78
	LIST OF REFERENCES	83
	INITIAL DISTRIBUTION LIST	87

LIST OF FIGURES

Figure 1.	The Four Interactions of Light and Matter (From Olsen, 2007).....	4
Figure 2.	Electro-Optical Remote Sensing (From CRISP, n.d.)	5
Figure 3.	The Electromagnetic Spectrum (From Halliday, Resnick, & Walker, 2011)....	7
Figure 4.	Solar Spectral Irradiance (From Brooks, 2008)	9
Figure 5.	Irradiance and exitance (After Jaques and Prah, 1998)	10
Figure 6.	Radiance (From Schott, 1997)	11
Figure 7.	Soil reflectance example with varying source and observer geometry (left: sun behind observer; right: sun ahead of observer) (From Lucht and Schaaf, 2006)	13
Figure 8.	Beam Geometry Above a Surface.....	13
Figure 9.	Nine geometry combination for incident and reflected light (From Schaepman-Strub et al., 2006, p. 30)	14
Figure 10.	Goniometer (From Coburn, 2006)	16
Figure 11.	Atmospheric Density, Pressure, Temperature up to 100 km (From The Free Dictionary by Farlex [as cited in Budyko and Kondratyev, 1979]).....	18
Figure 12.	MODTRAN Transmittance Curve.....	19
Figure 13.	Intensity of Rayleigh scattering varies inversely with the fourth power of the wavelength (λ^{-4}) (From Jensen, 2007)	21
Figure 14.	Rayleigh and Mie Scattering (From Nave, 2000)	22
Figure 15.	Various Paths of Radiance Received by a Remote Sensing System (From Jensen, 2007).....	23
Figure 16.	Histogram of brightness values for spectral channel 1 (400-450 nm) over Camp Pendleton, CA (From Olsen et al., 2011)	26
Figure 17.	Multi-angle Imaging Spectro-radiometer (From NASA JPL, 2013)	27
Figure 18.	“Agile PROBA-1 rolls in its orbit to take images” (From ESA, 2011).....	28
Figure 19.	WorldView-2 Satellite (From DigitalGlobe)	29
Figure 20.	Rio de Janeiro Imagery: Satellite and Solar Geometry.....	31
Figure 21.	MODTRAN Atmospheric Profiles for H ₂ O Composition by Altitude (From Berk et al., 2011).....	33
Figure 22.	Screenshot of MODO Graphical User Interface	34
Figure 23.	Separation Angles of the Eight Rio de Janeiro WV-2 Images.....	35
Figure 24.	True color image chip from P008 (WV-2 bands 5, 3, 2 (RGB), approximate image center 22°54'30" S, 43°10'00" W, approximate image dimensions 17 km x 17 km).....	36
Figure 25.	Image chip P008 Side-by-side with Google Terrain Map (left side WV-2 bands 5, 3, 2 (RGB), approximate image center 22°54'46" S, 43°10'35" W, approximate image dimensions 4 km x 5 km; right side from Google Maps, 2013)	37
Figure 26.	ROI's Used in the Imagery Analysis, Displayed on Image P008 (WV-2 bands 5, 3, 2 (RGB), approximate image dimensions 1 km x 0.5 km).....	40
Figure 27.	MODTRAN Sensor Geometry	42
Figure 28.	MODTRAN Solar Geometry (From Berk et al., 2011)	43

Figure 29.	MODTRAN Radiance Plots, Albedo: 1%, 25%, 50%.....	48
Figure 30.	MODTRAN Path Scattered & Ground Reflected Radiance, 1% Albedo, P2 & P8 geometry	50
Figure 31.	MODTRAN Path Scattered & Ground Reflected Radiance, 25% Albedo, P2 & P8 geometry	51
Figure 32.	MODTRAN Path Scattered & Ground Reflected Radiance, 50% Albedo, P2 & P8 geometry	51
Figure 33.	MODTRAN Path Scattered & Ground Reflected Radiance, 75% Albedo, P2 & P8 geometry	52
Figure 34.	MODTRAN Path Scattered & Ground Reflected Radiance, 100% Albedo, P2 & P8 geometry	52
Figure 35.	Zoomed-in Path Scattered & Ground Reflected Radiance, 25% Albedo, P2 & P8 geometry	54
Figure 36.	ASPHALT_DARK Spectral Reflectance Plot (After DLR using data included with MODO)	56
Figure 37.	ASPHALT – Radiance vs. Band.....	57
Figure 38.	ASPHALT–Radiance vs. Image Geometry	58
Figure 39.	LIGHT YELLOWISH BROWN LOAMY SAND Spectral Reflectance Plot (After Baldridge et al., 2009, using data downloaded from http://speclib.jpl.nasa.gov/)	59
Figure 40.	SAND – Radiance vs. Band.....	60
Figure 41.	SAND – Radiance vs. Image Geometry	61
Figure 42.	GRASS Spectral Reflectance Plot (After Baldridge et al., 2009, using data included with ENVI).....	62
Figure 43.	GRASS – Radiance vs. Band.....	63
Figure 44.	GRASS – Radiance vs. Image Geometry	64

LIST OF TABLES

Table 1.	Types of Atmospheric Scattering (data after Jensen, 2007; images from Nave, 2000).....	20
Table 2.	WorldView-2 Sensor Characteristics (After DigitalGlobe, Inc., 2013).....	30
Table 3.	Rio de Janeiro Imagery: Date, Time, and Geometry	31
Table 4.	MODTRAN Solar and Sensor Geometry Inputs	43

THIS PAGE INTENTIONALLY LEFT BLANK

LIST OF ACRONYMS AND ABBREVIATIONS

AOD	Aerosol Optical Depth
BRDF	Bidirectional Reflectance Distribution Function
CHRIS	Compact High Resolution Imaging Spectrometer
DISORT	Discrete Ordinates Radiative Transfer Program
DN	Digital Number
EM	Electromagnetic
ENVI	Environment for Visualizing Images Software Application (Exelis Visual Information Solutions, Inc.)
EO	Electro-optical
IMD	Image Metadata File
IR	Infrared
JPL	NASA Jet Propulsion Laboratory
LAI	Leaf Area Index
MISR	Multi-angle Imaging Spectro-radiometer
MODO	MODTRAN Graphical User Interface Software Program (Research Applications Schlaepfer)
MODTRAN	Moderate Resolution Atmospheric Transfer code
NASA	National Aeronautics and Space Administration
NEFDS	Nonconventional Exploitation Factors Data System
NGA	National Geospatial-Intelligence Agency
NIR	Near infrared
NITF	National Imagery Transmission Format
ROI	Region of Interest
TOA	Top of Atmosphere
UV	Ultraviolet
VNIR	Visible to Near Infrared
VIS	Visible
WV-2	WorldView-2

THIS PAGE INTENTIONALLY LEFT BLANK

ACKNOWLEDGMENTS

Special thanks are given to Professor Richard Olsen and Professor Fred Kruse of the Naval Postgraduate School for their assistance in completing this thesis. Special thanks are also offered to Mr. Andy Dinville and Mr. Victor Leonard of DigitalGlobe for providing the WorldView-2 imagery of Rio de Janeiro.

THIS PAGE INTENTIONALLY LEFT BLANK

I. INTRODUCTION

A. PURPOSE OF RESEARCH

Remotely sensed imagery of the Earth, in the visible (VIS) to near infrared (NIR) wavelengths, collects incident light from the sun reflected off the Earth. From source to sensor, the journey of the sun's light takes multiple paths and experiences numerous property-changing interactions that can profoundly affect what will ultimately be detected at the satellite.

When studying reflected light, both the source and direction of the incident light as well as the physical arrangement of the sensor with regard to the incident light are important. Furthermore, the properties of the surface upon which light is incident strongly affect the nature of the light reflected. The bidirectional reflectance distribution function (BRDF) is a means of quantifying how light will reflect from a particular surface over all the possible combinations of incident and reflected directions. Within the last decade, advances in the sensitivity and resolution of commercial remote sensing satellites have provided scientists with the enhanced ability to investigate BRDF effects from remote-sensing satellite platforms.

The purpose of this thesis was to analyze multispectral satellite imagery, looking for effects that may be directly attributable to BRDF properties. Eight images of Rio de Janeiro, Brazil, collected by the WorldView-2 satellite, were the primary source material for this analysis. Atmospheric models, generated using the Moderate Resolution Atmospheric Transmission program (MODTRAN), were also created using geometry and physical conditions similar to those found in the collected imagery. Both the imagery and atmospheric models were then compared, allowing assessment of the ability to distinguish reflectance properties of remotely sensed surfaces of interest.

B. SPECIFIC OBJECTIVE

The principle objective of this thesis was two-fold: using common remote sensing software tools, (1) analyze multi-angle, multispectral imagery, looking for variations in reflectance properties associated with BRDF, and (2) develop software-

based atmospheric models, using parameters similar to those found in the imagery, for comparison to the imagery and validation. It was expected that results would provide broad insight into the capabilities available to investigate BRDF properties found within multi-angle, multispectral imagery—capabilities that may find utility in commercial, civil, and military applications.

II. BACKGROUND

A. CHARACTERIZATION OF LIGHT

In the simplest of terms, remote sensing in the visible and near infrared portions of the electromagnetic (EM) spectrum is the study of reflected light. In human vision, visible light is sensed by our eyes and processed by our minds, activities that allow us to develop conclusions about and understand the physical world surrounding us. Electro-optical sensors placed in Earth orbit also gather light using mechanisms very similar to our eyes, but with much greater sensitivity and in much broader spectral regimes. This remotely gathered light is then processed, recorded and, ultimately, presented as imagery that allow us to, again, make conclusions about the world around us. Understanding light, therefore, is fundamental to any study of remote sensing.

1. The Interaction of Light and Matter

The very notion of “sensing” requires a physical interaction, and the sensing of light is no different. When considering only the visible EM spectrum (the only spectrum that our eyes are capable of detecting), the light that we sense originates directly from (1) a source (natural or artificial) and (2) from one, or a combination, of the four fundamental interactions of light with matter: transmission, reflection, scattering and absorption (Olsen, 2007). In Figure 1, if one assumes an observer in the plane of incident light (above each gray surface), what is actually seen is the light that is directly reflected (specular reflection) or scattered (diffuse reflection). Transmitted light and absorbed light have no path to the eye (unless, of course, the emission resulting from absorption occurs in the visible spectrum).

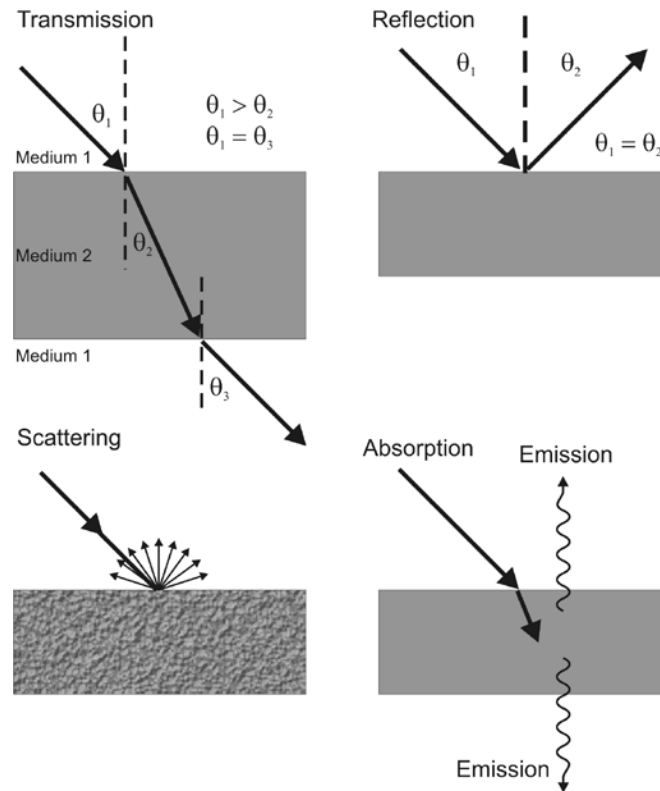


Figure 1. The Four Interactions of Light and Matter (From Olsen, 2007)

Extending this concept of the four interactions further, from the law of conservation of energy it follows that the energy of the incident light must equal the sum of the reflected, transmitted, scattered and absorbed light. Considering only the visible spectrum and a surface that is, itself, not a light source, an object will have color simply due to the fact that that object's surface is reflecting light of that specific wavelength. Because different surfaces have different colors which are, in general, different in color from the incident light, each surface must have unique properties with regard to the four interactions described previously. The study of this unique behavior of light interaction is the essence of remote sensing. Figure 2 illustrates this behavior from an electro-optical (EO) remote sensing platform.

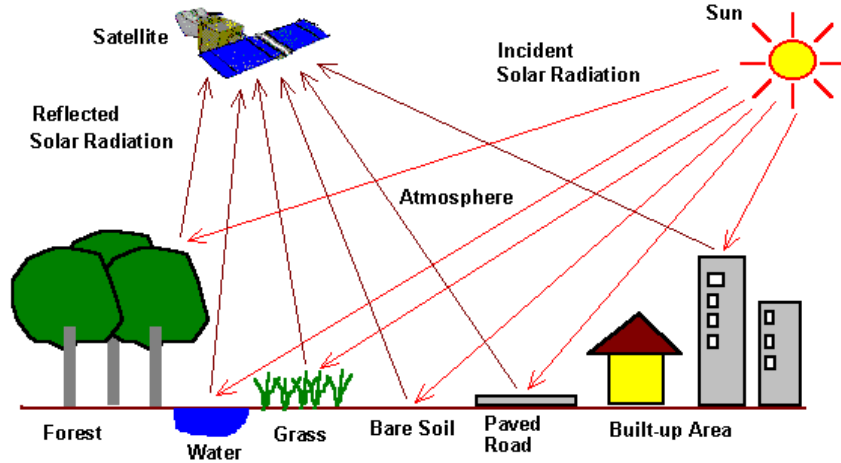


Figure 2. Electro-Optical Remote Sensing (From CRISP, n.d.)

2. Quantification of Light

To better characterize the nature of light in addition to color, it is important to understand the fundamental physics and nomenclature describing light and its propagation.

a. *The Electromagnetic Spectrum, Wavelength and Frequency*

Formulation of classical electrodynamics by James Clerk Maxwell revealed light to be a manifestation of interactions between electric and magnetic fields (Griffiths, 1999). This, in turn, led directly to our understanding that light behaves as a wave.

Maxwell completely described the behavior of electric, E , and magnetic, B , fields with the following equations:

$$\nabla \cdot \mathbf{E} = 0 \quad (2.1)$$

$$\nabla \cdot \mathbf{B} = 0 \quad (2.2)$$

$$\nabla \times \mathbf{E} = -\frac{\delta \mathbf{B}}{\delta t} \quad (2.3)$$

$$\nabla \times \mathbf{B} = \mu_0 \epsilon_0 \frac{\delta \mathbf{E}}{\delta t} \quad (2.4)$$

$$\mu_0 = 4\pi \cdot 10^{-7} \text{ N/A}^2 \quad (2.5)$$

is the permeability of free space and

$$\varepsilon_0 = 8.85 \cdot 10^{-12} \text{ C}^2/\text{Nm}^2 \quad (2.6)$$

is the permittivity of free space (Griffiths, 1999).

Solving using (2.3) and (2.4) results in

$$\nabla^2 \mathbf{E} = \mu_0 \varepsilon_0 \frac{\partial^2 \mathbf{E}}{\partial t^2} \quad (2.7)$$

and

$$\nabla^2 \mathbf{B} = \mu_0 \varepsilon_0 \frac{\partial^2 \mathbf{B}}{\partial t^2} \quad (2.8)$$

which are both easily recognized as second-order partial differential equations of the form commonly known as the wave equation

$$\nabla^2 f = \frac{1}{c^2} \frac{\partial^2 f}{\partial t^2}. \quad (2.9)$$

Comparing (2.7), (2.8) and (2.9) results in the speed of light

$$c = \frac{1}{\mu_0 \varepsilon_0} = 2.9979 \cdot 10^8 \text{ m/s}. \quad (2.10)$$

From fundamental physics, the speed of wave propagation (v) is directly proportional to its frequency (f) and wavelength (λ) by

$$v = f \lambda. \quad (2.11)$$

Because the speed of light is constant (2.10), the spectrum of electromagnetic radiation (i.e., light) can be clearly defined (2.11) in terms of frequency and wavelength (Figure 3).

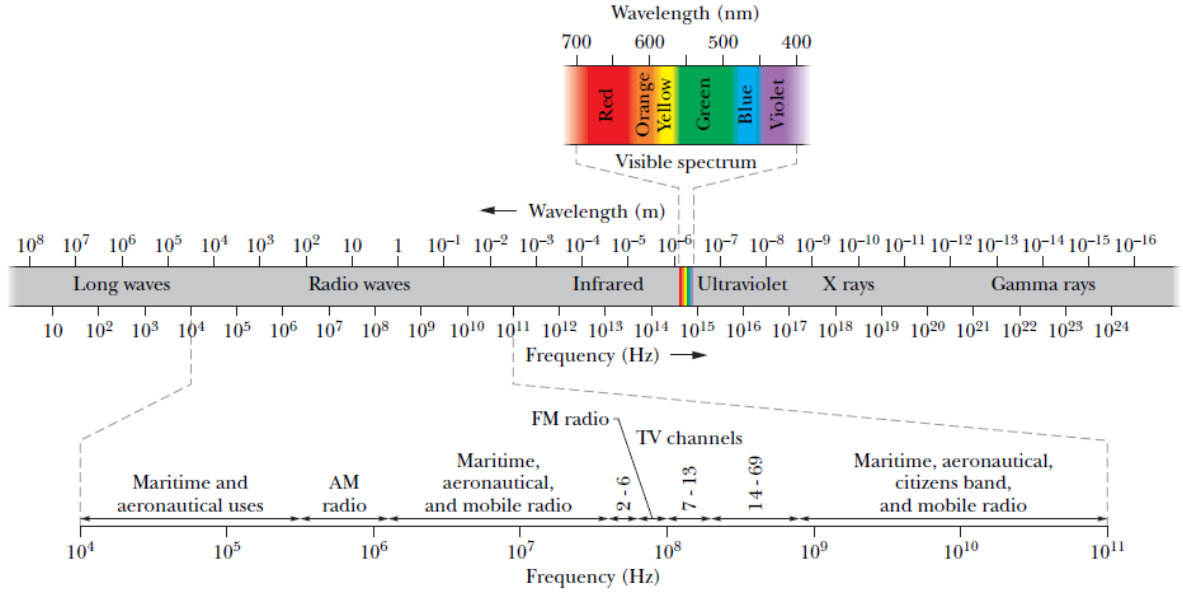


Figure 3. The Electromagnetic Spectrum (From Halliday, Resnick, & Walker, 2011)

b. Blackbodies, Energy and Solar Irradiance

According to Kirchhoff's Theorem,

$$\frac{E_f}{A_f} = J(f, T), \quad (2.12)$$

the ratio of emitted EM energy, E_f , to absorbed EM energy, A_f , of an object is dependent on both the frequency, f , and temperature, T , of the object (Serway, Moses, & Moyer, 1989). An ideal object that absorbs all incident EM energy ($A_f = 1$) is known as a "blackbody" since, as no light is reflected in the visible spectrum, it would appear black to the human eye (Serway et al., 1989). From (2.12), a blackbody must also be an ideal radiator (Serway et al., 1989). The study of blackbody radiation led to our understanding of the quantum nature of light and the developments that follow.

In the early part of the last century, Max Planck discovered that the energy of light, E , emitted from a blackbody would only do so in discrete intervals (Serway et al., 1989)

$$E = nhf \quad (n=1, 2, \dots) \quad (2.13)$$

in which f is the frequency of the emitted light and Planck's constant is given by

$$h = 6.626 \cdot 10^{-34} \text{ J} \cdot \text{s} . \quad (2.14)$$

Through the work of Einstein, Compton, Bohr and numerous other great physicists, we now know that these discrete intervals are due to both the wave-particle duality of light and the quantum nature of matter at the atomic and sub-atomic scale (Serway et al., 1989). As electrons move between energy states or nuclear reactions occur in highly energetic environments (such as our sun), the release of EM energy can be predicted and quantified based on the composition of the interacting particles. Furthermore, observations of scattering phenomena following light interactions confirm that light must possess particle-like properties. In simple terms, we call this photon behavior with a momentum, p , given by (Serway et al., 1989)

$$p = \frac{E}{c} = \frac{hf}{c} = \frac{h}{\lambda} . \quad (2.15)$$

Returning to the quantum perspective, an investigation into the light emitted from a blackbody will provide an indication of both the composition and energy of the blackbody. The energy is of most concern for remote sensing and can be directly related to the temperature through Planck's radiation law (Thornton and Rex, 2013)

$$E(\lambda, T) = \frac{2\pi hc^2}{\lambda^5} \left(\frac{1}{e^{\frac{hc}{\lambda kT}} - 1} \right) . \quad (2.16)$$

With (2.16) and the fact that the surface of the sun is approximately 5800K, a blackbody curve can be plotted (Figure 4). It is interesting to note that the actual spectrum of solar energy reaching the Earth is not a smooth curve; this is due to the quantum influences on electromagnetic emission due to the sun's actual composition.

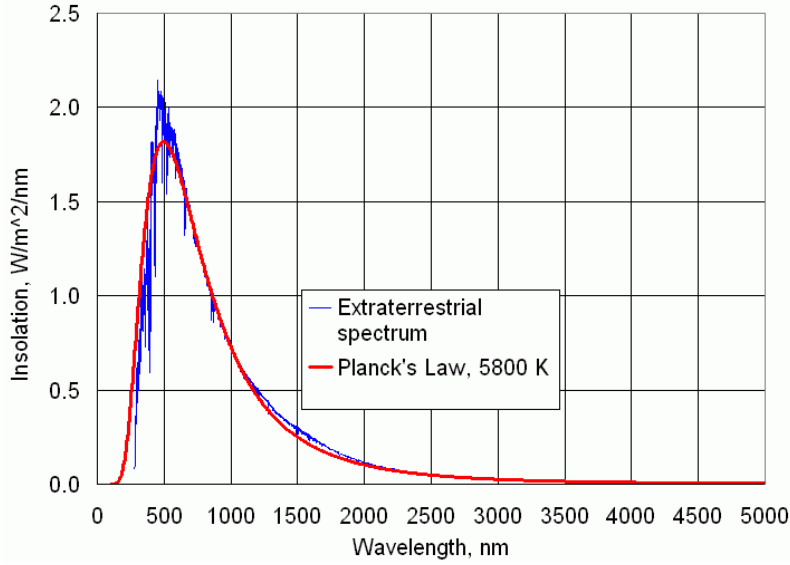


Figure 4. Solar Spectral Irradiance (From Brooks, 2008)

Utilizing the above equations, the amount of solar electromagnetic energy reaching the upper atmosphere of the Earth can be calculated as approximately 1376 W/m^2 (the area under the red curve in Figure 4) and peaks in the visible spectrum.

c. Radiometric Terms

Understanding the basic physics of light, and that its primary source in our solar system is the sun, some basic terms now require definition. In the field of remote sensing, the following terms are ubiquitous.

(1) Radiant Flux (Φ). The energy contained in a beam of light (Q) can most easily be understood and given utility in terms of the rate of energy propagation, known as radiant flux (Schott, 1997)

$$\Phi = \frac{dQ}{dt} \text{ W.} \quad (2.17)$$

(2) Irradiance and Spectral Irradiance (E). The amount of radiant flux falling onto a surface (Figure 5) is given by (Schott, 1997)

$$E = \frac{d\Phi}{dA} \text{ W/m}^2. \quad (2.18)$$

Spectral irradiance is irradiance per unit wavelength and is given by

$$E(\lambda) = \frac{d\Phi}{dA d\lambda} \text{ W/m}^2 \cdot \text{m} . \quad (2.19)$$

Exitance, M , is another commonly used term similar in form to irradiance; the difference is simply that the flux is away from the surface (Schott, 1997).

(3) Radiance (L). Both of the irradiance terms (2.18 and 2.19) provide spatial information for a beam of light only with regard to the amount of radiant flux onto (or, regarding exitance, away from) a surface (Figure 5), they do not provide an unambiguous indication of the direction that the light is moving.

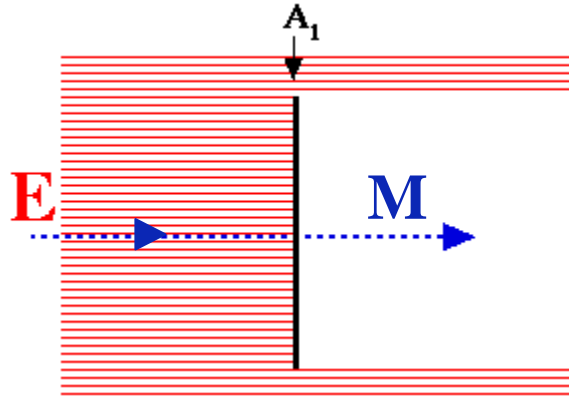


Figure 5. Irradiance and exitance (After Jaques and Prah, 1998)

To solve this dilemma, radiant intensity, defined as radiant flux per element of solid angle, is given by (Schott, 1997)

$$I = \frac{d\Phi}{d\Omega} \text{ W/sr} \quad (2.20)$$

in which the element of solid angle is defined as $d\Omega = \frac{dA}{r^2}$ steradians (Schott, 1997).

Dividing radiant intensity by an element of surface area, as done for radiant flux, results in the radiance, which provides both spatial and directional information for the radiant flux (Schott, 1997):

$$L = \frac{dI}{dA} = \frac{dE}{d\Omega} = \frac{d^2\Phi}{dAd\Omega} \text{ W/m}^2 \cdot \text{sr}. \quad (2.21)$$

For surfaces not perpendicular to the radiant flux, (2.21) can be corrected to the surface normal by introduction of a cosine term in the denominator. With radiance, the surface area is the circular area which is projected in the plane under study (open end of cone in Figure 6). Contrasted with irradiance and exitance, radiance can define both inward and outward fluxes; the direction component only need reference a consistent plane of reference (the square surface in Figure 6) (Schott, 1997).

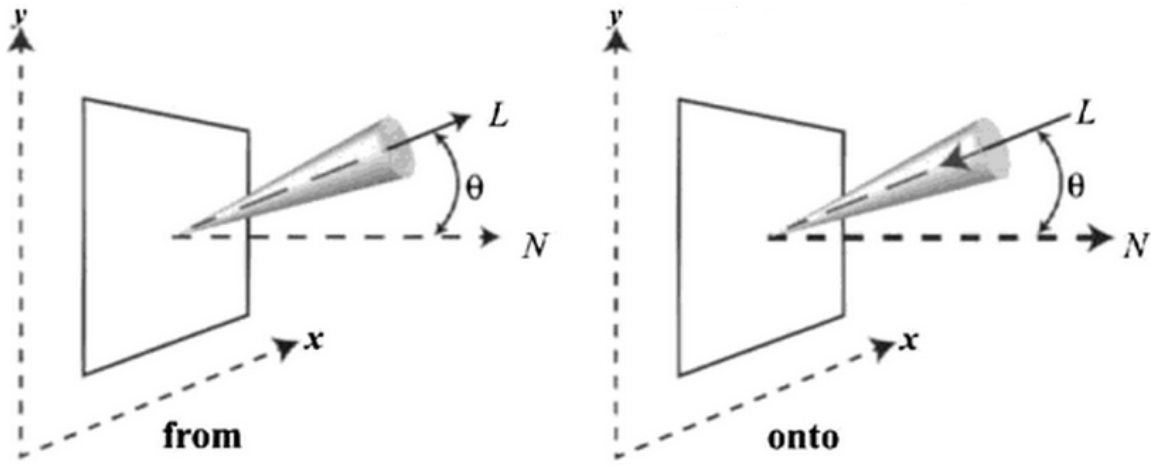


Figure 6. Radiance (From Schott, 1997)

Similar to spectral irradiance, spectral radiance is simply radiance per unit wavelength

$$L(\lambda) = \frac{dL}{d\lambda} \text{ W/m}^2 \cdot \text{sr} \cdot \text{m}. \quad (2.22)$$

d. Understanding Reflectance

To this point, the effects of the reflective surface, itself, on both the inbound and outbound light, have not been quantified in radiometric terms. As discussed previously, if a surface, illuminated by white light (e.g., the sun), appears to have color, then that surface must have some intrinsic property effecting the relationship between

incident and reflected light. The comparison of reflected light to incident light is the starting point for further discussion.

(1) Reflectance Definition. For a real element of surface area, reflectance is simply the ratio of reflected flux to incident flux (Nicodemus, Richmond, Hsia, Ginsberg, & Limperis, 1977). Using terms defined in part (c), reflectance is, therefore, simply a ratio of the exitance (M) to the irradiance (L) upon an element of surface area, dA , and is given by (Schott, 1997)

$$\rho = \frac{M}{E} \text{ (Unit less).} \quad (2.23)$$

Values for reflectance can only possess values between 0 (no reflection) to 1 (complete reflection). It is important to note that the two terms comprising the ratio in (2.23) contain no directional info for either the source or reflected light. As shown in Figure 7, it is apparent that values of reflectance are different for different viewing geometries; consequently, in order to adequately quantify reflectance, beam geometry must be explained and understood.



Figure 7. Soil reflectance example with varying source and observer geometry (left: sun behind observer; right: sun ahead of observer) (From Lucht and Schaaf, 2006)

(2) Beam geometry. Assuming a flat surface area element with both source and sensor located above, the maximum volume of consideration for both the incoming and outgoing light is that of a hemisphere (i.e., in terms of solid angle, the maximum extent is 2π steradians (Figure 8)) ((Schaepman-Strub, Schaepman, Painter, Dangel, & Martonchik, 2006).

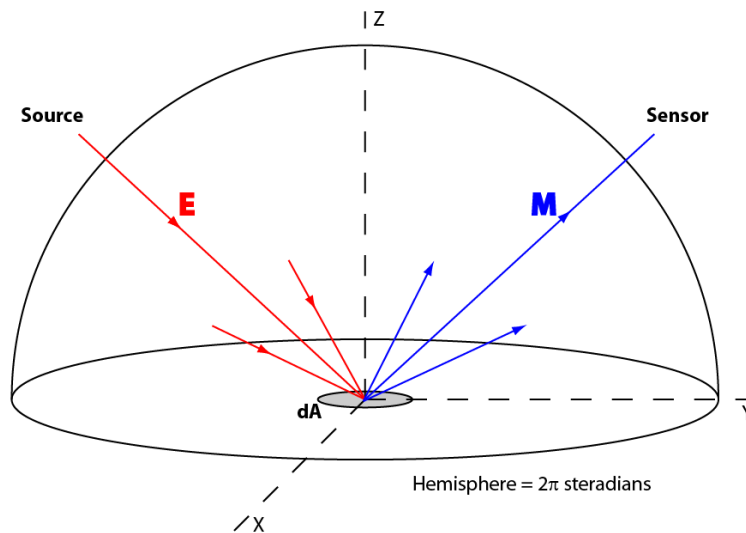


Figure 8. Beam Geometry Above a Surface

Additionally, both the incoming and outgoing light may be diffuse, specular or a combination of the two. According to the seminal work *Geometrical Considerations and Nomenclature for Reflectance* (Nicodemus et al., 1977), three

different means of characterizing directional reflectance were developed: hemispherical (purely diffuse), directional (purely specular) and conical (a hybrid of the two). From these three characterizations, it follows that there are nine different geometry combinations that can be used to adequately describe the directional relationships between incident and reflected light (Figure 9).

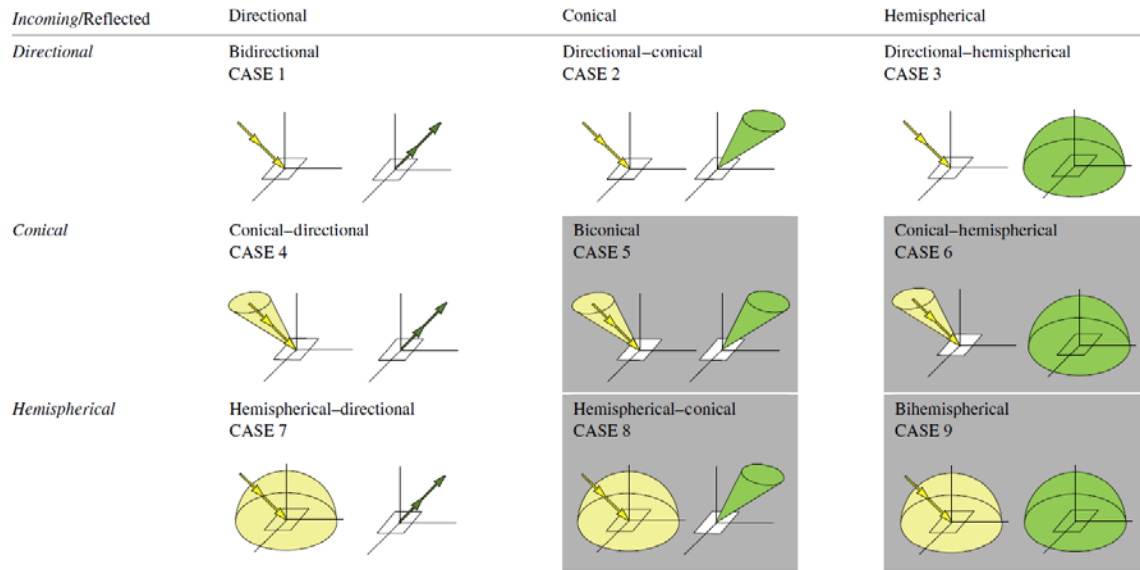


Figure 9. Nine geometry combination for incident and reflected light
(From Schaepman-Strub et al., 2006, p. 30)

In a natural environment at large scale (such as satellite remote sensing), the bihemispherical-conical case (case 8) is most fitting since it considers incident light from all directions reflected into a sensor viewing cone of limited extent. The question still remains, however, of how to characterize the reflectance properties of a surface for all source and viewing geometries.

(3) Bidirectional Reflectance Distribution Function (BRDF). Looking closely at each of the cases in Figure 9, it can be reasonably concluded that the incident and reflected elements of any of the conical and hemispherical cases may be simplified to that of the directional case integrated over finite solid angles, up to and including 2π steradians. Furthermore, integration of the directional case over finite solid angles implies that the values used must be of infinitesimal scope and also include terms

for the directions of both incident and reflected beams. This mathematical result is known as the bidirectional reflectance distribution function and, similar to the definition of reflectance, is the ratio of an infinitesimal element of reflected radiance to an infinitesimal element of irradiance (Schaepman-Strub et al., 2006):

$$BRDF = f(\theta_i, \phi_i; \theta_r, \phi_r) = \frac{dL_r(\theta_i, \phi_i; \theta_r, \phi_r)}{dE_i(\theta_i, \phi_i)} \text{ sr}^{-1}. \quad (2.24)$$

At this point, the ability to fully characterize the surface reflectance for all combinations of source and viewing geometries can be *mathematically* described using the BRDF. However, because the BRDF is formally defined “as a ratio of infinitesimals...that can never be measured directly” (Nicodemus et al., 1977), then, for practical applications, its usage in language and experimentation requires further elaboration, particularly when discussing applications in remote sensing.

(4) Measurements of Reflectance. For actual determination of reflectance it is important to note which of the radiometric terms discussed so far are actually capable of measurement. Radiance is the most common value measured from a remote sensing platform and this measurement allows calculation of parameters such as reflectance. The BRDF, on the other hand, is not something that can be directly measured. It can, however, be approximated quite accurately by gathering comprehensive reflectance data across all combinations of source and viewing geometries using devices such as a goniometer (Figure 10).



Figure 10. Goniometer (From Coburn, 2006)

Within the last decade, satellite electro-optical sensors have advanced to such a degree that the resultant imagery has pixel resolutions less than one meter. Combined with this enhanced resolution, the ability of a satellite to gather multiple images of the same location in a single pass raises the opportunity to study multi-angle reflectance properties from space. While it is not possible to “measure the BRDF” from space, it should now be possible to extract satellite radiometric data that allows calculation of a surface’s BRDF. These effects appear as variations in a surface’s radiance or reflectance as long as the data are gathered over a short time frame (i.e., single satellite pass). This ensures that the light source and atmospheric conditions between images are approximately the same. Of these latter two conditions, the light source (the sun) has already been discussed and should have little variation between images. The atmospheric effects on light, however, require further investigation.

B. ATMOSPHERIC EFFECTS ON LIGHT

For the visible to near IR spectrum, the top of atmosphere (TOA) irradiance from the sun is the primary source of light that leads to detection at a satellite sensor. Satellite electro-optical sensors, however, do not discriminate the source of illumination. The light

detected at the sensor may be direct from the sun, reflected from the surface of the Earth, or the product of any of a number of these and other interactions with matter on the path to the sensor. The effects that this path through atmosphere has on light must, therefore, be explained. These include: (1) the actual mechanisms of atmospheric influence on light propagation and (2) characterization of these mechanisms such that they can be analyzed in terms of radiance detected at the satellite sensor.

1. Atmospheric Composition

The Earth's atmosphere is composed of numerous particles, ranging in size from single atoms and molecules in gaseous form up to larger particulate matter such as aerosols (e.g., dust and soot) and water (e.g., droplets or ice). Below approximately 100 km (homosphere), the distribution of molecules by mean molecular weight is relatively uniform with a steadily decreasing density and pressure (Salby, 1996; Budyko and Kondratev, 2010). Above 100km (heterosphere), the atmosphere has thinned to such an extent that molecular weights begin to exhibit a non-uniform distribution and, finally, above approximately 500km (exosphere), atoms begin to exit into space (Salby, 1996).

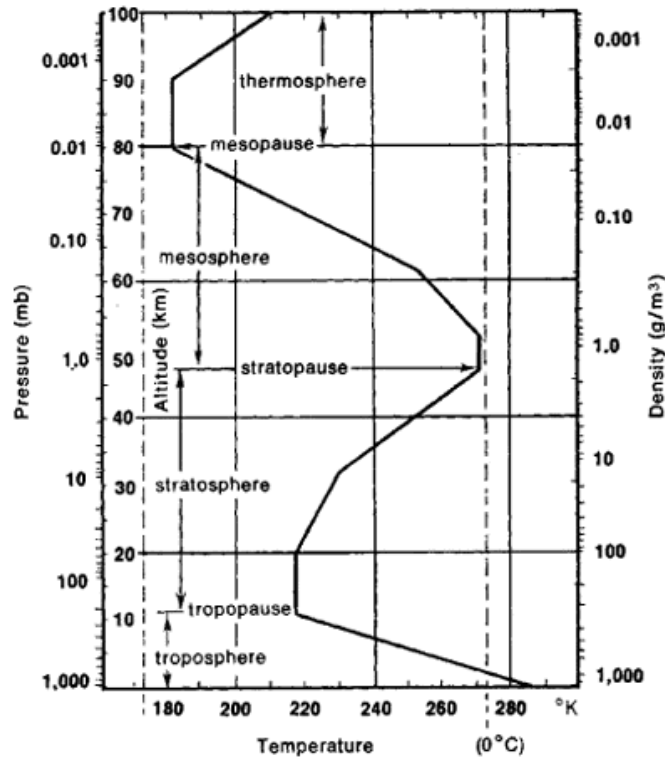


Figure 11. Atmospheric Density, Pressure, Temperature up to 100 km
(From The Free Dictionary by Farlex [as cited in Budyko and Kondratev, 1979])

Due to their higher weights, water droplets and aerosols are typically found in the lower layer of the atmosphere (troposphere). The primary volume, then, in which the atmosphere has the most effect on light propagation, is below 100km and this is the focus area for further inquiry, particularly for atmospheric modeling to be discussed later. The 100 km line is also known as the Karman line, the line which differentiates aeronautics from astronautics (Sanz Fernández de Córdoba, 100km Altitude Boundary for Astronautics, 2013).

2. Atmospheric Absorption

The primary mechanisms by which atmospheric particles interact with light are absorption and scattering. Absorption occurs when the energy contained in incident light of a particular wavelength is sufficient enough to cause a photo-chemical reaction, such as the case below for atomic oxygen disassociation (2.25) (Saha, 2008).



The absorbed light makes or breaks the chemical bonds of the reacting particles; any excess is retained as thermal energy in the products. This thermal energy may later be emitted at longer wavelengths (thermal infrared) (Olsen, 2007) or utilized for bond formation in follow-on chemical reactions.

Because the atmosphere is composed of numerous different elements and particles (e.g., oxygen, nitrogen, water), there exist multiple spectral windows in which absorption occurs. Within these spectral windows (Figure 12), light at the noted wavelengths is no longer propagating and will effectively be filtered out prior to reaching an electro-optical sensor.

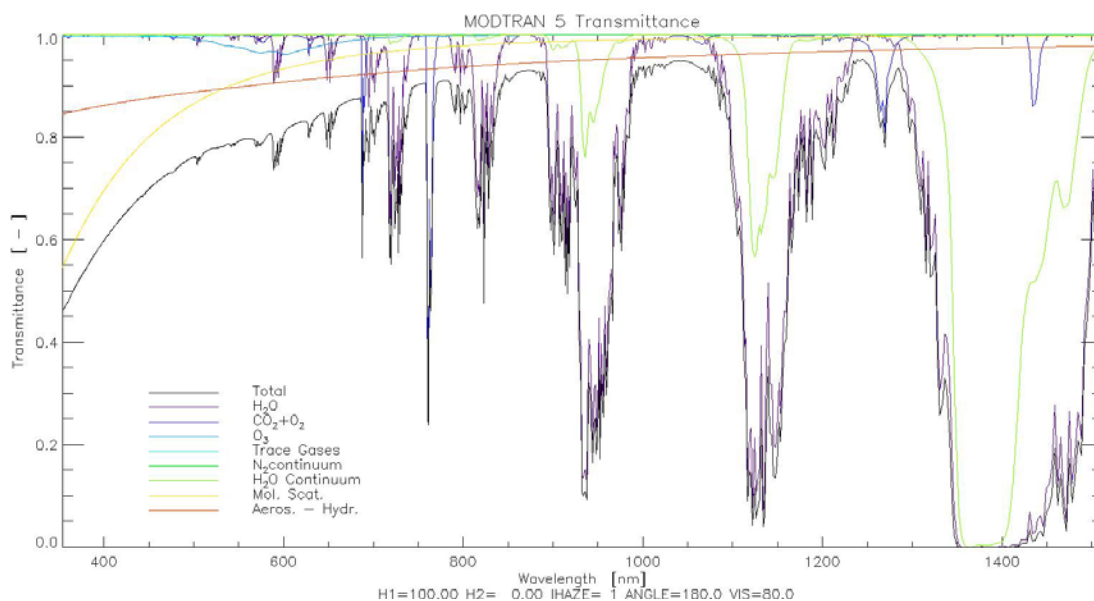


Figure 12. MODTRAN Transmittance Curve

3. Atmospheric Scattering

Where absorption is primarily concerned with the wave nature of light, scattering addresses its particle nature. There are three general categories for this scattering in the VIS to NIR portion of the EM spectrum (Table 1).


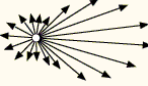
Scattering Type	Particle Size	Wavelength Dependence (in the VNIR range)	Directionality (from left)
Rayleigh	$< 0.1 \lambda$	Short wavelengths	
Mie	$0.1 - 10 \lambda$	Longer wavelengths	
Non-Selective	$> 10 \lambda$	All wavelengths	All directions equally

Table 1. Types of Atmospheric Scattering (data after Jensen, 2007; images from Nave, 2000)

Rayleigh scattering, named for Lord Rayleigh's work in optics in the latter half of the 19th century, was first investigated in an effort to explain the blue color of the sky (Schott, 1997). One of the key results of his work was the derivation of the Rayleigh scattering law (Schott, 1997)

$$\beta_r(\theta) = \frac{8\pi^2 (n(\lambda) - 1)^2}{3m\lambda^4} \left[\frac{3}{4} (1 + \cos^2 \theta) \right] . \quad (2.26)$$

The final term in (2.26), known as the Rayleigh scattering phase function, can be plotted to yield the directionality image in Table 1 which shows that Rayleigh scattering is largely directionally independent, but with slightly greater scattering occurring equally in both the back-scatter and forward-scatter directions. Additionally, because the Rayleigh law is proportional to $\frac{1}{\lambda^4}$, it is clear from Figure 13 that Rayleigh scattering is strongest in the shorter wavelengths, hence the blue color of the sky on a clear day.

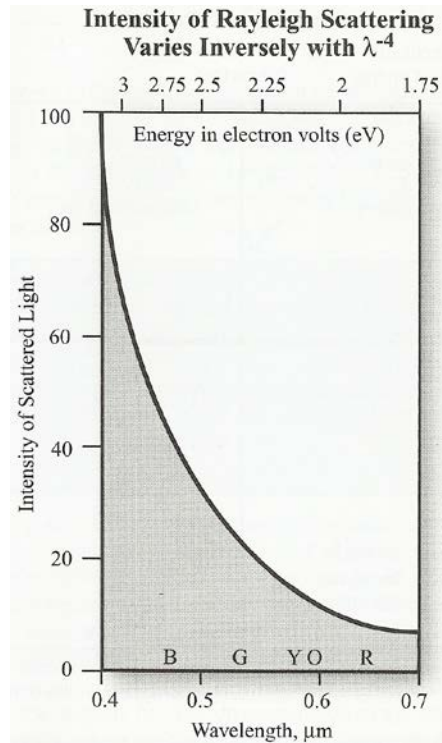


Figure 13. Intensity of Rayleigh scattering varies inversely with the fourth power of the wavelength (λ^{-4}) (From Jensen, 2007)

Rayleigh scattering by atmospheric gases generally takes place in the 2 – 8 km atmospheric range above ground (Jensen, 2007).

The next class of atmospheric scattering, Mie scattering, occurs as light scatters off of very small particulate matter (e.g., mist and dust) and is frequently referred to as aerosol scattering (Schott, 1997). From Table 1, Mie scattering favors the forward direction and is less wavelength dependent than Rayleigh scattering. This type of scattering explains the increased brightness and halo effect when looking in the direction of the sun or bright objects in the presence of mist or fog (Figure 14). Mie scattering generally occurs in the lower 4.5 km of the atmosphere (Jensen, 2007).

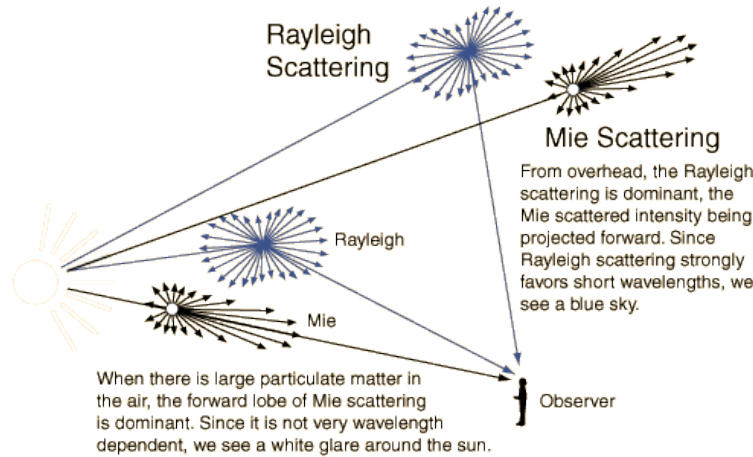


Figure 14. Rayleigh and Mie Scattering (From Nave, 2000)

As atmospheric particulate matter (e.g., raindrops, ice and large ash) increases in diameter to greater than 10 times the wavelength of the incident light, non-selective scattering occurs. In the visible and near infrared (VNIR) range, this form of scattering is both wavelength and directionally independent. Non-selective scattering takes place in the lowest portions of the atmosphere where larger particles are generally found (Jensen, 2007). This form of scattering explains the whiteness of clouds in direct sunlight due to the scattering off of ice and water particles (Olsen, 2007).

Of these three types of scattering, Rayleigh scattering occurs most evenly around the Earth due to the uniform distribution of atmospheric gases. Mie and non-selective scattering are largely dependent on the presence of heavier atmospheric moisture content or aerosol pollutants that are commonly found in urban areas or resulting from localized natural phenomena such as volcanoes or dust storms. What is important to note is that for multi-angle remote sensing, as slant-range viewing distance increases, differences in Rayleigh scattering in the shorter wavelengths should be readily discernible; Mie and non-selective scattering should have little influence.

4. Target and Path Radiance

Fortunately, atmospheric absorption in the VIS to NIR spectrum is negligible, leaving atmospheric scattering as the primary phenomena affecting light on its path from TOA to sensor. The ultimate goal in measuring atmospheric and surface parameters is to

understand and determine the total radiance, L_S , detected by the sensor as the sum of all possible radiance terms resulting from atmospheric and surface interactions (Figure 15).

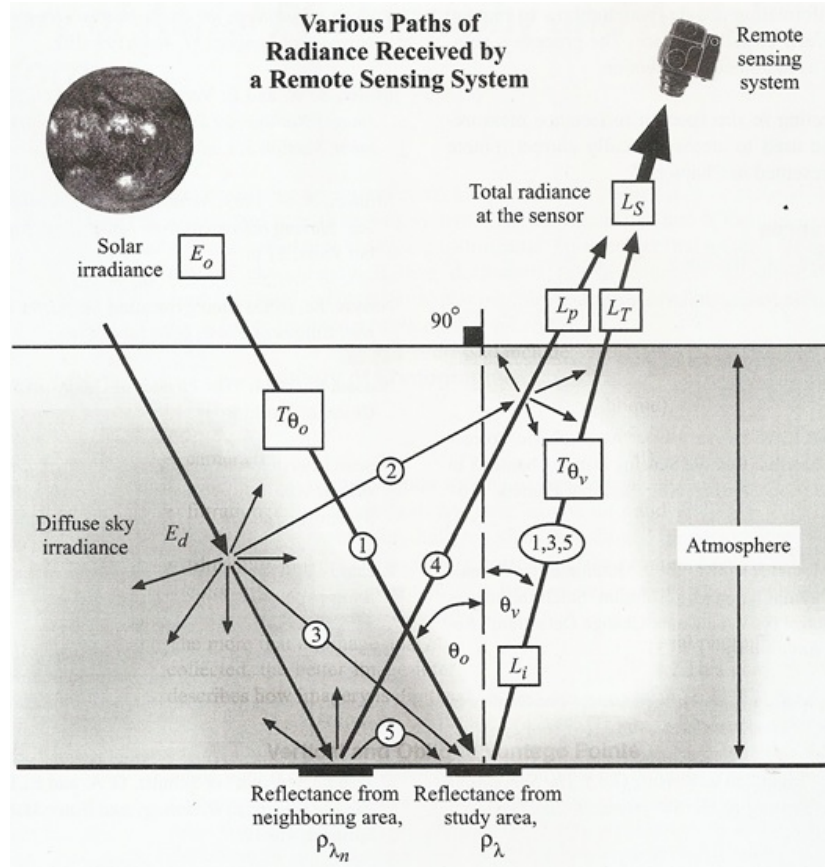


Figure 15. Various Paths of Radiance Received by a Remote Sensing System
(From Jensen, 2007)

Following the approach by Jensen (2007), the first path to consider is the least complicated, beginning with solar irradiance at TOA, E_o , and propagating directly to the ground (path 1 in Figure 15). Atmospheric losses on path 1 light are characterized by directionally dependent transmittance, T_{θ_o} , which accounts for absorption and scattering that never reaches the sensor. The next two paths are the result of TOA irradiance which is scattered before reaching the Earth's surface and is labeled diffuse sky radiance, E_d . The resulting irradiance can be characterized further as (path 2) upwelling sky irradiance that may directly contribute to the radiance detected at the sensor and (path 3)

downwelling sky irradiance that may contribute to the overall irradiance at the surface. Path 3 light, due to the scattering encountered, may be spectrally quite different from path 1 light. The final two paths are those that result from TOA irradiance reflecting off an adjacent surface on the ground with a reflectance value different from the surface of interest: Path 4 light is that which is reflected, passes back through the atmosphere and directly contributes to L_s ; path 5 light reflects off the adjacent surface, but scatters again in the atmosphere such that it illuminates the surface of interest. Again, due to reflection at the adjacent surface, path 4 and path 5 light will be spectrally distinct from the others (Jensen, 2007).

For radiance detected at the sensor, the challenge now becomes how to differentiate the radiance directly attributable to the surface of interest from the radiance that is the result of these different path interactions. Again, from Figure 15, path radiance, L_p , is defined as the radiance at the sensor due to all paths other than that directly attributable to the surface of interest. L_t is the radiance detected at the sensor that is directly attributable to the surface of interest, but, similar to path 1, includes atmospheric transmission losses, T_{θ_v} . These two terms can be combined to provide the total radiance detected at the sensor (Jensen, 2007)

$$L_s = L_p + L_t . \quad (2.27)$$

The radiance at the sensor can now be quantified as a combination of light originating with TOA solar irradiance which is then separated into terms that account for the interactions occurring due to the atmosphere and adjacent surfaces. The challenge for remote sensing, however, still remains to determine the unique radiance of the surface of interest, L_t . If the other path terms remain constant, or can be accounted for by other means (e.g., calibration, atmospheric removal processing), then surface reflectance properties, such as BRDF, should be detectable from a remote sensing platform.

C. PREVIOUS RESEARCH

1. Naval Postgraduate School

a. McConnon Thesis (McConnon, 2010)

BRDF properties were explored using a multispectral band-ratio method applied to 15 WV-2 images of Duck, North Carolina, and 10 WV-2 images of Camp Pendleton, California. Multi-angle band ratio values were extracted for image pairs normalized to the brightest image in each set and then plotted. This method was used to remove atmospheric effects from the data without having to apply additional atmospheric processing. Image histograms for each image set were extracted and plotted by WV-2 band. The results demonstrated that reflectance properties vary based on the separation angles between illumination and sensor positions, and by wavelength.

b. High Spatial Resolution Bidirectional Reflectance Retrieval Using Satellite Data (Olsen, Kim, and McConnon, 2011)

A brief continuation of the work in the McConnon thesis, this effort highlighted the methods and results of the band ratio method to distinguish BRDF properties found within the WV-2 imagery. WV-2 image histograms were also presented demonstrating the variation in brightness for each of the 10 image geometries of the collect over Camp Pendleton, California, (Figure 16). Additionally, this work included the addition of a MODTRAN simulation based on the image geometry and other parameters found in the Camp Pendleton collect; this simulation, for all intents and purposes, was the starting point for the work in this thesis.

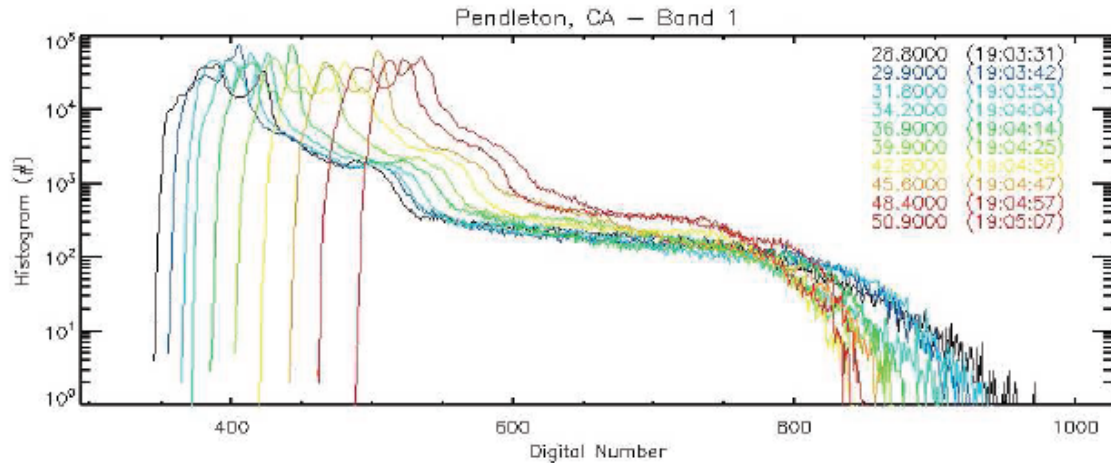


Figure 16. Histogram of brightness values for spectral channel 1 (400-450 nm) over Camp Pendleton, CA (From Olsen et al., 2011)

Eight histograms, similar to Figure 16, were generated for the WV-2 imagery in this thesis and can be found, along with a brief analysis, in Appendix D.

c. *Lee Thesis (Lee, 2012)*

Bathymetry analysis was conducted using thirty-nine multispectral WorldView-2 images collected over Oahu, Hawaii. A multi-angle band ratio method was applied to the images using image pairs in the COASTAL, BLUE, GREEN and YELLOW WV-2 bands. Depth derivations from this method were then compared to actual depth information for the regions analyzed. Results demonstrated that depth values derived from the most-nadir images provided more accurate depth values than those collected off-nadir.

2. Other Research

Several satellites have been launched within the last two decades with capabilities that, for all intents and purposes, ushered in the study of multi-angle reflectance within the field of satellite remote sensing. Two of these are listed below.

a. *MISR*

NASA's Multi-angle Imaging Spectro-radiometer (MISR) was launched in 1999 aboard the Terra EOS AM-1 satellite at a 705 km sun-synchronous orbit (NASA

JPL, 2013). MISR employs nine cameras which can image the Earth simultaneously from nadir, 26.1, 45.6, 60 and 70.5 degrees (both fore and aft) and is shown in Figure 17 (NASA JPL, 2013).

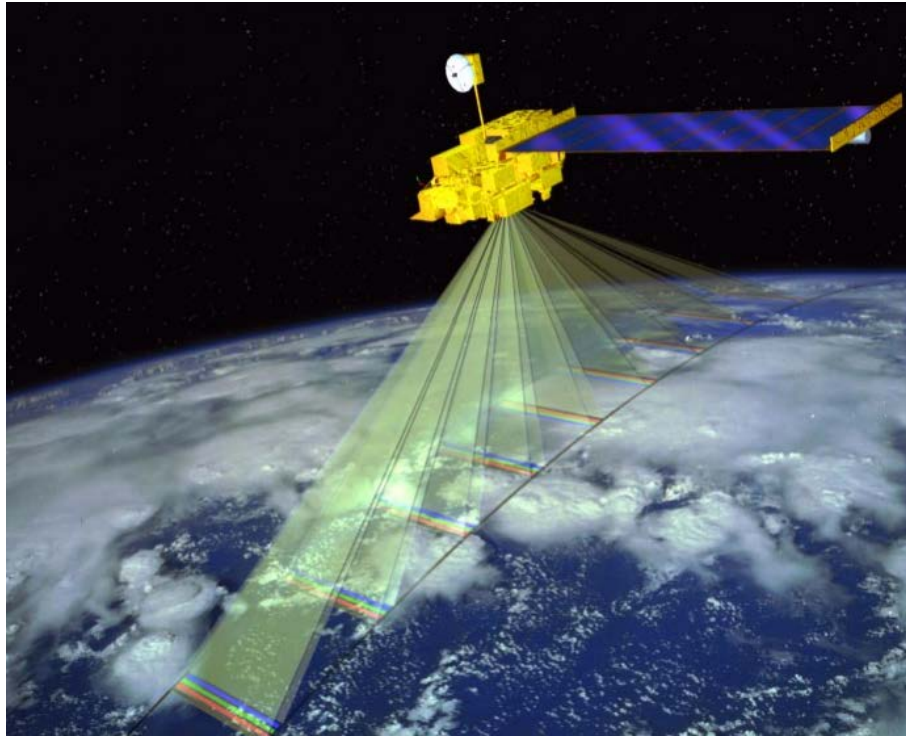


Figure 17. Multi-angle Imaging Spectro-radiometer (From NASA JPL, 2013)

MISR-produced imagery has contributed to numerous research activities over the last decade in the study of aerosols, surfaces and clouds; many publications can be found on NASA's Jet Propulsion Laboratory MISR website (NASA JPL, 2013). Specific to studies of bidirectional reflectance, MISR data has assisted the measurement and characterization of seasonal changes in background reflectance for forest canopies, efforts which contribute both temporally and spatially to ecosystem modeling (Canisius & Chen, 2007). From a practical standpoint, studies using multi-angle MISR imagery over water have shown that oil slick appearance varies predictably as view angle changes, a phenomenon that can enhance "the reliability of automatic oil detection" (Chust & Sagarminaga, 2007).

b. CHRIS

The Compact High Resolution Imaging Spectrometer (CHRIS), a program of the European Space Agency (ESA), was launched in 2001 on the PROBA-1 satellite (Figure 18) into a 600 km polar orbit (ESA, 2013). CHRIS' objective "is the collection of BRDF (Bidirectional Reflectance Distribution Function) data for a better understanding of spectral reflectances" (ESA, 2013). Similar to the methods of this thesis, multi-angle CHRIS data has been used to validate canopy BRDF models generated using PROSPECT and SAILH radiative transfer models (D'Urso, Dini, Vuolo, Alonso, and Guanter, 2004). More recently, multi-angle CHRIS imagery sets have been used to advance studies in estimating aerosol optical depth (AOD) (Davies, North, Grey, and Barnsley, 2010). In addition to BRDF studies, CHRIS has been instrumental in atmospheric, agricultural, land and ocean/coastal studies (ESA, 2013).



Figure 18. "Agile PROBA-1 rolls in its orbit to take images" (From ESA, 2011)

III. DATA AND METHODS

A. DATA

1. Source and Data

a. Worldview-2 Satellite

The WorldView-2 (WV-2) commercial satellite (Figure 19) is owned and operated by DigitalGlobe, Inc., based out of Longmont, CO.



Figure 19. WorldView-2 Satellite (From DigitalGlobe)

WV-2 is DigitalGlobe's second next-generation electro-optical platform. It is configured with a single panchromatic band sensor and eight multispectral band sensors at lower spatial resolution (Table 2) (DigitalGlobe, Inc., 2013).

Sensor		Wavelength (nm)	Resolution
Panchromatic		450–800	0.46 m GSD (nadir); 0.52 m GSD @ 20 deg off-nadir
Mult-spectral	Coastal	400–450	1.85 m GSD (nadir); 2.07 m GSD @ 20 deg off-nadir
	Blue	450–510	
	Green	510–580	
	Yellow	585–625	
	Red	630–690	
	Red Edge	705–745	
	Near IR 1	770–895	
	Near IR 2	860–1040	

Table 2. WorldView-2 Sensor Characteristics (After DigitalGlobe, Inc., 2013)

The satellite operates at an altitude of 770 km in a sun-synchronous orbit with period of 100 minutes, allowing a best-case revisit of 1.1 days with a collection capacity of 1 million square kilometers per day (DigitalGlobe, Inc., 2013). Using precision control moment gyros for attitude control, WV-2 can slew 300 km in 9 seconds (DigitalGlobe, Inc., 2013), a capability allowing the capture of multiple images within the same target pass. All of these features make the WorldView-2 satellite particularly well-suited for the gathering of multi-angle, multispectral imagery pertinent to this research.

b. Rio de Janeiro Imagery

For this study, DigitalGlobe provided eight WorldView-2 digital images centered over Rio de Janeiro, Brazil. These images were collected over a five minute period in the late morning (1000 local) as the satellite passed from north to south over the target area. Collection date was 19 January, 2010, which, for the southern hemisphere, is the summer season. Imagery details can be found in Table 3 and Figure 20. At the time of collection, the sun was east of the scene at a zenith angle (measured from scene normal) of approximately 26 degrees. The image collected closest to satellite nadir is labeled P008 and was collected as the satellite was 8.7 degrees from zenith.

Image #	Acq Date	Acq Time	Solar Zenith (deg)	Solar Azimuth (deg)	Satellite View Zenith (deg)	Satellite View Azimuth (deg)	Mean GSD
P002	2010-01-19	13:08:25.727350	26.9	90.1	60.3	13	5.016
P006	2010-01-19	13:09:13.994750	26.7	90.1	48.4	12.9	3.309
P007	2010-01-19	13:09:54.935950	26.5	90	34	12.8	2.429
P008	2010-01-19	13:10:47.253138	26.3	89.9	8.7	9.5	2.019
P005	2010-01-19	13:11:38.417250	26.1	89.8	20.2	193.2	2.062
P003	2010-01-19	13:11:59.732850	26	89.8	30.1	193	2.293
P001	2010-01-19	13:12:40.374850	25.9	89.7	45.3	192.9	3.053
P004	2010-01-19	13:13:37.632850	25.6	89.6	59.8	192.7	4.937

Table 3. Rio de Janeiro Imagery: Date, Time, and Geometry

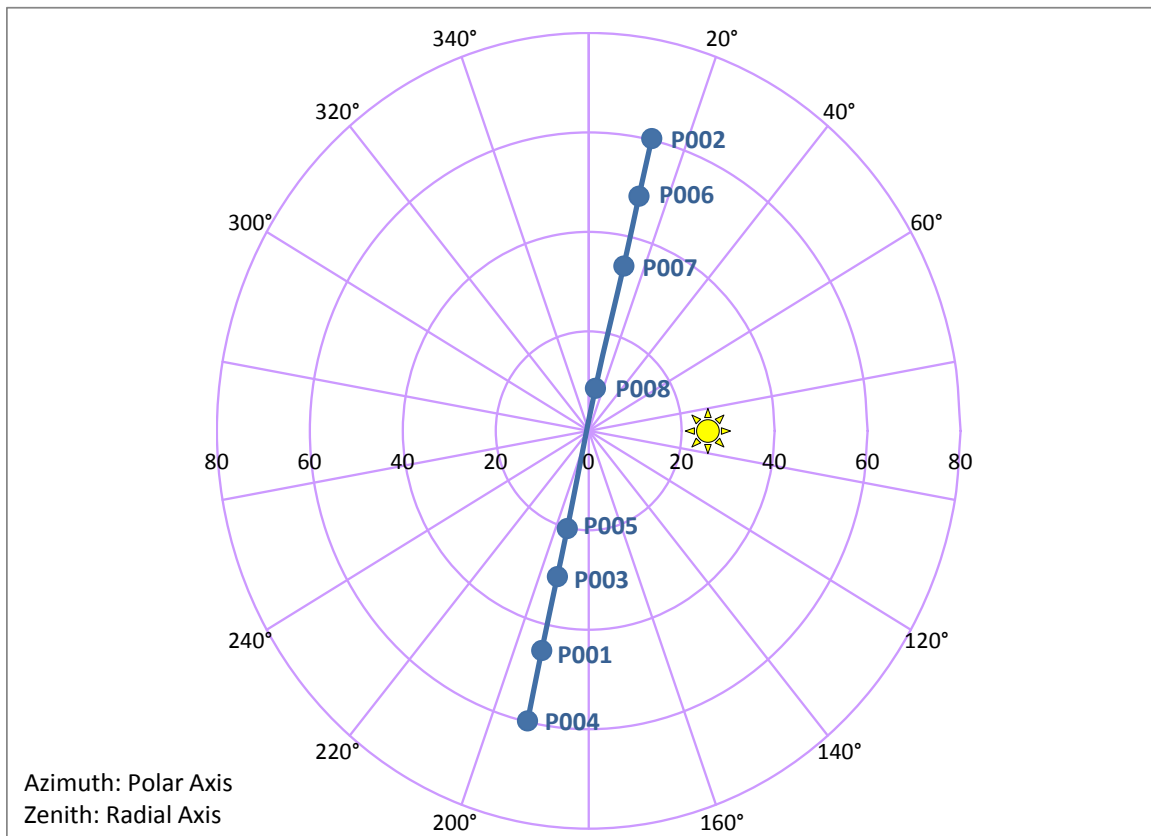


Figure 20. Rio de Janeiro Imagery: Satellite and Solar Geometry

DigitalGlobe provides imagery with varying levels of pre-processing and geolocation accuracy (each type discussed in *DigitalGlobe's Core Imagery Product Guide* [DigitalGlobe, Inc., 2013]); the imagery used in this research was provided as "BASIC1B." As its name implies, this level of imagery has basic sensor radiometric correction applied, but has not been ortho-rectified. DigitalGlobe's imagery metadata

document (IMD), provided with the data, allows simple geo-accuracy and radiance calculations for correction of the imagery (DigitalGlobe, Inc., 2013). Each of the eight images provided contained a panchromatic and multispectral image in NITF format, an IMD and numerous other descriptive and supporting files. The only files used in this study were the multispectral images and associated IMD files.

2. Tools

a. ENVI

In this study, the primary software application used for the processing, manipulation and analysis of the Rio de Janeiro imagery was the Environment for Visualizing Images (ENVI), version 5.0, by Exelis Visual Information Solutions, Inc. ENVI is fully capable of handling multispectral imagery in various formats and all spatial sub-setting (chipping), registration, WV-2 radiance correction, and statistical (histogram) outputs were performed using tools within the ENVI suite. Additionally, ENVI provides numerous reference spectral libraries which can be used for comparison when analyzing imagery. FLAASH, the Fast Line-of-Sight Atmospheric Analysis of Spectral Hypercubes module based on the MODTRAN4 radiation transfer code (ITT Visual Information Systems, Inc., 2009), is also included with ENVI and can be used to process radiance-corrected imagery into atmospherically corrected surface reflectance.

b. MODTRAN and MODO

The Moderate Resolution Atmospheric Transfer code (MODTRAN5) was used to model atmospheric conditions similar to those found in the WV-2 imagery. As its name implies, MODTRAN is a medium resolution (0.2 cm^{-1} wavelength increment over the UV to far IR range) radiative transfer band-model code that can calculate numerous forms of atmospheric transmittance and radiance (Berk, Anderson, Acharya, & Shettle, 2011). This is accomplished numerically by modeling the atmosphere in horizontally stratified homogenous layers, each with unique vertical profiles based on thermodynamic parameters as well as molecular and particulate (aerosol) composition. To simplify initial MODTRAN usage, several atmospheric reference models are included that the user can

select based on the global region in which analysis is desired (differentiated by latitude and season) (Figure 21).

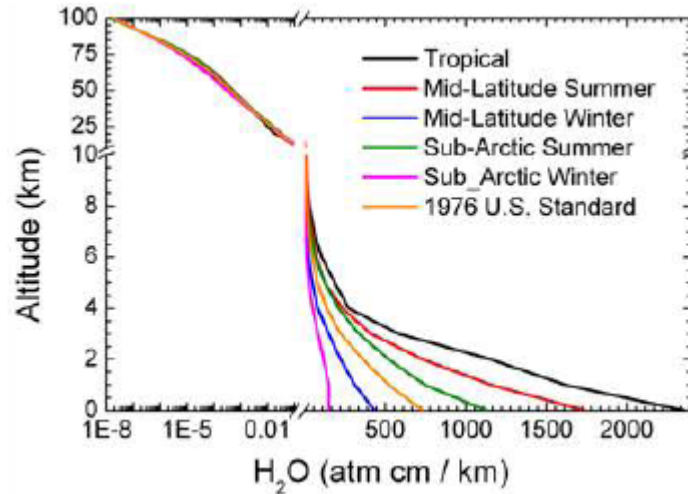


Figure 21. MODTRAN Atmospheric Profiles for H₂O Composition by Altitude
(From Berk et al., 2011)

MODTRAN is also capable of accepting custom atmospheric inputs should the user desire to deviate from the reference models provided. In addition to the initial profile selection, MODTRAN also requires inputs defining the path geometry and will also accept supplemental sensor and surface reflectance parameters (to name a few) that the user may wish to include in the calculation. The maximum TOA MODTRAN altitude is 100 km (Berk et al., 2011) which, for reasons discussed in section II.B.1, is adequate for the analysis in this research.

MODO, a MS Windows-based GUI for MODTRAN, was the primary tool used in this thesis to generate MODTRAN models. A screenshot of the MODO GUI shows some of the available MODTRAN parameter options (Figure 22).

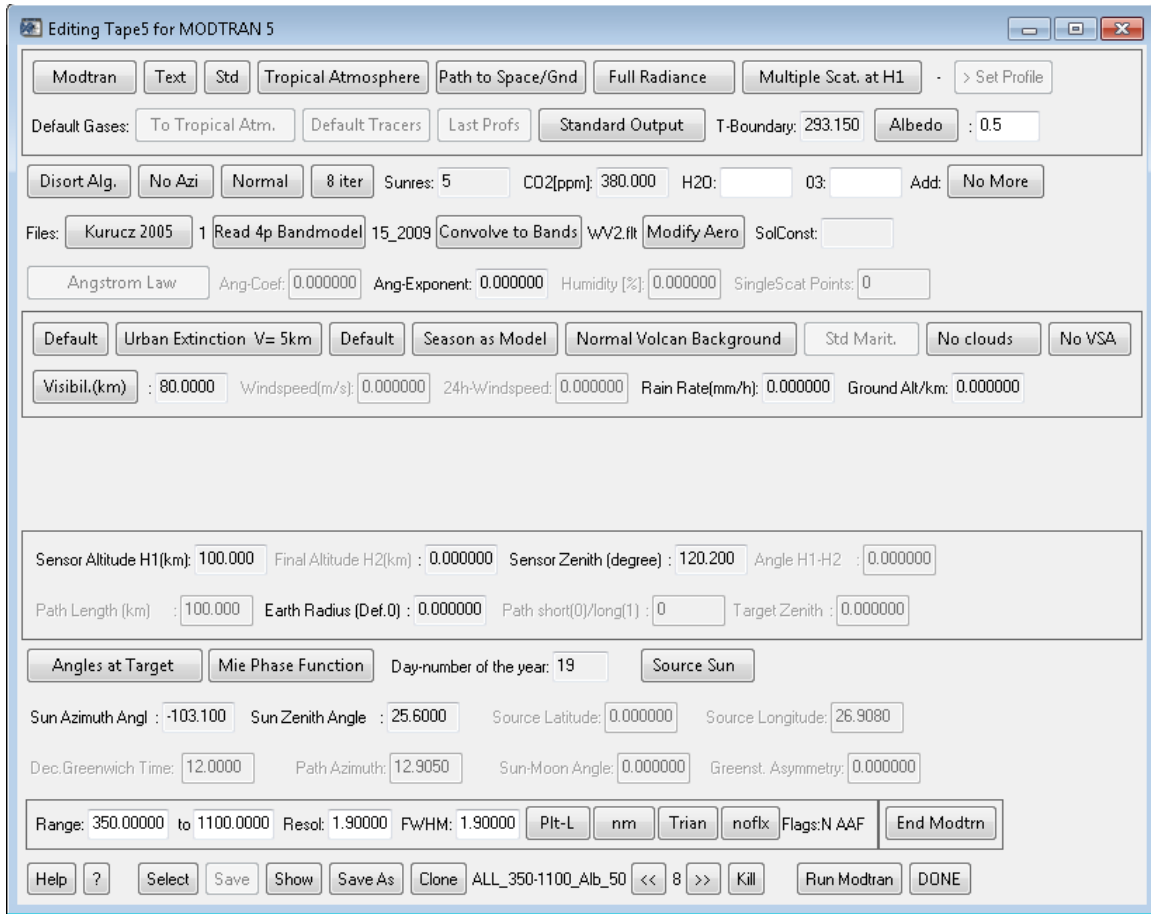


Figure 22. Screenshot of MODO Graphical User Interface

B. IMAGE PREPARATION

Useful per-pixel top-of-atmosphere WV-2 radiance values that can be adequately referenced between images are the desired measures necessary for the multi-angle analysis described in this thesis. Several steps were necessary to derive these values from the provided WV-2 imagery. These steps, described below, required both qualitative and quantitative analysis of the WV-2 data.

1. Image Organization and Multi-Angle Assessment

All imagery was consistently provided by DigitalGlobe as BASIC1B products. The data contained in the IMD file for each image was first parsed and presented in tabular format using Microsoft Excel. From this table, it was then possible to determine the order of the images based on acquisition time as well as determining the sensor and

solar geometry for the entire image set (data which facilitated the creation of Table 3 and Figure 18). As the study of multi-angle effects was the primary objective of this study, separation angles between solar and sensor view directions, referenced to the scene center of each image, were calculated. The resulting separation angles are displayed in Figure 23 and show that the imagery is satisfactory for studying multi-angle reflectance properties. The separation angle between the most nadir image (P008) and the images collected before and after are approximately evenly spaced, with the extremes (P002 and P004) at least 30 degrees separated from P008.

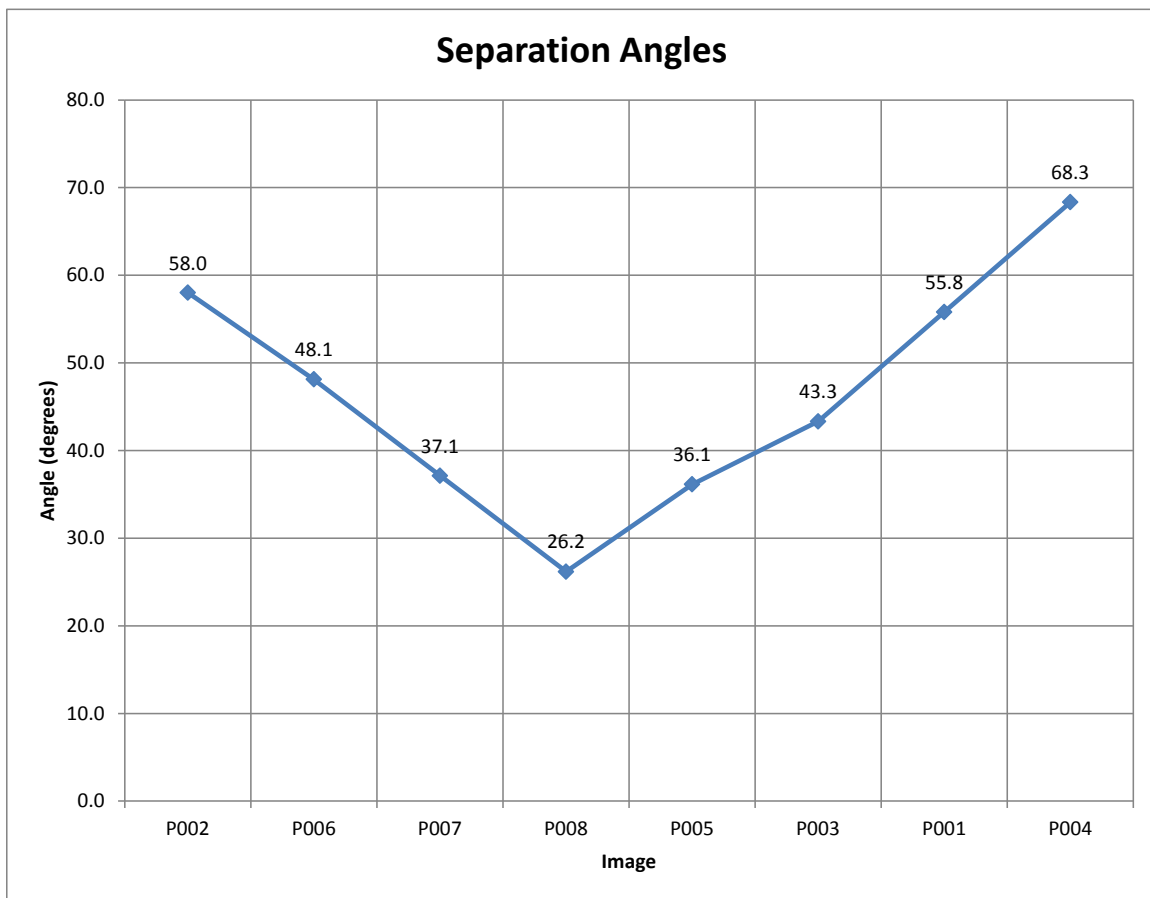


Figure 23. Separation Angles of the Eight Rio de Janeiro WV-2 Images

2. Spatial Sub-setting

From the IMD file, and simply by looking at the images as provided, it was apparent that they were not all of the same dimensions, an expected effect of the off-nadir

collection. Consequently, a consistent subset common to all eight datasets was determined and extracted for further analysis (Figure 24). An added benefit of the smaller image chip was increased speed of processing. Furthermore, in an effort to minimize the effects of terrain on reflectance measurements at the WV-2 sensor, these subsets were also chosen to be as topographically flat as possible. Fortunately, even though Rio de Janeiro contains numerous hills and sloped contours, it is a coastal city and relatively flat areas exist at the beaches and close to the coastline. The coverage area chosen is shown as the highlighted area in Figure 24.

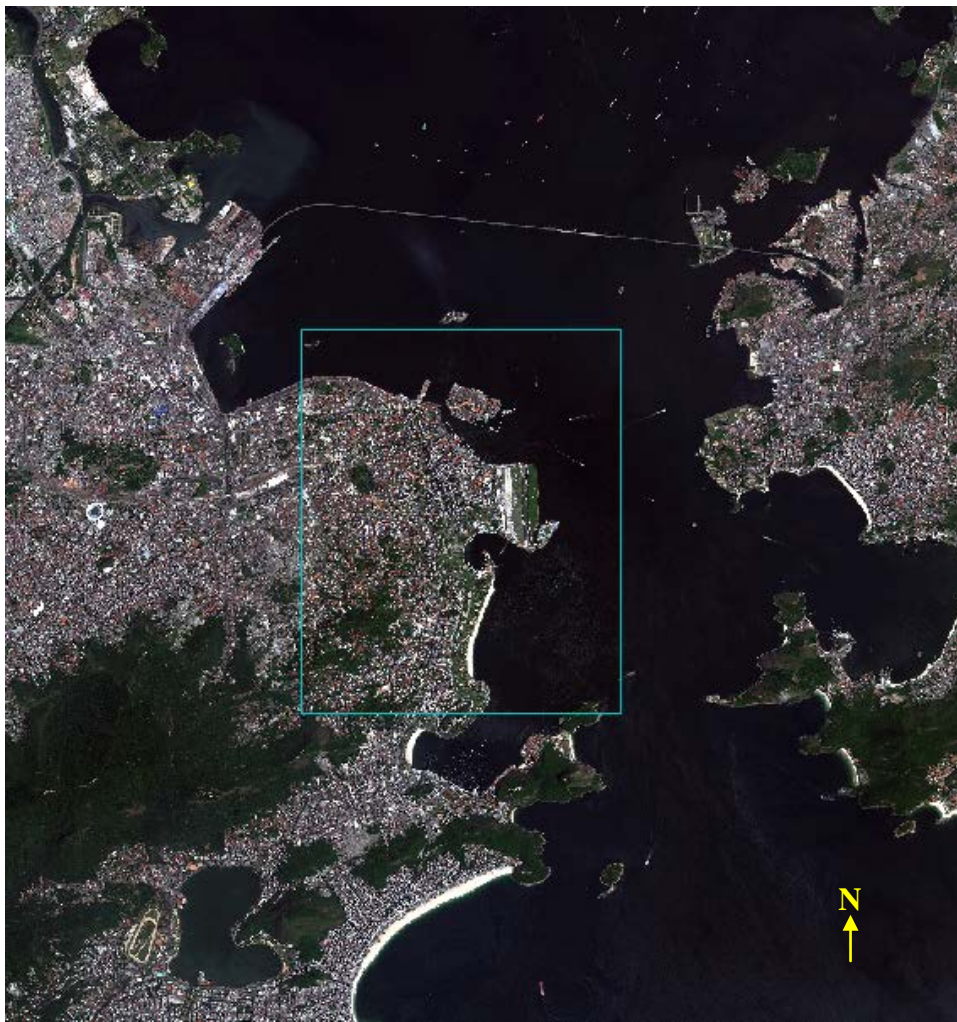


Figure 24. True color image chip from P008 (WV-2 bands 5, 3, 2 (RGB), approximate image center $22^{\circ}54'30''$ S, $43^{\circ}10'00''$ W, approximate image dimensions 17 km x 17 km)

Figure 25 is a side-by-side display of the chosen image chip and a terrain map of the same region from Google Maps. The Santos Dumont Airport is present within this chip, containing numerous flat and consistent surfaces such as asphalt runways, grassy fields, and concrete. A beach is located to the south of the airport, providing a bright contrast to many of the pixels within the chip. Numerous other topographically flat surfaces are present in the narrow strip just west of the beach and east of the highway (Vevd. Da Perimetral). This particular image chip is also located near the scene center for each of the eight images and, hence, the solar and view geometry remain valid and consistent.

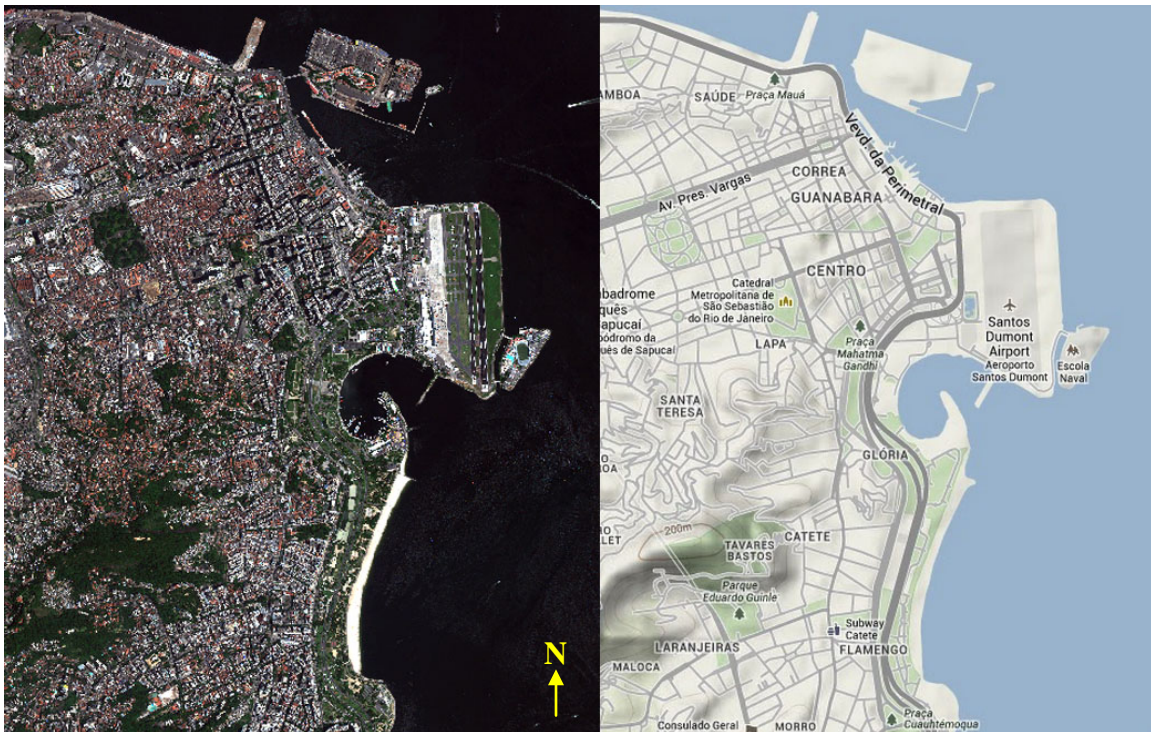


Figure 25. Image chip P008 Side-by-side with Google Terrain Map (left side WV-2 bands 5, 3, 2 (RGB), approximate image center $22^{\circ}54'46''$ S, $43^{\circ}10'35''$ W, approximate image dimensions 4 km x 5 km; right side from Google Maps, 2013)

Using P008 as the reference chip, all other images were reduced to spatial subsets of similar size. It is worth emphasizing that the chips did not, at this point, represent the same spatial subset by geographic reference but only by pixel locations defined by the

reference chip. Fortunately, each chip contained the areas of interest (airport and beach) which would be used for further analysis.

3. Top-of-Atmosphere Radiance Correction

ENVI contains a built-in tool for the conversion of WV-2 per-pixel digital number values—which are actually relative radiance values already radiometrically corrected in the delivered BASIC1B product—to absolute TOA radiance values for each multispectral band of the WorldView-2 sensor. This conversion makes use of the following equations (Updike et al., 2010)

$$L_{pixel,band} = absCalFactor_{band} \cdot q_{pixel,band} \quad (3.1)$$

$$L_{\lambda_{pixel,band}} = \frac{L_{pixel,band}}{\Delta\lambda_{band}} \quad (3.2)$$

in which $absCalFactor$ and $\Delta\lambda_{band}$ are both found in the IMD file and $q_{pixel,band}$ is the digital number per pixel in the image. The background and derivation of these equations specific to the WorldView-2 satellite can be found in (Updike et al., 2010). As part of the radiance conversion, a scale factor must be applied which is essentially a conversion to the form of radiance units desired. Using both the digital number and the values for $absCalFactor$ and $\Delta\lambda_{band}$ provided by the IMD fill will result in units of $\frac{W}{m^2 \cdot sr \cdot \mu m}$. The

FLAASH atmospheric correction software expects the radiance conversion to result in units of $\frac{\mu W}{cm^2 \cdot sr \cdot nm}$. A scale factor of 10 is, therefore, necessary. Because this analysis later compared these radiance values to those generated using MODTRAN, having the units in $\frac{\mu W}{cm^2 \cdot sr \cdot nm}$ was actually expedient.

4. Image Registration

Following TOA radiance correction, the challenge was then to develop a method to consistently reference similarly located pixels across all eight images. Because the viewing geometry varied across the imagery set by as much as 60 degrees, foreshortening

resulted in a slight visible distortion of objects within the images as well as a shift in position based on view direction. Registration is a process that attempts to correct for the positional distortion by adjusting each image (warp images) to a reference image (base image). ENVI version 5 has a robust registration workflow that was applied to every image except P008 which, as the most nadir image, possessed the least distortion and was chosen as the seed image. Using approximately 50 tie points per warp-base pair and Delauney triangulation as the warping method resulted in surfaces within the areas of interest that were consistently located across the set for further analysis using regions of interest.

5. Regions of Interest and Statistical Outputs

A region of interest (ROI) is a unique portion of an image specifically designated and defined by the user that can greatly ease the extraction of statistical data from the image. These objects can be formed as polygons, polylines or pixels. Once created and saved, an ROI can be reconciled by map with all other images in the set, provided that the reference position of objects within each image (i.e., the pixel map) is the same across the image set. Because all of the images were adequately registered, the use of ROI's was appropriate and greatly eased the extraction of data for similar surfaces within each image. Each of the ROI's chosen for analysis was sized at 9x9 pixels, or smaller, in order to minimize any registration errors. The ROI's chosen were (1) a grassy area just east of the runway, (2) an asphalt section of the runway and (3) a section of sand slightly west of the beach (Figure 26).

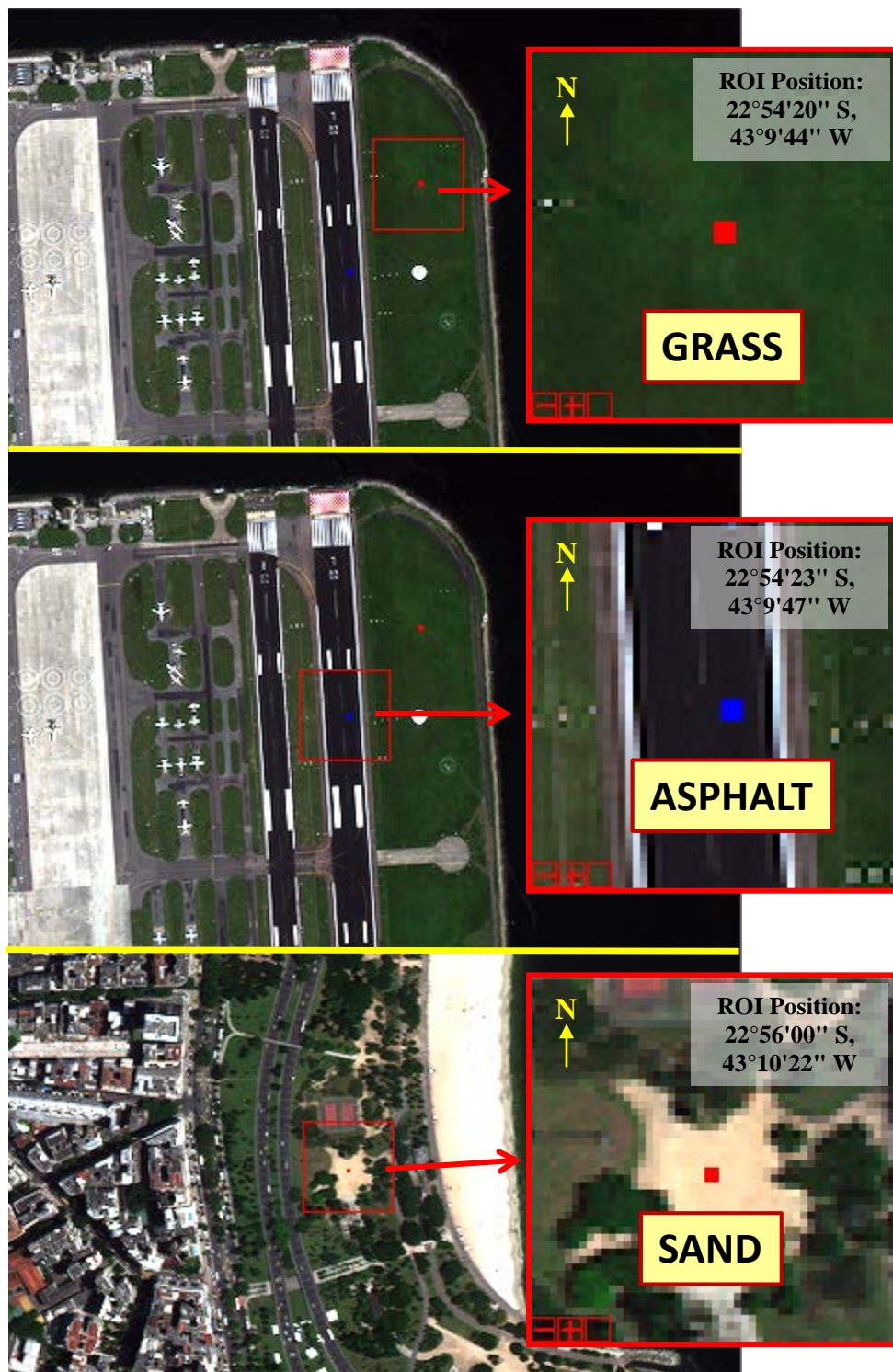


Figure 26. ROI's Used in the Imagery Analysis, Displayed on Image P008 (WV-2 bands 5, 3, 2 (RGB), approximate image dimensions 1 km x 0.5 km)

Following ROI reconciliation in each image, statistical data were extracted for each ROI and saved. Each statistical data file, organized by WV-2 band, consisted of basic data (minimum, maximum and mean digital number values) followed by the actual DN for each pixel contained in the ROI. This information was then parsed into Microsoft Excel for analysis and graphical presentation. An example ENVI statistical data file can be found in the Appendix, Section A.

C. ATMOSPHERIC MODELING

MODO was the primary tool used for MODTRAN modeling in this thesis.

1. Model Parameters

a. Atmospheric Values

The starting point for the determination of MODTRAN input parameters was the Rio de Janeiro imagery. The location and time of year dictated the choice of a tropical atmospheric model with an urban aerosol profile. Due to the very clear conditions present in the imagery (less than 1.6% cloud cover in P008), a visibility of 80 km was chosen as an override to the 5km default of the urban profile. The more CPU-intensive DISORT (Discrete Ordinates Radiative Transfer Program) was selected over the 2-stream Isaac's model algorithm for multiple scattering calculations. Carbon dioxide concentration was set to 380 ppm. No other modifications to the default atmospheric settings were made.

Determining the geometry inputs was a two-fold process. The first step is defining the atmospheric processing path from ground to sensor (i.e., sensor geometry). The choices available are: (1) *horizontal path*, used for very short ranges within a single homogeneous atmospheric layer; (2) *slant path to space*, which, as the name implies, calculates from the ground up to the maximum processing altitude allowable; and (3) *slant path*, which processes from a user-dictated start and stop altitude (between ground and maximum allowable) (Ontar Corporation, 2009). *Slant path to space* was chosen because the altitude of the WV-2 sensor is well above the maximum MODTRAN processing altitude of 100 km. The parameters required to describe the sensor geometry

are the height, $H1$, of the sensor above ground (in kilometers) and the zenith angle, ϕ , as shown in Figure 27. For clarity, a sensor directly over the target would have a zenith angle of 180 degrees. It is important to note that there is no term to describe the azimuthal position of the sensor; this will be included in the input for the solar geometry.

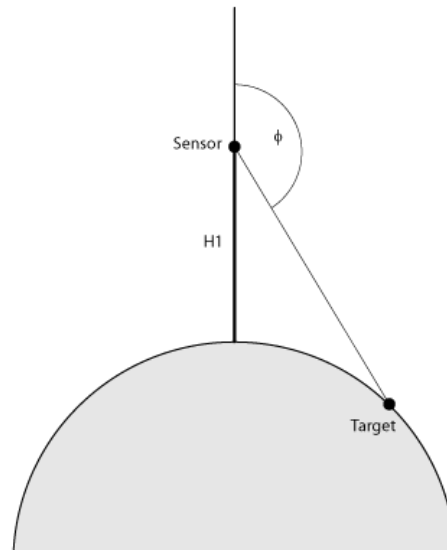


Figure 27. MODTRAN Sensor Geometry

In defining the solar geometry—the second step—the input determination is more complex because the azimuth value is referenced relative to the view direction of the sensor. The relative azimuth input can only range in value from -180 degrees to 180 degrees, with negative values indicating the sensor is left of the sun, positive values to the right (if viewed from above). As the azimuth values provided in the IMD file are all referenced to true north, the calculation of the relative azimuth is a simple mathematical exercise. The solar zenith is measured similar to that of the sensor geometry. Figure 28 depicts values required for the solar geometry and Table 4 lists all the values for sensor and solar geometry used in this research.

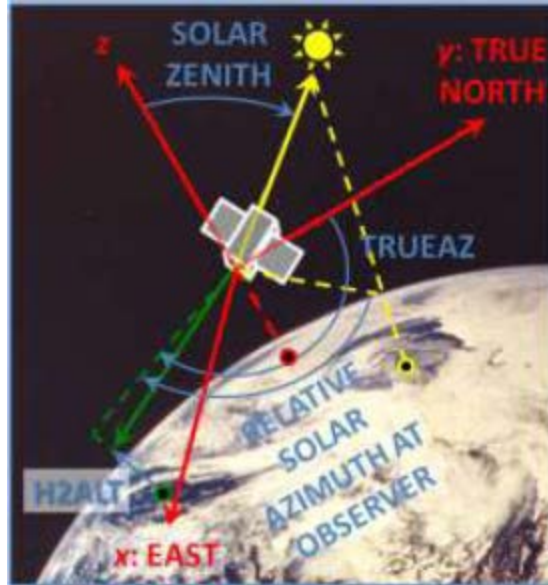


Figure 28. MODTRAN Solar Geometry (From Berk et al., 2011)

Image Model	Solar Zenith (deg)	Sensor Zenith (deg)	Relative Azimuth (deg)
P002	26.9	119.7	77.1
P006	26.7	131.6	77.2
P007	26.5	146	77.2
P008	26.3	171.3	80.4
P005	26.1	159.5	-103.4
P003	26	149.9	-103.2
P001	25.9	134.7	-103.2
P004	25.6	120.2	-103.1

Table 4. MODTRAN Solar and Sensor Geometry Inputs

a. Surface Reflectance Inputs

MODTRAN version 5 provides several options for the selection of surface reflectance properties of the image pixel. In the simplest case, albedo values can be directly entered ranging from 0 (completely dark) to 1 (100% reflection—brightest value). Surface reflectance values can also be entered by use of a spectral albedo text file specific to a surface of interest. This file must adhere to a specific formatting structure containing two columns of which one is for wavelength and the other the associated reflectance value (ranging, again, from 0 to 1). MODTRAN provides a useful tool that can

convert ENVI surface reflectance library files (*.sli) into the format required by MODTRAN. Use of both directly entered albedo values and spectral albedo text files were used in this thesis.

Two remaining special options—“LAMBER” and “BRDF”—are also available. The “LAMBER” selection signals to MODTRAN to also calculate the adjacency effects of the region surrounding the image pixel; this option requires the selection of two reflectance files. The “BRDF” option allows the user to select one of several kernel-based algorithms for BRDF modeling of the image pixel. The input parameters required for the numerical calculations of the latter case were not available for this research. Neither of these options was used in this thesis and each is mentioned only for completeness.

It is important to note that MODTRAN models image point reflectance as Lambertian. A Lambertian surface is an ideal diffuse reflector in which incident irradiance is reflected equally into all directions; hence, reflected radiance is constant in all directions (Schott, 1997). This property will become significant during the forthcoming analysis.

b. Frequency Range and Resolution

To match the multispectral wavelength range of the WV-2 satellite (400–1040 nm), a MODTRAN wavelength processing range of 350–1100 nm was set for all tape5 files. Because of this wide frequency range, it was not necessary to calculate values at MODTRAN’s best-case resolution of 0.2 cm^{-1} . Instead, the 15 cm^{-1} band model was selected, increasing the speed of processing for each MODTRAN run.

c. WorldView-2 Sensor Characteristics

For default MODTRAN radiance processing, tabular output is generated covering the entire wavelength range chosen and incremented according to the specified resolution. The WV-2 multispectral sensor, however, detects and measures radiance values for all photons that fall within each wavelength band of its eight multispectral sensors. WV-2 detected output is, therefore, not generated as a continuous range of

radiance values over the entire wavelength range, but as discrete values of radiance specific to the band of detection. To model this adequately, a WV-2 spectral response filter file was generated that allowed MODTRAN to spectrally convolve the calculated radiance to each of the WV-2 spectral bands. Similar to a spectral albedo file, a spectral response filter file must be strictly formatted in two columns, one for wavelength, the other the response value ranging from 0 to 1. When a spectral response filter file is used, an additional MODTRAN output file, with extension *.chn, will be generated listing the convolved radiance values.

2. MODTRAN Input Template Creation

MODTRAN model outputs were required to investigate the effects of both increasing general surface brightness (albedo) and surface reflectance properties similar to that for the ROI's displayed in Figure 26.

a. Input Template Organization and Batch Processing

Eight MODTRAN-unique template files (*.tp5) were initially created using previously discussed atmospheric parameters, image geometry and the WV-2 spectral response filter file. Each file was then ordered for batch execution in MODO according to the image acquisition time (Table 3). An added benefit to using MODO was that once a batch execution was established, a single template file could also be saved containing all information for each of the eight original template files. This effectively created a master template upon which all further MODTRAN runs could be based, ensuring consistency in both geometry and atmospheric parameters while simultaneously minimizing input errors.

b. Albedo Calculations

Five MODTRAN templates were used to create models with varying surface albedo values. Once a template was loaded into MODO, the desired spectral albedo value was manually entered per iteration, executed and then saved. Albedo values used in this analysis were 1%, 25%, 50%, 75% and 100%.

c. Surface Reflectance Calculations

Three MODTRAN templates were used to create models with surface reflectance values comparable to the ROI's of GRASS, ASPHALT, and SAND. The following surface spectral reflectance library files were used: (1) GRASS provided with ENVI in the Johns Hopkins University spectral library (Baldrige, Hook, Grove, & Rivera, 2009), (2) ASPHALT_DARK provided with MODO in the ATCOR spectral library (DLR, n.d.) and (3) LIGHT YELLOWISH BROWN LOAMY SAND downloaded from the soils section of the online ASTER Spectral Library database (Baldrige et al., 2009). Plots of each of these libraries are displayed as Figures 36, 39 and 42 in Chapter IV.

3. Model Outputs and Processing

a. Outputs and Processing

MODTRAN produces a standard output file (*.tp7) per run (Berk et al., 2011). This file is organized by wavenumber and contains 16 columns of calculated values, some of which are total radiance, ground reflected radiance and solar scattered (path scattered) radiance. This file was used to generate all albedo-only plots.

In addition to an output file, whenever a sensor response filter file is employed in the MODTRAN input parameters, a channel output file (*.chn) is also generated (Berk et al., 2011). This file is organized by the bands established in the spectral response filter file and provides MODTRAN-calculated spectral radiance associated with each band. This file was used to generate all surface reflectance plots.

Microsoft Excel was used for the processing of all MODTRAN outputs. Data files were imported into Excel, organized and parsed. Plots were then generated using Excel's built-in charting features and used for analysis.

IV. RESULTS AND ANALYSIS

Initially, MODTRAN radiance plots were generated using geometry and atmospheric conditions similar to the imagery. After evaluation of the initial model data represented by these plots, surface reflectance plots were then generated using surface reflectance spectral libraries similar to those chosen for analysis within the imagery. Comparative analysis was then conducted between the MODTRAN data plots and imagery data plots.

Radiance units used in all plots are $\frac{\mu W}{cm^2 \cdot sr \cdot nm}$.

A. MODTRAN ALBEDO MODELS

1. WV-2 Spectral Band and Image Geometry Plots

The surface reflectance parameters of these models were set solely to albedo values ranging from 1% (darkest) to 100% (brightest) in 25% increments. All ten plots can be found in Appendix B. Plots for albedo values of 1%, 25% and 50% are shown in Figure 29. Each albedo is displayed as a set: (1) Radiance vs. Band and (2) Radiance vs. Image Geometry. Plots for 75% and 100% (not shown) are similar to those for the 50% case, but with Radiance vs. Image Geometry plots showing increasing downward curvature as albedo increases.

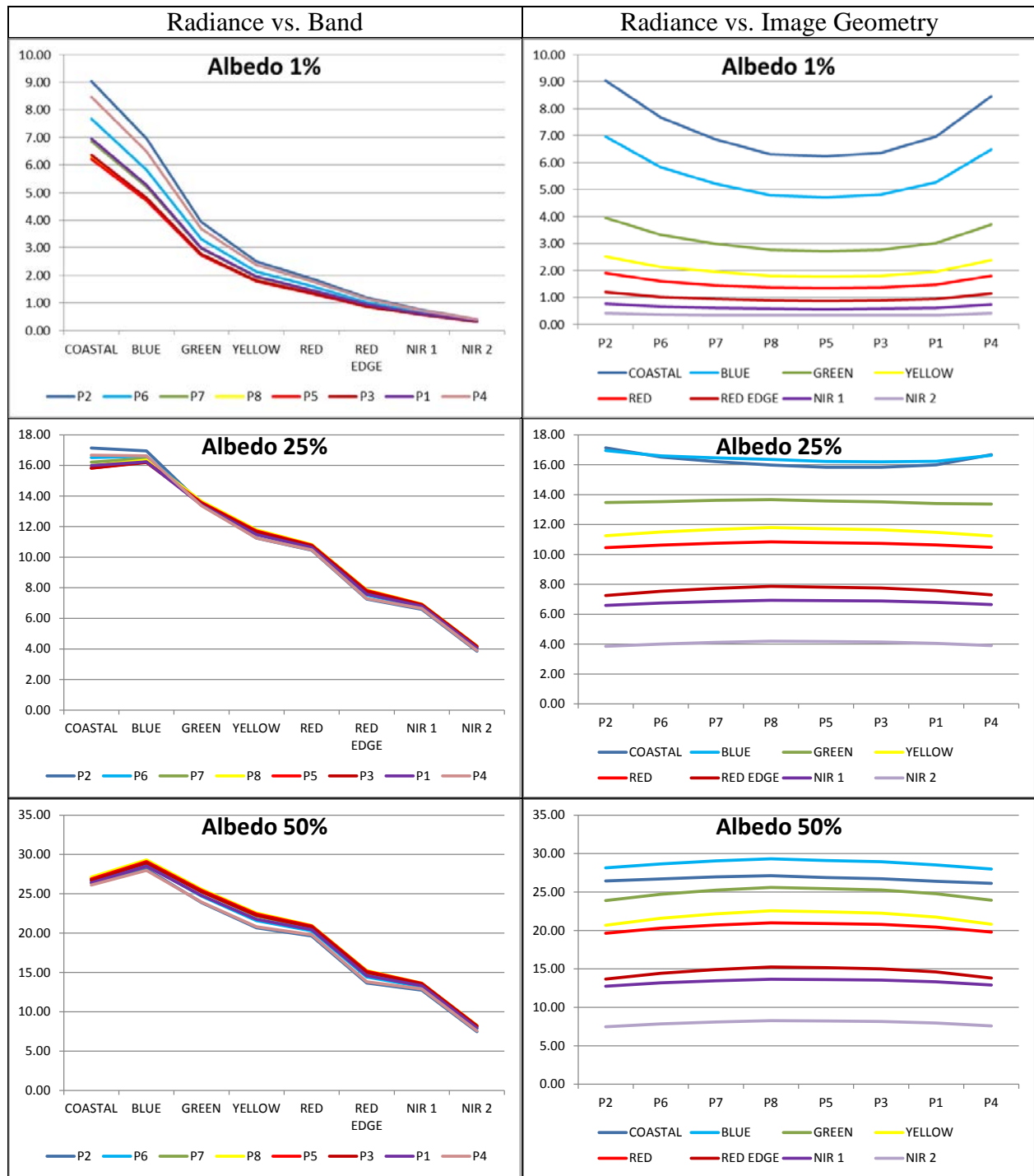


Figure 29. MODTRAN Radiance Plots, Albedo: 1%, 25%, 50%

Considering the Radiance vs. Band plots first, as albedo increases the overall radiance increases—an intuitive result. Additionally, the brightest bands are the shorter wavelengths as evidenced by the downward slope of the plot from left to right. The main

difference lies in the shorter wavelengths for each image, particularly for the darker albedos, in which the radiance is strongest for the images furthest away from nadir (P2 and P4). At some point between 25% and 50% albedo, band variation for the different image geometries approaches a constant value and the overall plot shapes remain the same as albedo increases.

Similar to the Radiance vs. Band plots, as albedo increases in the Radiance vs. Image Geometry plots the overall radiance increases, as well. In this case the primary difference is seen in the curvature of the lines for the different spectral bands. For the darkest albedo, an upward curvature is very evident, particularly in the shorter wavelengths. As albedo increases, curvature shifts downward beginning with the longer wavelengths (coastal and blue). By 50% albedo all band plots are downward in curvature and remain this way up to the maximum 100% albedo.

These plots show that the MODTRAN-modeled image pixel reflectance (albedo) has a discernible influence on the TOA radiance. In the Radiance vs. Band plots, it is apparent that the variation for the darker albedo data sets is greatest in the shorter wavelengths (coastal and blue). From II.B.3 (Atmospheric Scattering), this variation suggests an influence that could be attributable to Rayleigh scattering which is strongest in the shorter wavelengths. Additionally, atmospheric path length is greatest for the most off-nadir image geometries (P2 and P4) and should consequently result in larger scattering effects for these geometries over the closer-to-nadir geometries. This effect supports the Rayleigh scattering attribution since radiance values in the shorter wavelengths are greatest for image geometries P2 and P4 and decrease and then increase as geometry moves through that for P8. By extension, this reasoning also explains the upward curvature seen in the Radiance vs. Image Geometry plots for the darker albedos. As albedo brightness increases and the curvature shifts from upward to downward beginning with the longer wavelength bands, another phenomenon must be occurring; the next section will explore this further.

2. Path Scattered and Ground Reflected Radiance Plots

MODTRAN plots were generated showing the path scattering and ground reflected radiance terms calculated for P2 and P8 image geometries (Figures 30–34). P8 represents the most nadir image geometry and P2 represents one of the two most off-nadir image geometries. Directly from equation (2.27), MODTRAN computed values of path scattering and ground reflected radiance correspond to the terms L_p and L_T , respectively, and their sum is the total radiance, L_s , detected at the sensor.

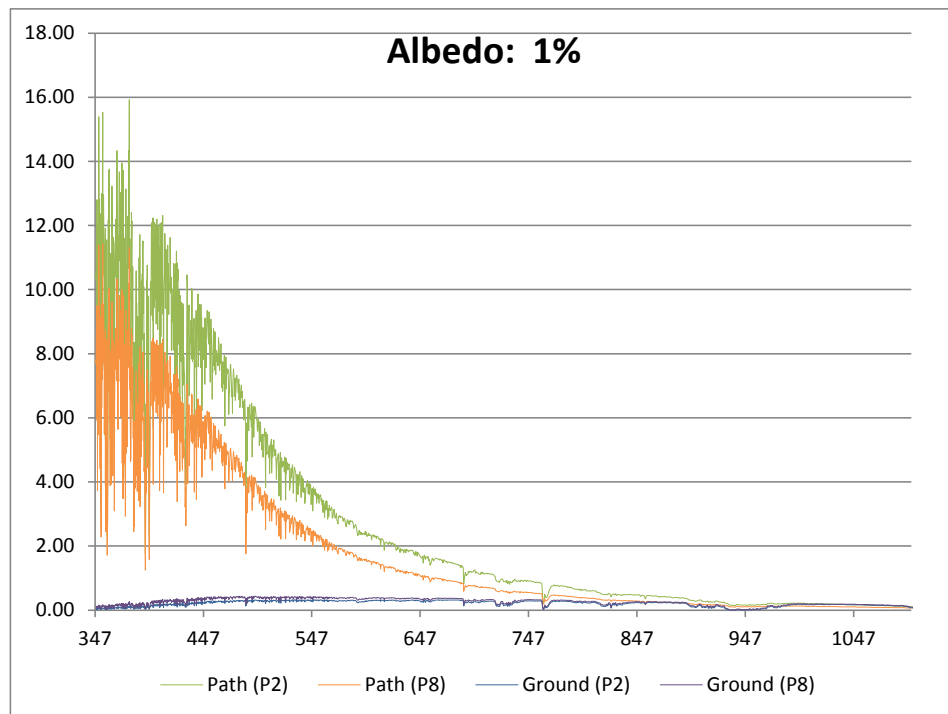


Figure 30. MODTRAN Path Scattered & Ground Reflected Radiance, 1% Albedo, P2 & P8 geometry

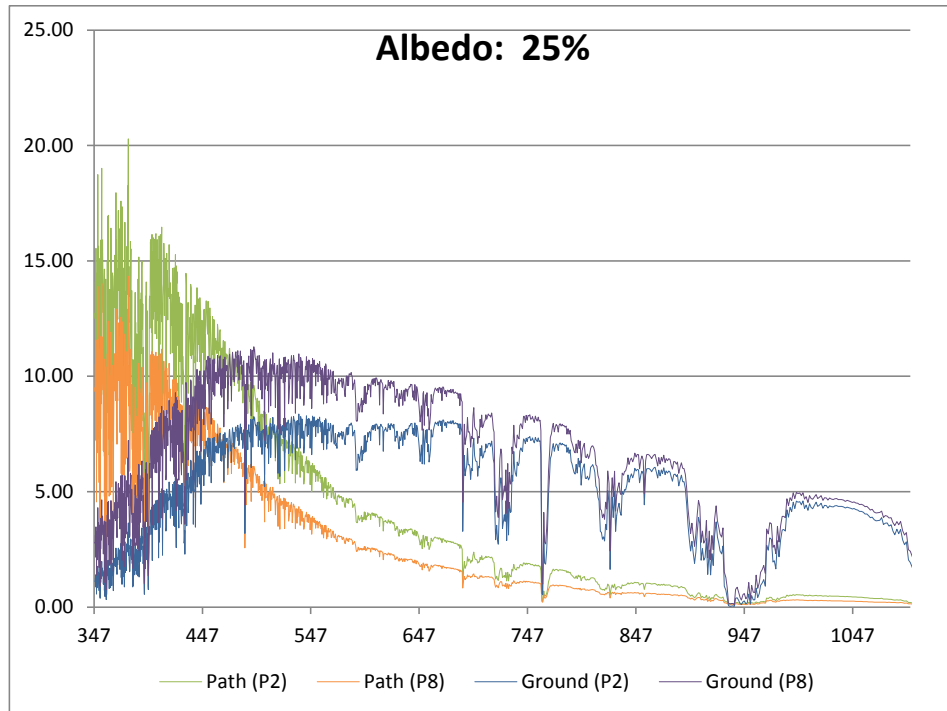


Figure 31. MODTRAN Path Scattered & Ground Reflected Radiance, 25% Albedo, P2 & P8 geometry

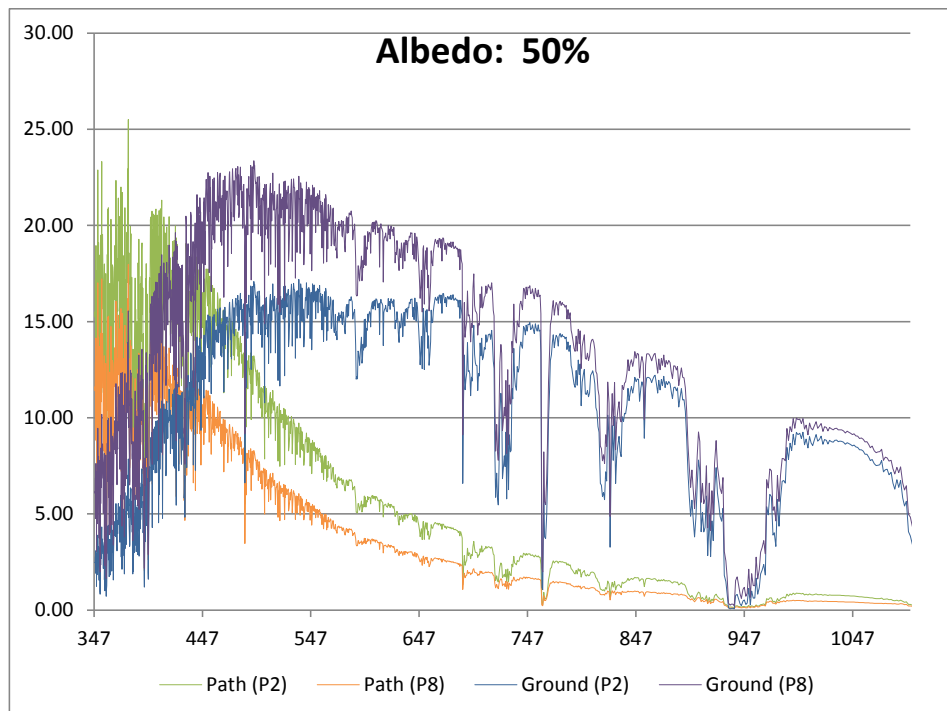


Figure 32. MODTRAN Path Scattered & Ground Reflected Radiance, 50% Albedo, P2 & P8 geometry

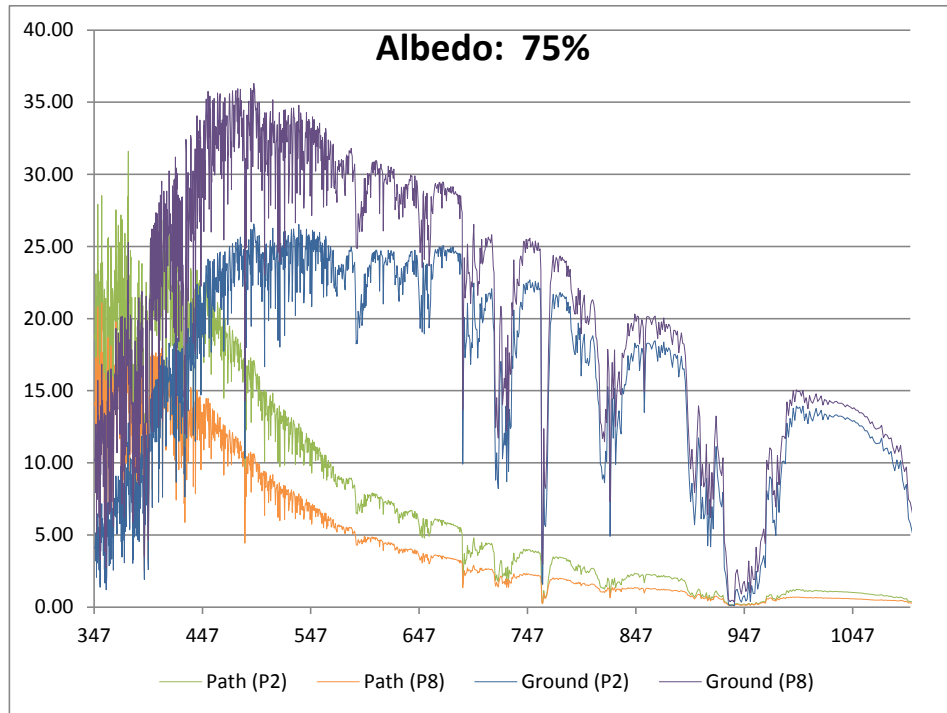


Figure 33. MODTRAN Path Scattered & Ground Reflected Radiance, 75% Albedo, P2 & P8 geometry

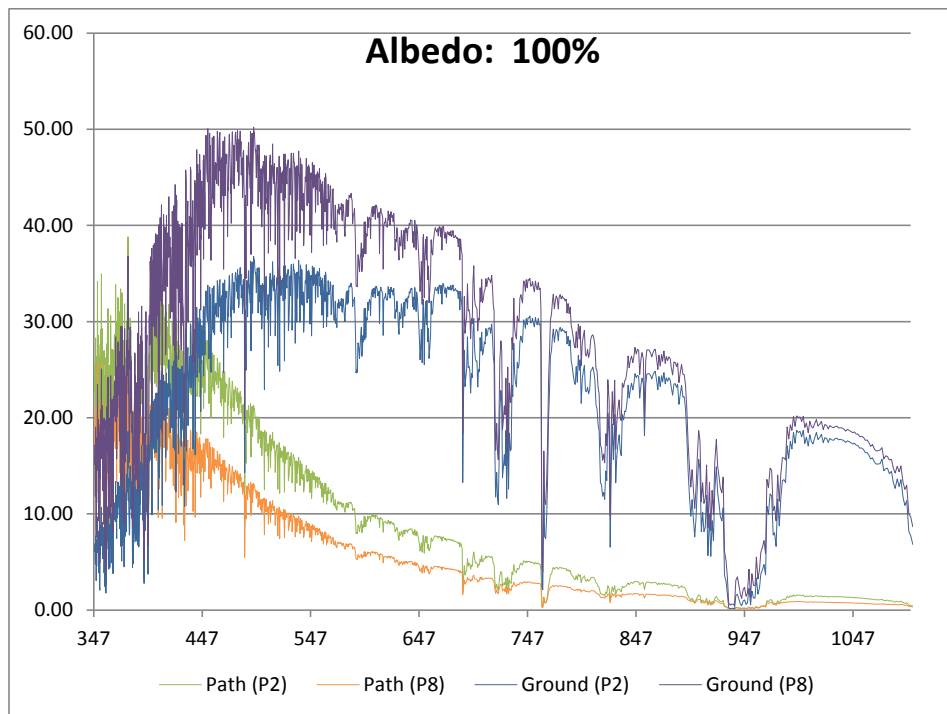


Figure 34. MODTRAN Path Scattered & Ground Reflected Radiance, 100% Albedo, P2 & P8 geometry

Starting with a surface albedo of 1%, path scattering radiance for both P2 and P8 dominates over ground reflected radiance which is almost negligible. As would be expected for the path scattering, P2 radiance is greater than P8 radiance due to the longer path through the atmosphere.

As albedo increases to 25%, the ground reflected radiance takes a dominant role over path scattered radiance, for increasing wavelength, in the 450–550 nm wavelength range. Examining the differences based on geometry, overall path scattered radiance is higher as off-nadir angle increases, and overall ground reflected radiance is higher as off-nadir angle decreases. Comparing the points on the plot where these two radiance values intersect for the respective geometries adds some additional insight. As seen in Figure 35, which is the 25% albedo plot zoomed-in to the 400–550 nm wavelength range, the crossover point between path scattered and ground reflected radiance for the P8 (nadir) geometry is to the left of that for P2 geometry. In terms of WV-2 spectral bands, the most nadir case geometry experiences a crossover within the coastal band; as off-nadir angle increases, the crossover occurs at the high end of the blue band.

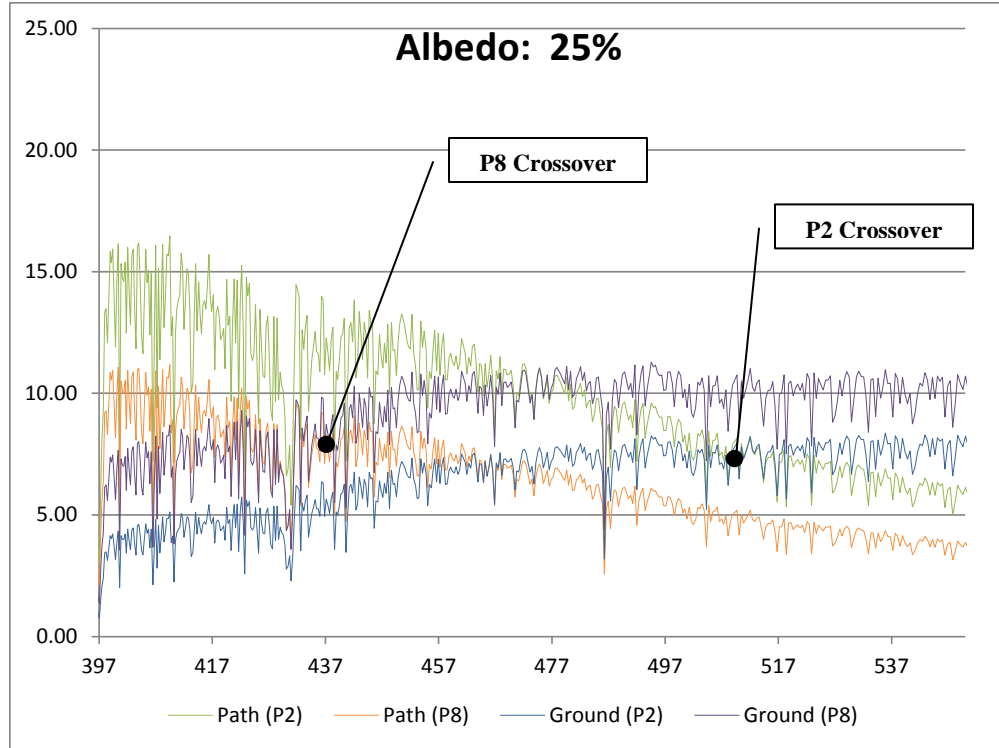


Figure 35. Zoomed-in Path Scattered & Ground Reflected Radiance, 25% Albedo, P2 & P8 geometry

For the other albedo cases (50%, 75% and 100%), behavior is similar to the 25% albedo case. As would be expected, overall radiance values increase with increasing albedo. The crossover points, however, shift to the left (decreasing wavelength) as surface albedo increases.

The phenomena seen in the previous section's plots can now be explained. As surface albedo increases, the position of the crossover points shifts to the left (decreasing wavelength) and the distance between them decreases, as well. Over all bands of the WV-2 sensor, TOA radiance is, therefore, dominated by path scattered radiance when surface albedo is low (dark) and by ground reflected radiance when albedo is high (bright). Because the crossover point separation directly corresponds to image geometry, the greater variation in radiance as wavelength decreases among the plotted series of the Radiance vs. Band plots of Figure 29 is a direct result of the corresponding changes in path scattered radiance as surface albedo and wavelength decrease. Similarly, the crossover point separation also explains the decreasing upward curvature seen in the

Radiance vs. Image Geometry plots. This is due to the decreasing dominance of path scattered radiance to the total radiance as albedo increases.

Turning attention to the right of the crossover points, for increasing albedo and increasing wavelength, ground reflected radiance is dominant. The downward curved lines of the higher wavelength bands in the Radiance vs. Image Geometry plots of Table 5 are, therefore, representative of ground reflected radiance only. This indicates that ground reflected radiance is greatest for the most nadir image geometry and decreases as off-nadir angle increases, suggesting a variation in surface reflectance that is solely due to the viewing geometry. Because the slight decrease in radiance is relatively uniform on either side of the curve's high point (representing P8 geometry), this is consistent with a Lambertian surface.

B. COMPARISON OF WV-2 IMAGERY TO MODTRAN MODELS, BY BAND

The analysis in section IV.A provides valuable insight when applied to the WV-2 imagery. A surface reflectance spectral library is essentially a series of albedo values associated with a corresponding wavelength range. In choosing the surfaces to investigate, it was important to select those with albedos that were dark, bright and a combination of the two. The surfaces chosen were ASPHALT, SAND and GRASS.

1. Asphalt

Albedo values for the asphalt surface are generally dark across the entire WV-2 wavelength range (Figure 36). As a result, the plots contained in Figures 37 and 38 look very similar to the dark (1%) albedo plots of section IV.1.A.

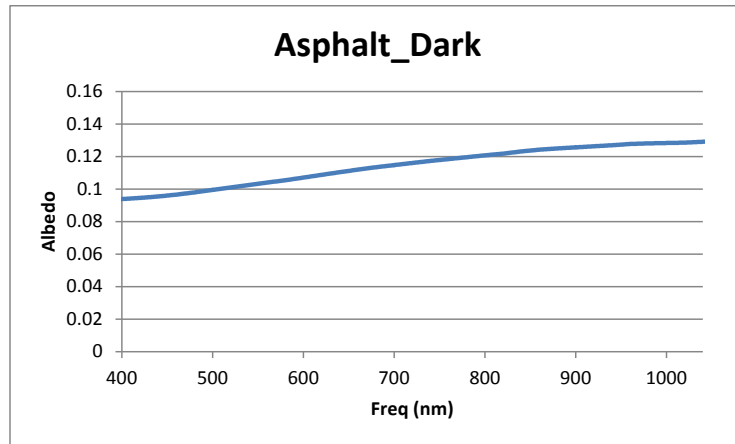


Figure 36. ASPHALT_DARK Spectral Reflectance Plot (After DLR using data included with MODO)

a. Analysis–Radiance vs. Band

Both of the plots in Figure 37 show downward trending plotlines that converge from left to right, an expected result for darker albedo values. Overall radiance values derived from the imagery are lower than those for the MODTRAN-calculated values indicating that the actual image pixel chosen was darker than the Asphalt_dark spectral library. Because of the slight differences in overall radiance values, the Imagery-Asphalt plot looks more like the 1% albedo plot of Figure 29 and the MODTRAN-Asphalt plot begins to show an appearance trend between the 1% and 25% albedo plots of Figure 29. Each of these results is consistent and indicates that the modeled data is in agreement with the WV-2 imagery data for a dark surface.

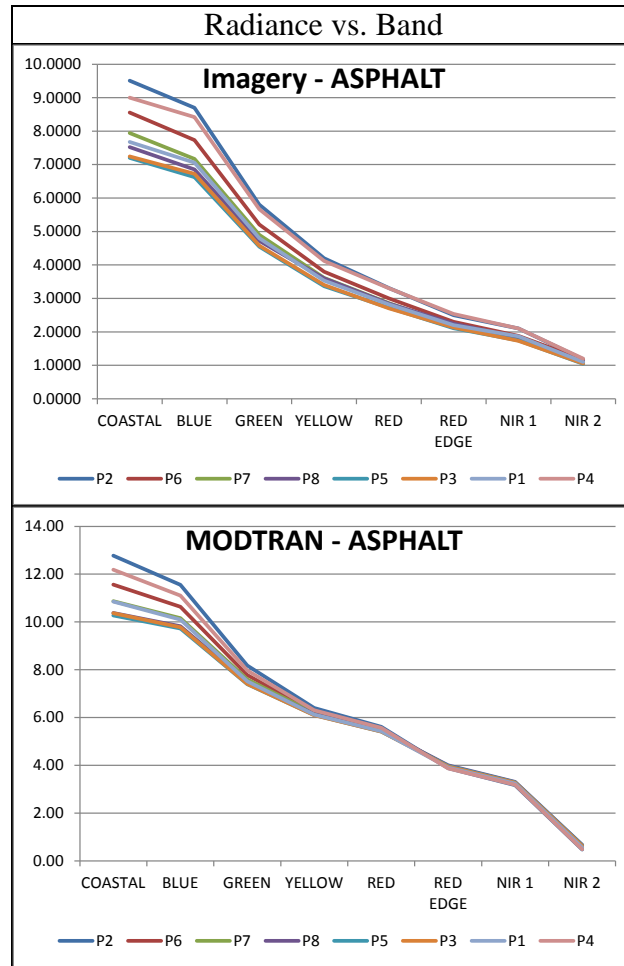


Figure 37. ASPHALT – Radiance vs. Band

b. Analysis–Radiance vs. Image Geometry

The plots in Figure 38 are in almost full agreement. The differences in overall radiance values between the two plots are minor and the cause is the same as that provided in the analysis above. The shift from upwardly-curved lines in the coastal and blue bands to almost horizontal lines in the NIR bands indicates path scattered radiance is the dominant form of radiance for this data. In the Imagery-Asphalt plot of Figure 38, there does appear a slight radiance increase for image geometry P8 (most nadir) in the higher wavelength bands. This is a clear indication of non-Lambertian surface reflectance properties of the asphalt surface in the imagery that could be attributed to unique BRDF effects of the asphalt ROI.

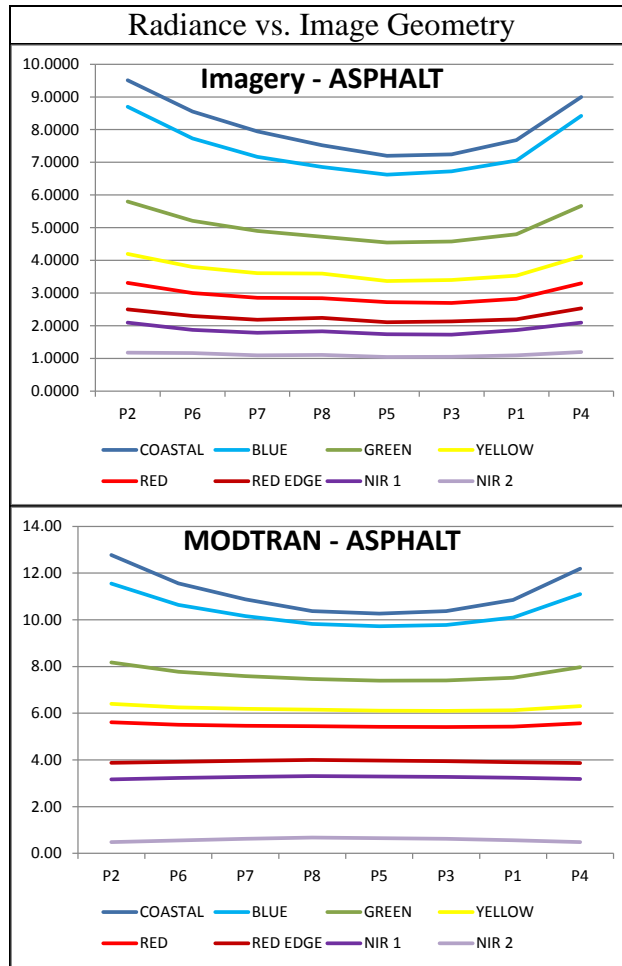


Figure 38. ASPHALT–Radiance vs. Image Geometry

2. Sand

Compared with the asphalt surface, the sand surface is generally bright across the entire WV-2 wavelength range (Figure 39). Both plots appear very similar in both shape and overall radiance values indicating that the chosen SAND spectral library used in the MODTRAN calculations was an accurate representation of the sand ROI chosen in the imagery.

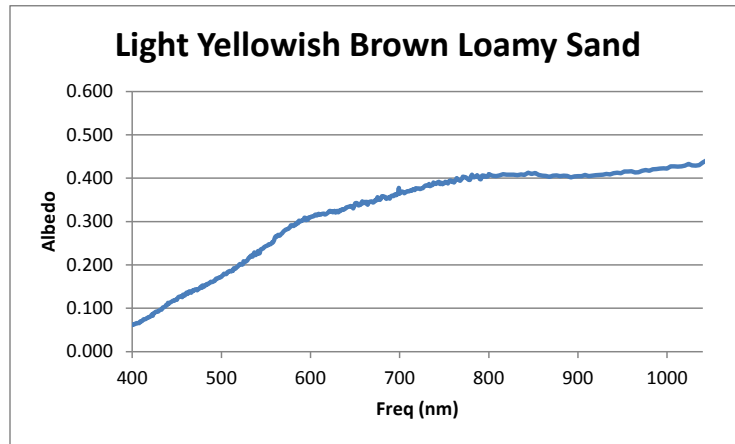


Figure 39. LIGHT YELLOWISH BROWN LOAMY SAND Spectral Reflectance Plot (After Baldrige et al., 2009, using data downloaded from <http://speclib.jpl.nasa.gov/>)

a. Analysis–Radiance vs. Band

In the plots of Figure 40, the highest radiance values occur in the yellow band which makes sense as the sand is visually yellowish in color. The closest agreement in both plots with respect to the different geometry lines is among the radiance values for the coastal, blue and NIR bands. For the lower wavelengths, the slight variation in radiance values among the geometry lines is due to the dark albedo and corresponding dominance of path scattered radiance in this wavelength region (Figure 39). As the albedo increases, it would be expected that the lines would converge and remain so as shown in the MODTRAN-SAND plot. It is interesting to note that this is not the case in the Imagery-SAND plot: there is a much broader variation in radiance up to the NIR1 band, with the highest radiance consistently occurring for the P8 (most nadir) geometry. To explain this behavior requires further analysis of the Radiance vs. Image Geometry plots.

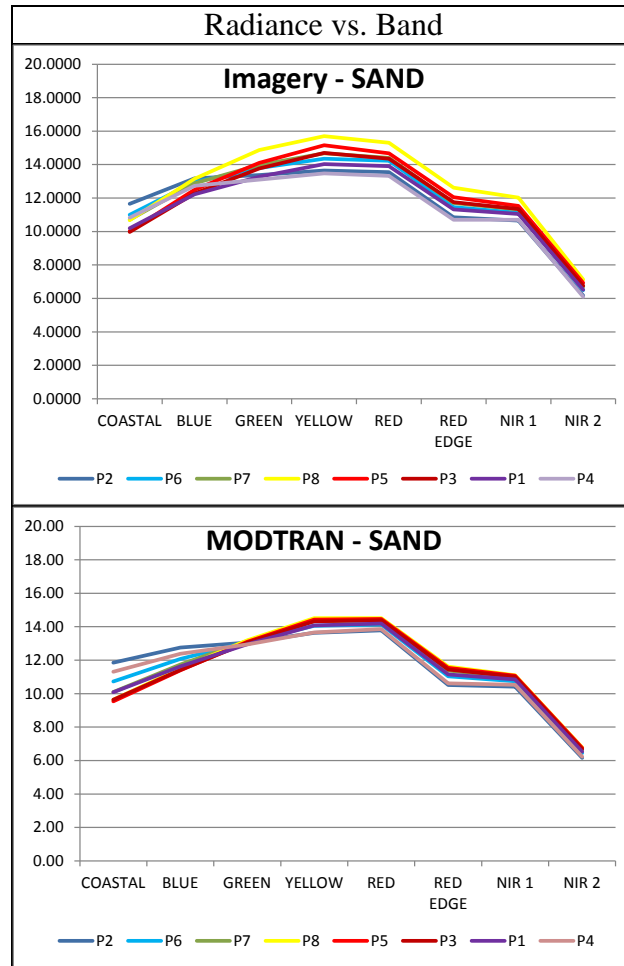


Figure 40. SAND–Radiance vs. Band

b. Analysis–Radiance vs. Image Geometry

The most obvious difference between the plots of Figure 41 is that the smooth lines of the MODTRAN-SAND plot are not the same in the Imagery-SAND plot. Not surprisingly, because of the darker albedo values in the shorter wavelengths (Figure 39), path scattered radiance is dominant in the coastal and blue bands and manifests in the plots as the two upward-shaped coastal and blue curves. The brighter albedo values in the higher wavelengths result in the downward-shaped curves for all other bands and indicate the dominance of ground reflected radiance. Similar to the discussion for the Asphalt analysis, the lack of smoothness evident in the Imagery-SAND plot could be a clear indication of non-Lambertian reflectance properties of the real surface studied in the imagery. Additionally, because this surface is much brighter than asphalt, these

differences are more apparent. This, in turn, could explain the variation in radiance values seen for the different geometry lines of the GREEN to RED EDGE bands in the Imagery-SAND plot of Figure 40.

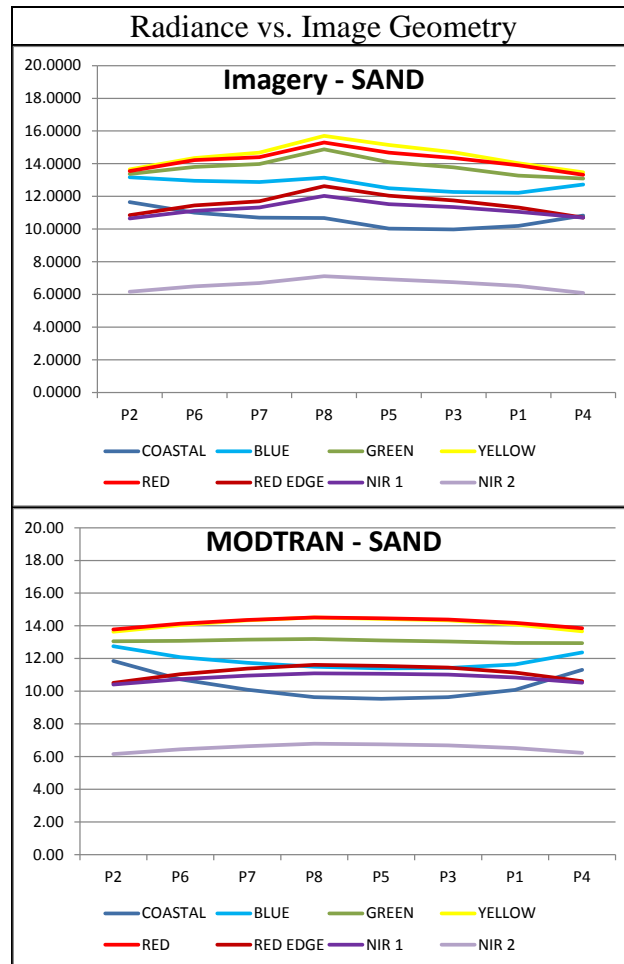


Figure 41. SAND – Radiance vs. Image Geometry

3. GRASS

As expected for green vegetation, the albedo values for GRASS are generally dark up until the IR ledge (~700 nm), at which point they increase quickly to brighter values (Figure 42). Over the wavelength range of the WV-2 satellite, this surface spectral library provides a nice split between dark and bright albedo values. Analysis will first consider the darker region (400–700 nm) and then the brighter region (700–1100 nm).

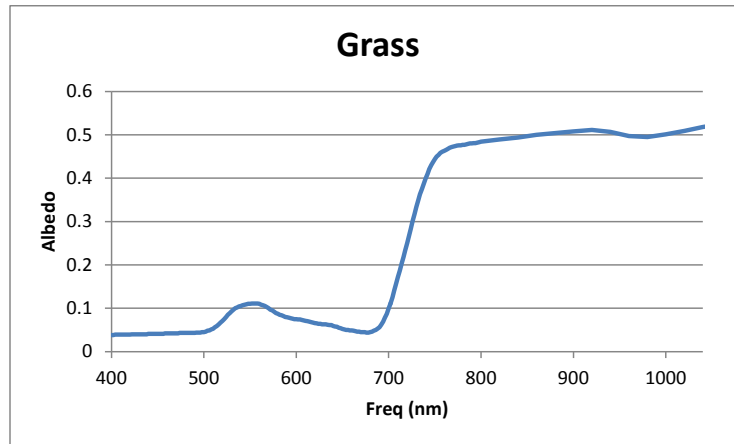


Figure 42. GRASS Spectral Reflectance Plot (After Baldrige et al., 2009, using data included with ENVI)

a. Analysis–Radiance vs. Band

For the COASTAL to RED bands of the Radiance vs. Band plots in Figure 43, the corresponding albedo values of Figure 42 are generally dark except for a slight increase in the green band. Because of this, the COASTAL to RED plotlines of Figure 43 are consistent with the dark albedo plots of Figure 29 (downward trending and converging left to right) with only a slight radiance increase in the GREEN band due to the brighter albedo in the green wavelengths. The higher radiance values of the most off-nadir geometry lines (P4 and P2) over the most nadir geometry lines (P8), most evident in the COASTAL band, is clear indication of the dominance of path scattered radiance in this region.

Between the RED and NIR2 bands, the corresponding albedo values of Figure 42 are much brighter with respect to the lower wavelength range. Consequently, the plotlines of Figure 43 are much closer together than in the COASTAL to RED region and there is shift, with the most-nadir geometry now having the higher radiance value. This indicates that ground reflected radiance has now become dominant in this region.

The similarity between both plots indicates satisfactory agreement between the actual imagery results and the MODTRAN-modeled results.

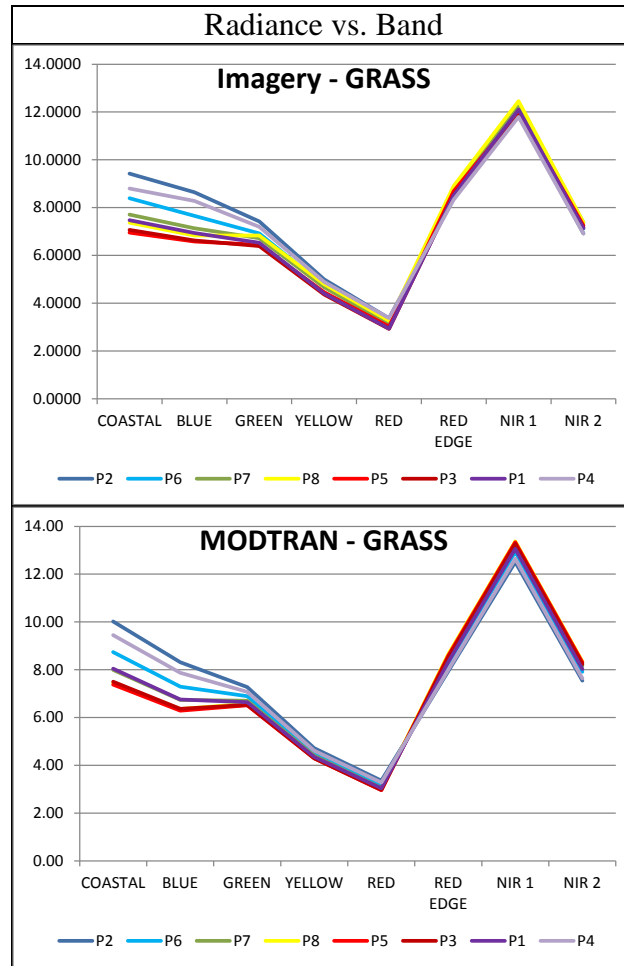


Figure 43. GRASS – Radiance vs. Band

b. Analysis–Radiance vs. Image Geometry

The Radiance vs. Image Geometry plots of Figure 44 provide an opportunity for analysis that combines elements seen in the analyses for both ASPHALT and SAND (dark and bright albedo values). Specifically, the COASTAL to RED band lines exhibit downward curvature (dominance of path scattered radiance) and the RED EDGE to NIR2 bands exhibit upward curvature (dominance of ground reflected radiance). Additionally, in the Imagery-GRASS plot, the RED EDGE to NIR2 plot lines are not as smooth as those in the MODTRAN-GRASS plot, suggesting that the actual surface in the imagery is non-Lambertian.

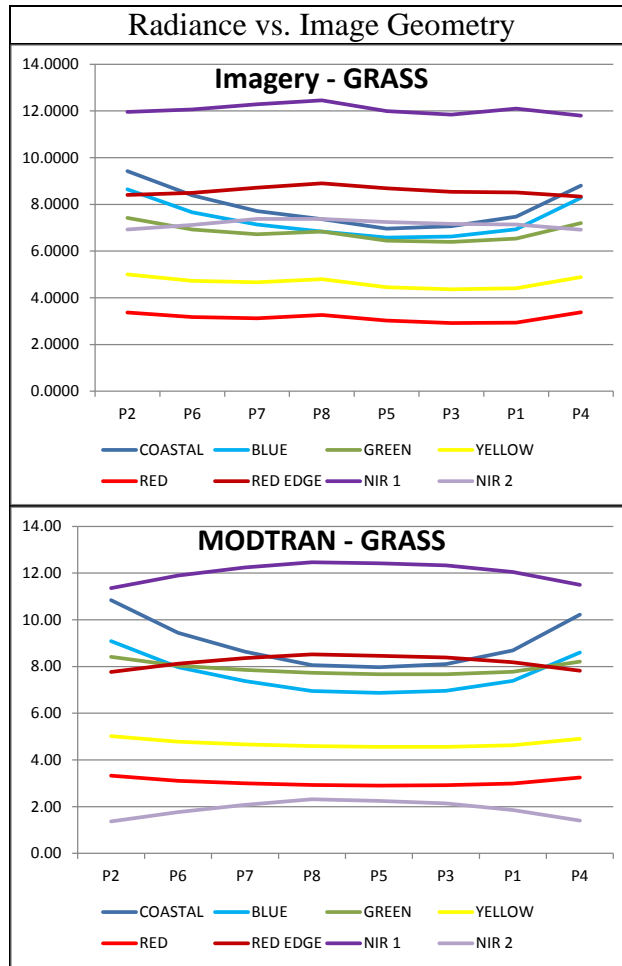


Figure 44. GRASS – Radiance vs. Image Geometry

V. CONCLUSIONS

A. SUMMARY OF ANALYSIS AND RESULTS

Eight multi-angle, multispectral WorldView-2 images of Rio de Janeiro were processed to TOA radiance using sensor and acquisition information. Three regions of interest were chosen within the imagery set, corresponding to both dark and bright targets, and a combination of the two. Additionally, MODTRAN models were developed using image parameters, to include geometry for both sun and sensor positions, atmospheric parameters and surface reflectance spectral libraries similar to the regions of interest chosen from the imagery.

Analysis was conducted in three steps. The first step, using only the MODTRAN models, resulted in plots of TOA radiance for each image geometry and were grouped according to surface reflectance values ranging from dark (1% albedo) to bright (100% albedo). These plots established a baseline for further analysis and comparison. The second step, again using only MODTRAN models, developed plots that demonstrated the differences between atmospherically-dominated and ground reflectance-dominated contributions to TOA total radiance. The final step compared TOA radiance plots from the WV-2 imagery to similarly modeled MODTRAN data.

B. CONCLUSIONS

The ability to model WV-2 radiance using MODTRAN provides useful insight into reflectance phenomena, particularly from a remote sensing perspective. Specifically, MODTRAN provides the ability to model surface reflectance in a variety of ways that give the user the ability to consider different approaches when relating models to WV-2 imagery. In this thesis, both the MODTRAN albedo and radiance models, generated for the different image geometries, provided these approaches. The albedo models served as a basis for comparison with the WV-2 imagery data, and the radiance models provided a means to explain the phenomena present in both the imagery and model data. Each of these efforts provided both (1) a validation that MODTRAN models could be generated that accurately represent multi-angle, multispectral WorldView-2 imagery, and (2) the

phenomena seen in both the modeled and empirical results could be explained using MODTRAN-generated data, to include discernment of BRDF effects in WorldView-2 imagery data.

The multi-angle, multispectral features of the WV-2 satellite, coupled with the modeling capabilities of MODTRAN, resulted in the observation and understanding of three distinct phenomena. First, the enhanced resolution of the WV-2 satellite provided the means to distinguish surfaces with a granularity necessary to ensure consistent observation of spectral properties. This was demonstrated by the effective analysis of the three different surfaces chosen as the ROI's in the WV-2 imagery. Second, WV-2's multi-angle capabilities allowed measurements of radiance over a range of angular values. These measurements, in concert with the MODTRAN models, provided a clear indication of the influence that atmospheric path length and surface reflectance have on TOA radiance. Within the MODTRAN-modeled radiance analysis, this influence was clearly evident as the plotlines for path scattered radiance were noticeably higher in the off-nadir geometries and ground reflected radiance was higher in the nadir geometries. This behavior was further confirmed in the comparison analysis by the shapes of the plotlines: upward curvature demonstrated higher path scattering radiance for the off-nadir geometries, flat to moderately downward curvature demonstrated higher ground reflected radiance. Third, and finally, the wavelength of the sensed light, characterized by the WV-2 band of detection, exhibited clear influences by atmospheric scattering and view/illumination geometry. In all of the Radiance vs. Band plots for dark surfaces (<25% albedo), the variation in radiance values was most evident in the COASTAL and BLUE WV-2 bands, a behavior consistent with Rayleigh scattering. For the MODTRAN-modeled plots, as surface brightness increased (>25% albedo), the plotlines converged and remained relatively close together into the higher WV-2 wavelength bands, an expected behavior as ground reflected radiance is dominant in this region. Of particular note, however, were the noticeable differences between the imagery and MODTRAN-modeled plots of Radiance vs. Image Geometry for brighter albedo. Because MODTRAN models surface reflectance as Lambertian, the resultant plotlines are relatively flat and smooth; the imagery plotlines, however, are not. This provided

clear evidence that the ROI's selected from the WV-2 imagery, representing real surface reflectance properties, are not Lambertian and, consequently, the reflectance properties exhibited are due to the unique BRDF's of the surfaces analyzed.

C. FUTURE WORK POSSIBILITIES

1. MODTRAN Modeling using BRDF Algorithms

A relatively new feature of MODTRAN allows surface reflectance to be modeled using several kernel-driven BRDF algorithms. Use of these algorithms could provide models which more accurately represent multi-angle surface properties and, when compared to actual imagery data, could further confirm the utility of using a remote sensing platform in the study of BRDF effects.

2. MODTRAN Modeling of Hyperspectral Data

The ability afforded the MODTRAN user of creating unique satellite sensor response filter files offers great flexibility for further analysis. The modeling of a hyperspectral satellite sensor, and subsequent comparison to actual data, could provide much greater fidelity over that of a multispectral sensor.

3. Further Investigation of MODTRAN-modeled Radiance Elements

In addition to the MODTRAN-calculated path scattered and ground reflected radiance terms used in this thesis, MODTRAN calculates several other radiance terms, to include terms for thermal emission. A deeper investigation into the relationships among these different radiance values could provide valuable scientific insight and real-world utility.

4. Investigate WorldView-2 BRDF Phenomena using NEFDS Applications

The Nonconventional Exploitation Factors Data System (NEFDS) is a data and application software suite managed by the National Geospatial-Intelligence Agency (NGA). NEFDS provides quality reflectance data, to include BRDF, and other spectral measurements designed specifically for remote sensing applications. An investigation

and analysis of multi-angle WorldView-2 reflectance results with NEFDS measurements could provide useful validation and scientific insight regarding spectral signatures and materials detection.

APPENDIX

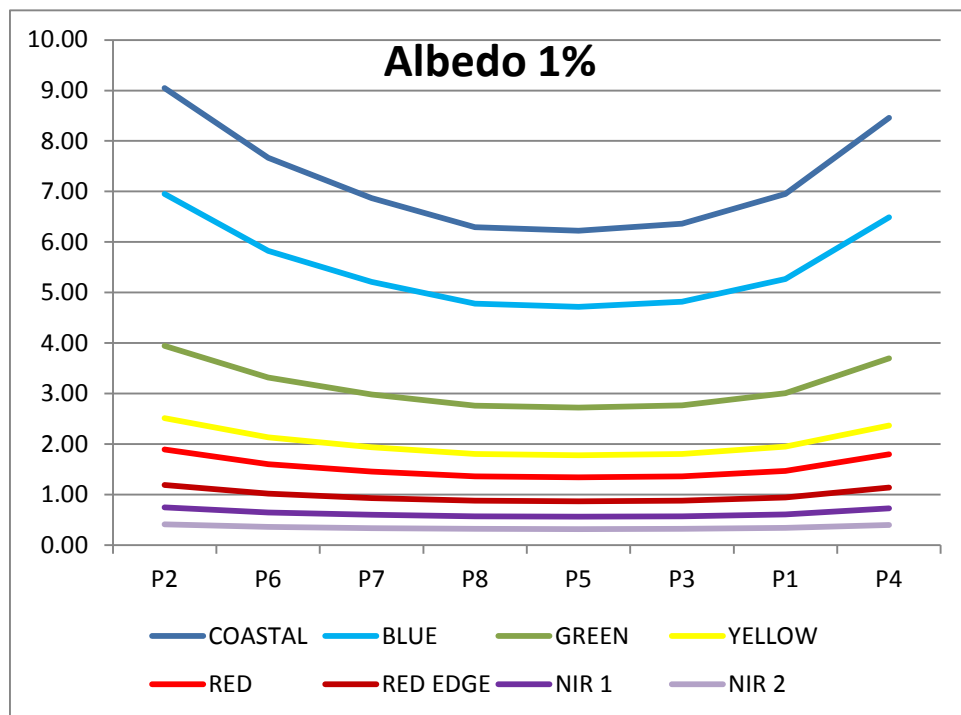
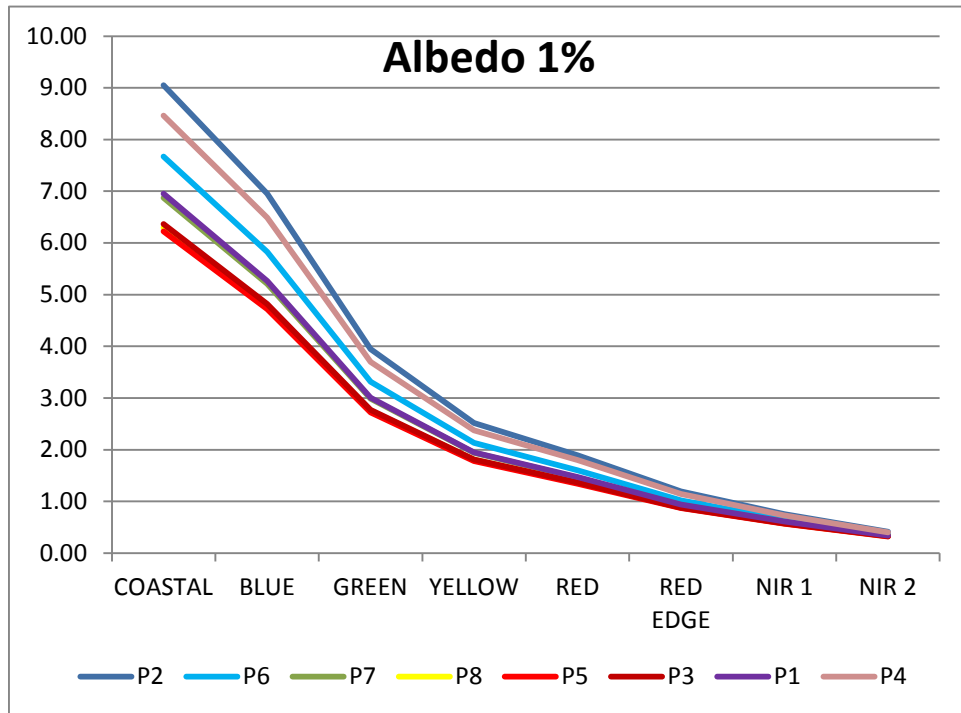
A. ENVI STATISTICS FILE

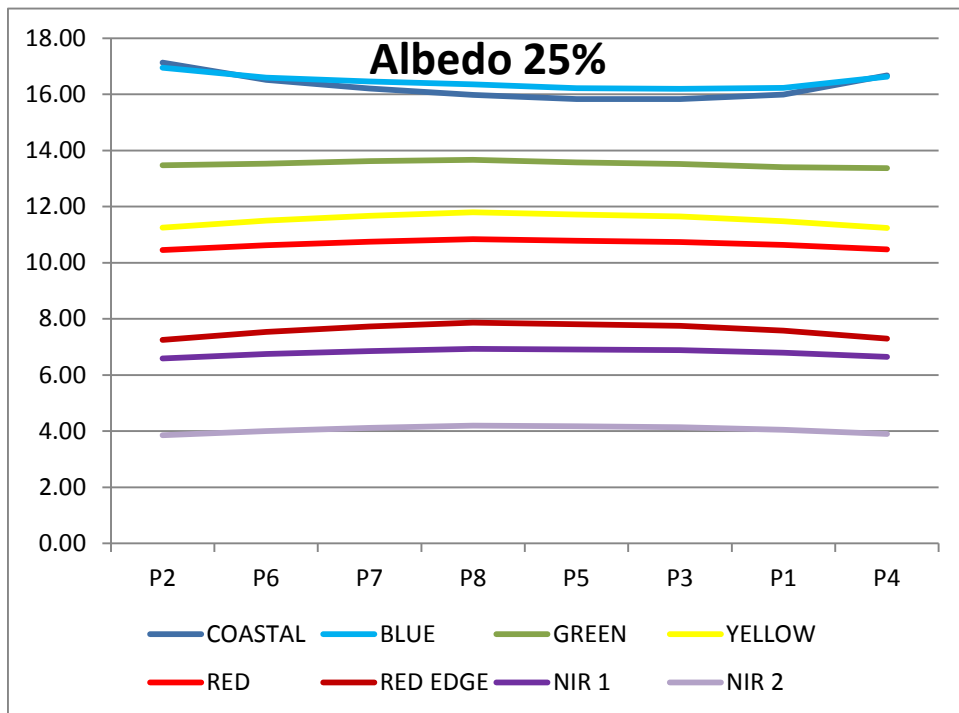
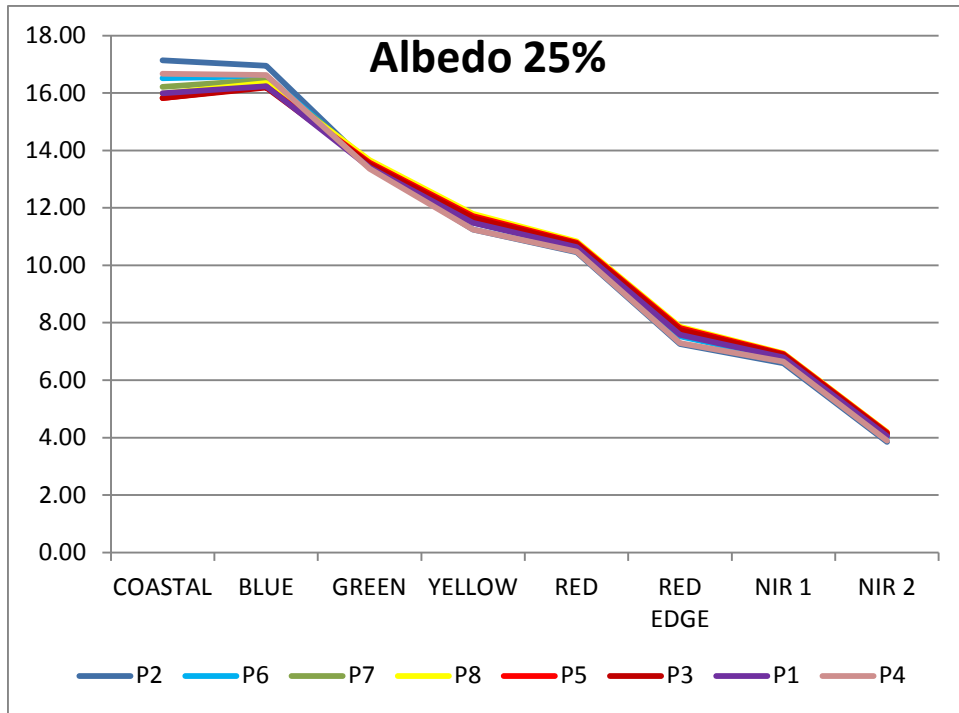
ROI: Asphalt (RW) [Blue] 9 points

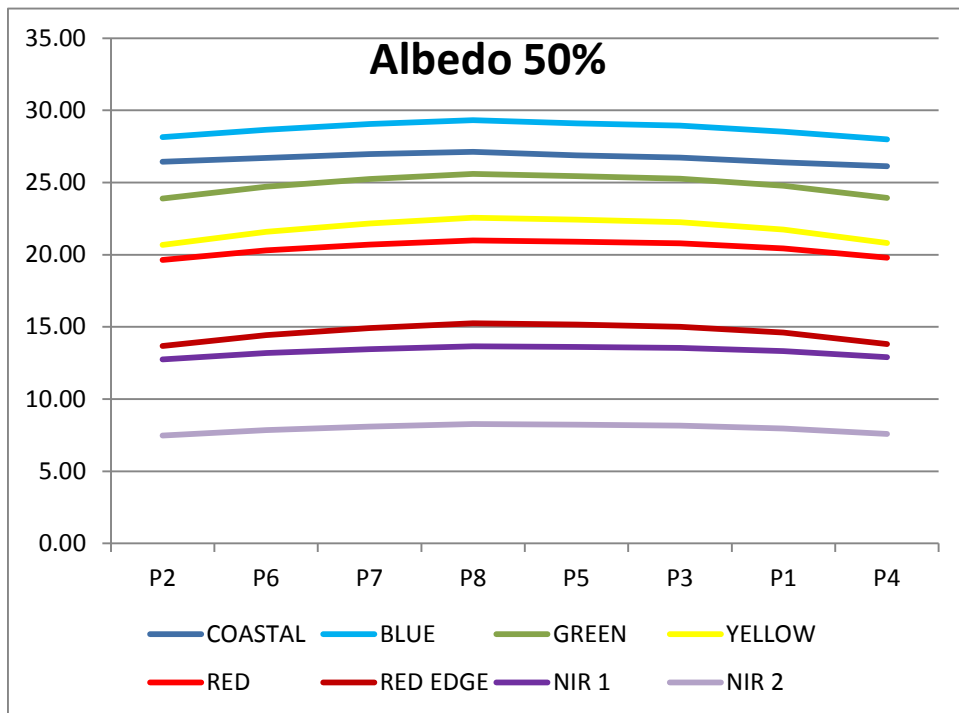
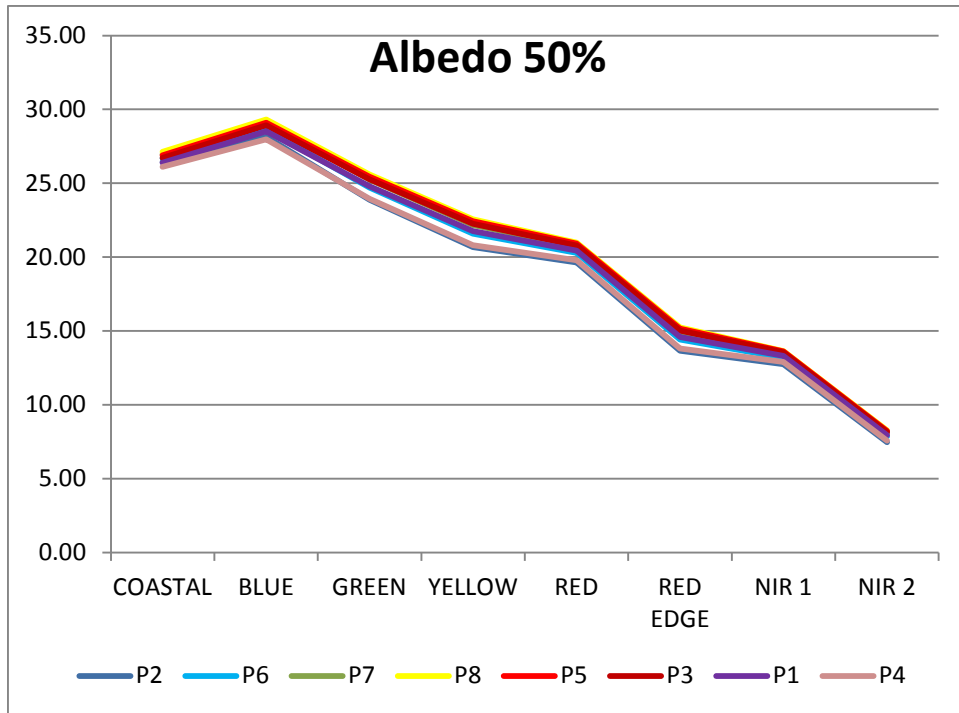
Basic Stats	Min	Max	Mean	Stdev
Band 1	76	77	76.777778	0.440959
Band 2	70	71	70.555556	0.527046
Band 3	48	48	48.000000	0.000000
Band 4	35	36	35.333333	0.500000
Band 5	28	29	28.222222	0.440959
Band 6	21	23	22.000000	0.500000
Band 7	18	20	18.666667	0.707107
Band 8	11	11	11.000000	0.000000

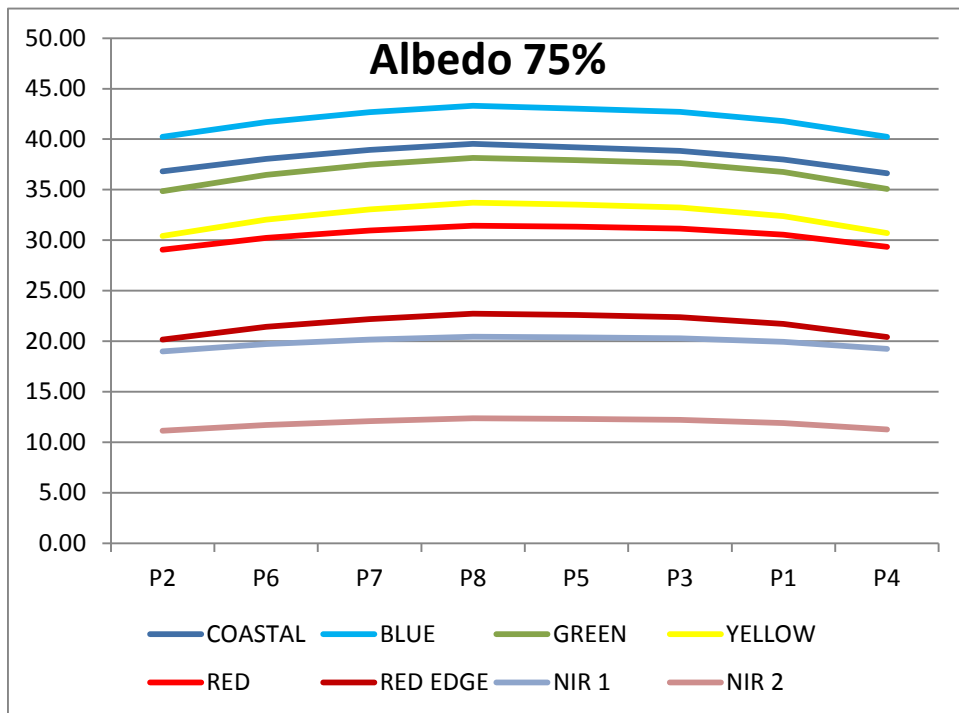
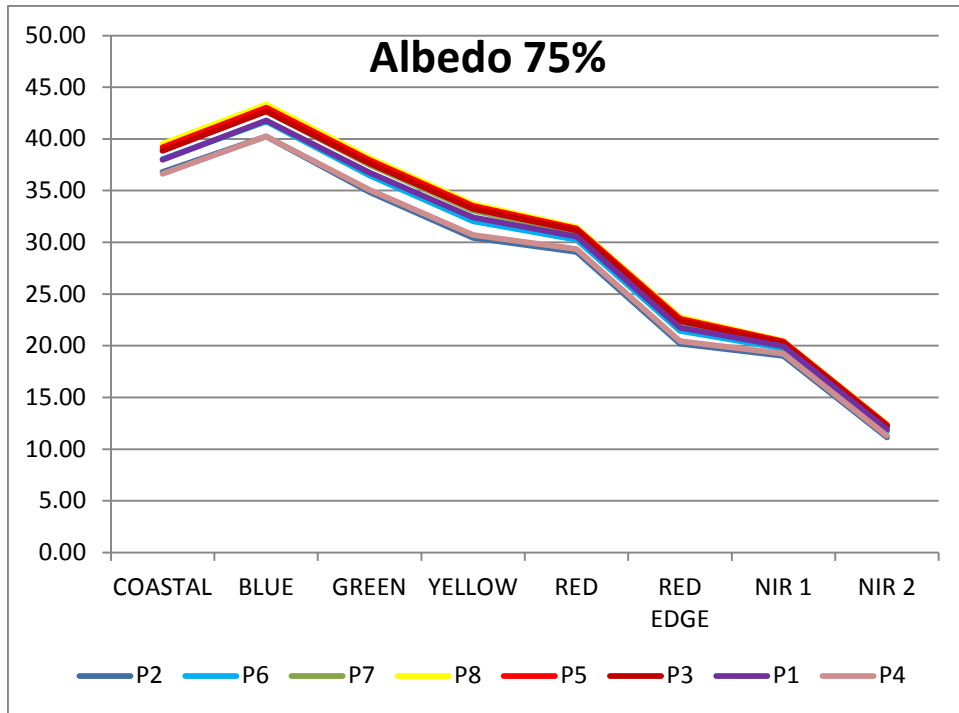
Histogram	DN	Npts	Total	Percent	Acc Pct
Band 1	76	2	2	22.2222	22.2222
	77	7	9	77.7778	100.0000
Histogram	DN	Npts	Total	Percent	Acc Pct
Band 2	70	4	4	44.4444	44.4444
	71	5	9	55.5556	100.0000
Histogram	DN	Npts	Total	Percent	Acc Pct
Band 3	48	9	9	100.0000	100.0000
Histogram	DN	Npts	Total	Percent	Acc Pct
Band 4	35	6	6	66.6667	66.6667
	36	3	9	33.3333	100.0000
Histogram	DN	Npts	Total	Percent	Acc Pct
Band 5	28	7	7	77.7778	77.7778
	29	2	9	22.2222	100.0000
Histogram	DN	Npts	Total	Percent	Acc Pct
Band 6	21	1	1	11.1111	11.1111
	22	7	8	77.7778	88.8889
	23	1	9	11.1111	100.0000
Histogram	DN	Npts	Total	Percent	Acc Pct
Band 7	18	4	4	44.4444	44.4444
	19	4	8	44.4444	88.8889
	20	1	9	11.1111	100.0000
Histogram	DN	Npts	Total	Percent	Acc Pct
Band 8	11	9	9	100.0000	100.0000

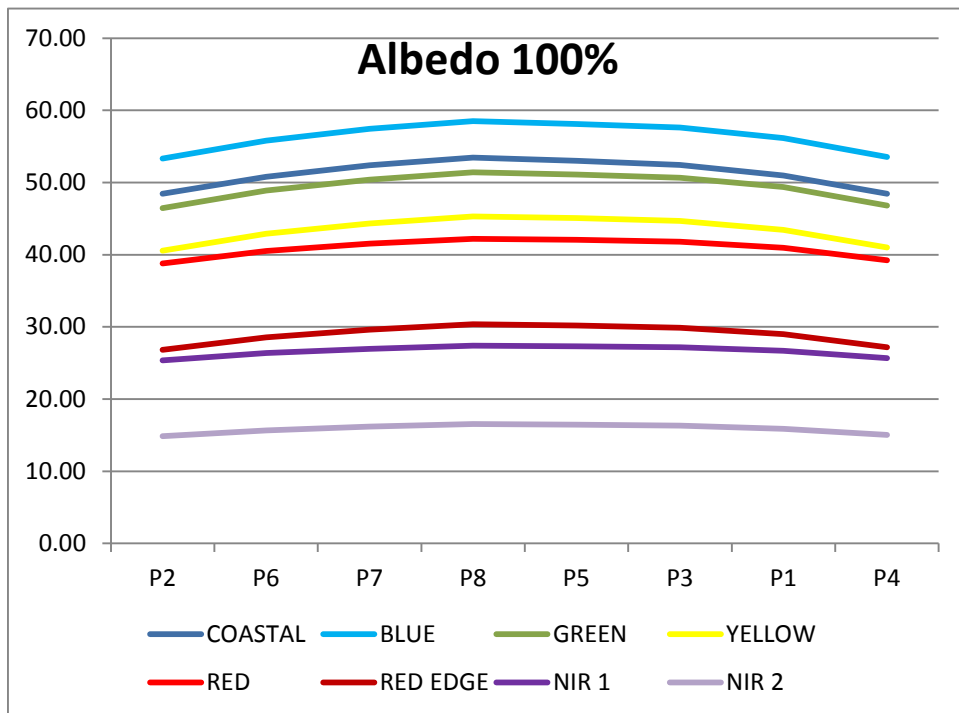
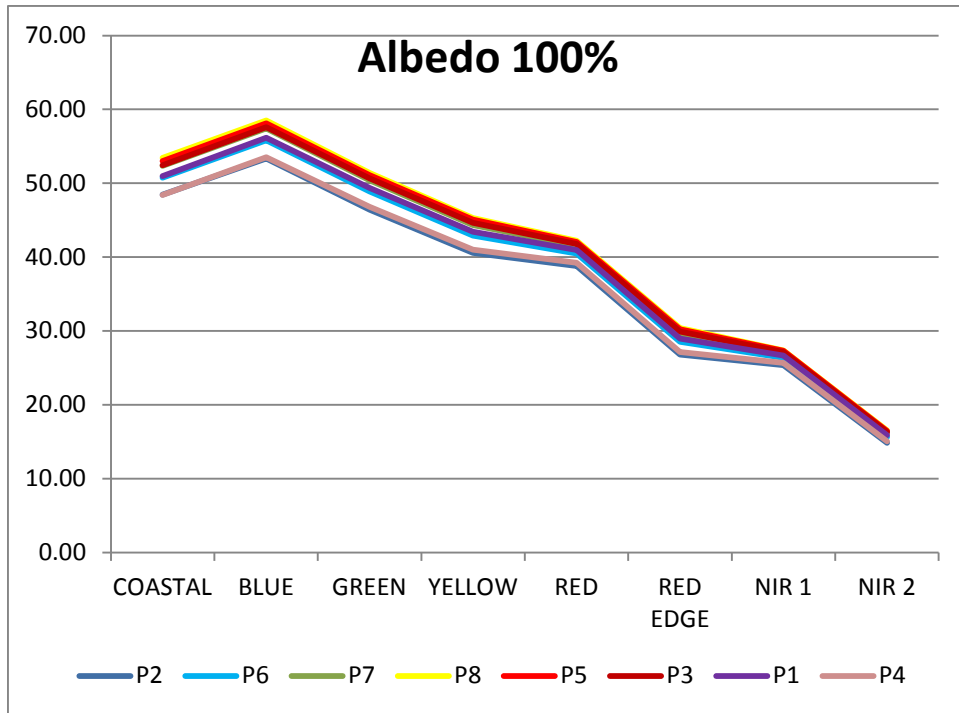
B. MODTRAN RADIANCE PLOTS: RADIANCE VS. BAND AND RADIANCE VS. IMAGE GEOMETRY FOR VARYING ALBEDO





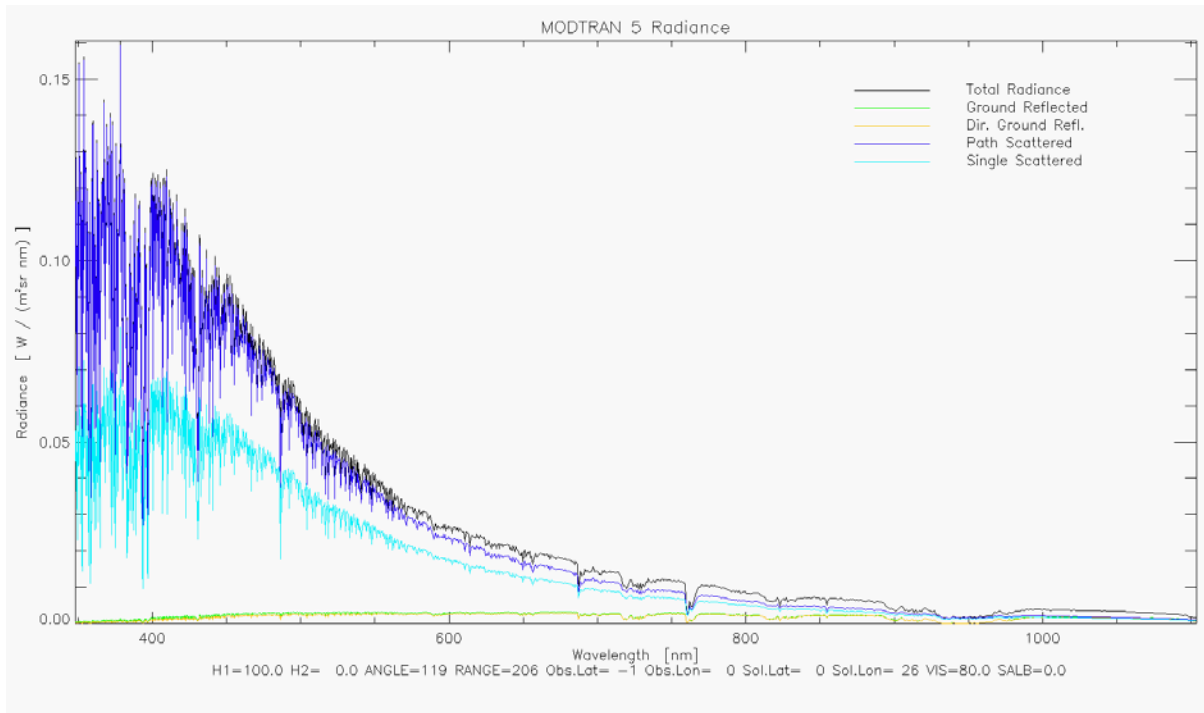




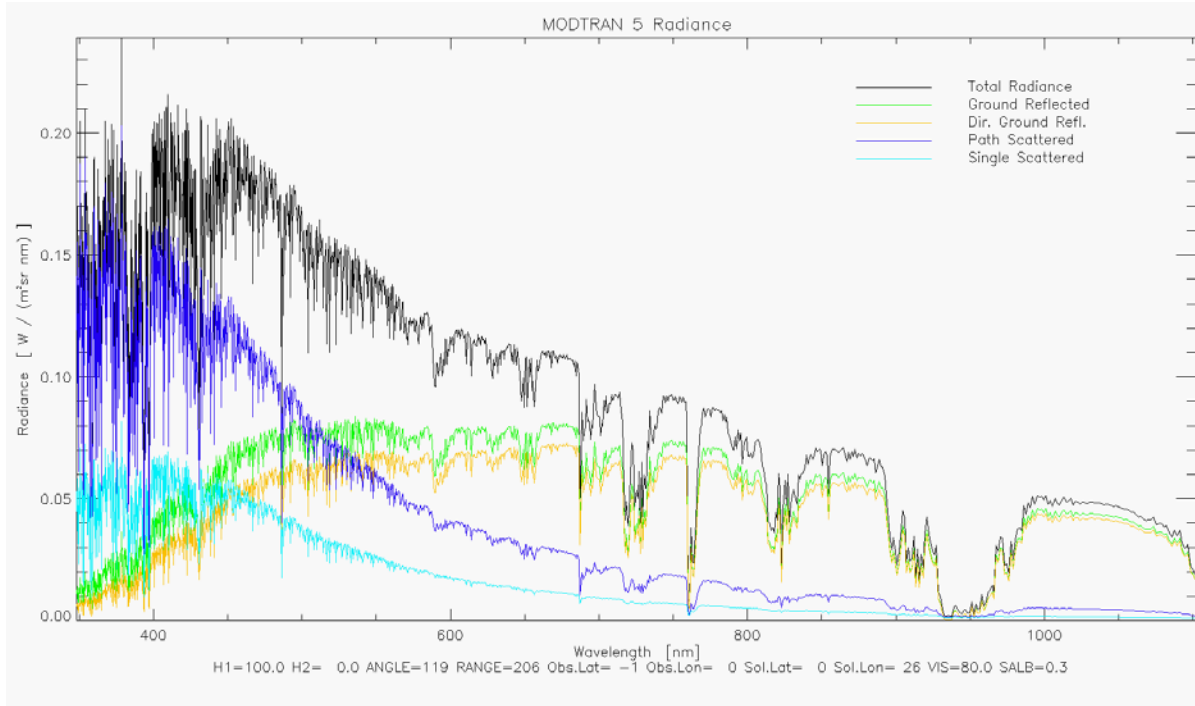


C. MODTRAN RADIANCE PLOTS, 380–1100 NM

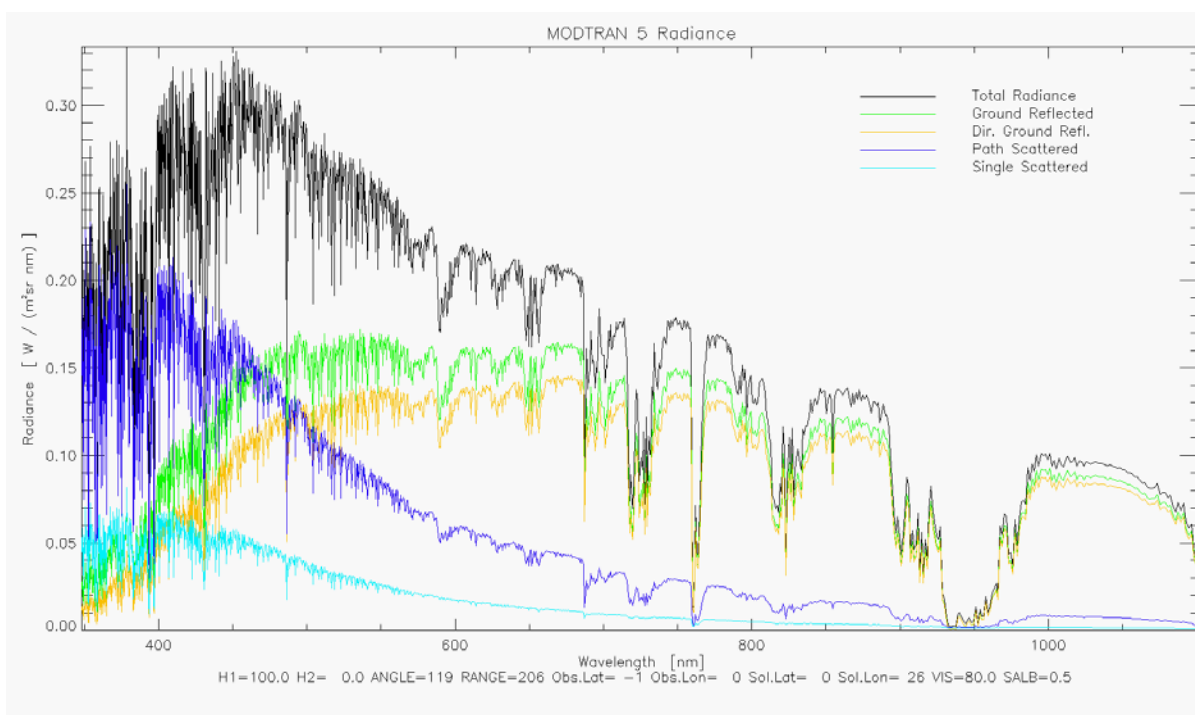
The following charts depict five elements of MODTRAN-generated radiance. The legend for each radiance type is shown in the upper right corner of each chart.



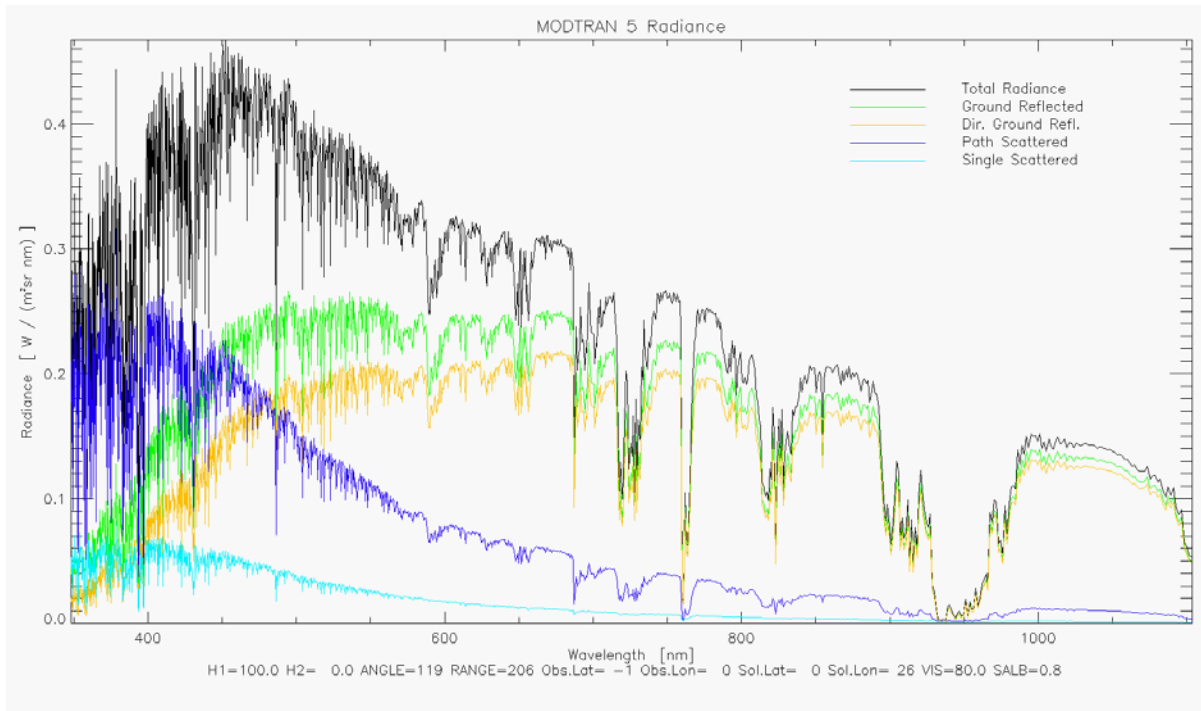
Albedo: 0.01



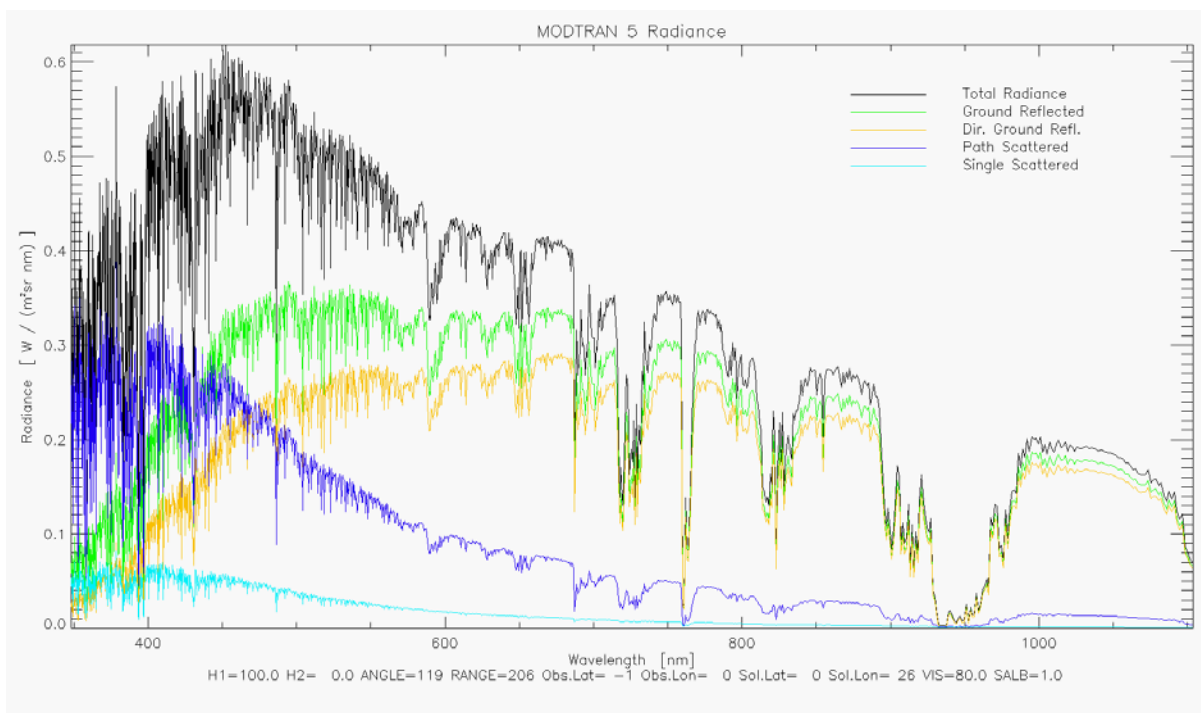
Albedo: 0.25



Albedo: 0.50



Albedo: 0.75



Albedo: 1

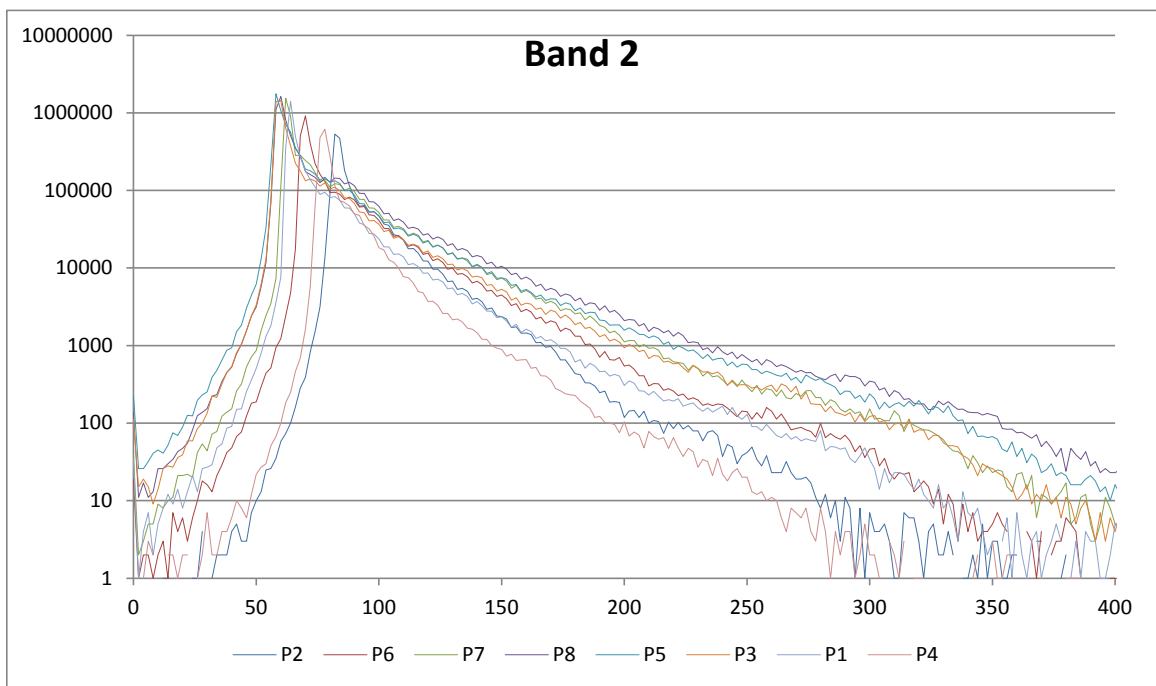
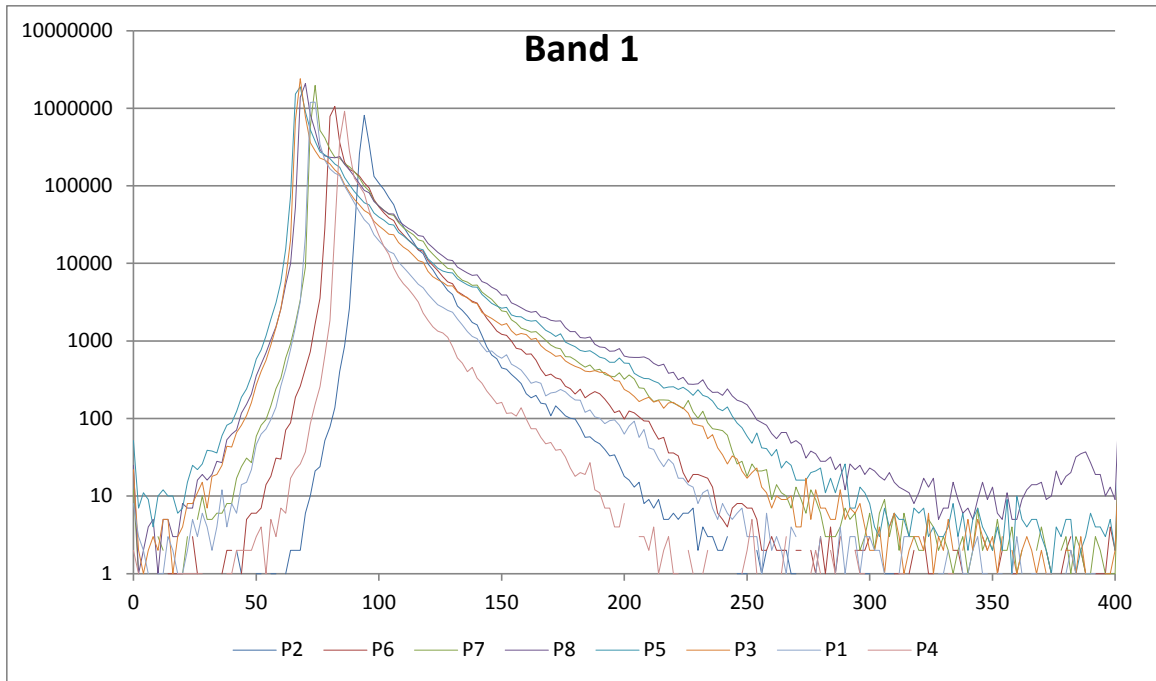
[All charts in Appendix C generated using MODO / ENVI IDL]

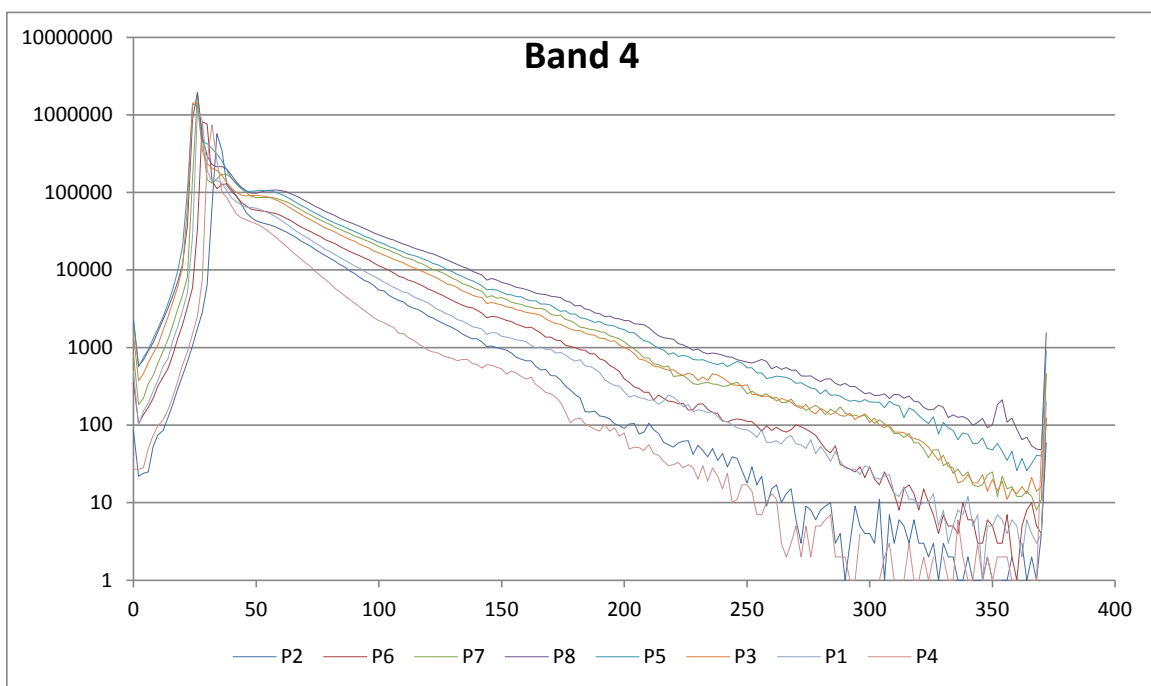
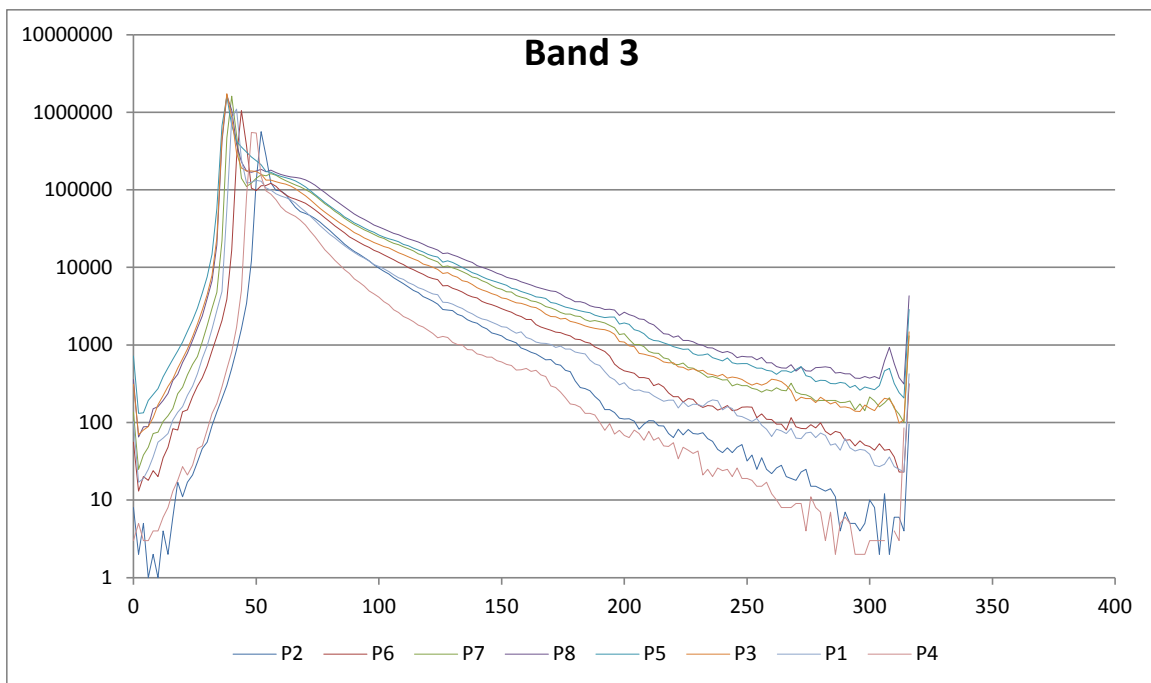
D. IMAGERY HISTOGRAMS BY BAND

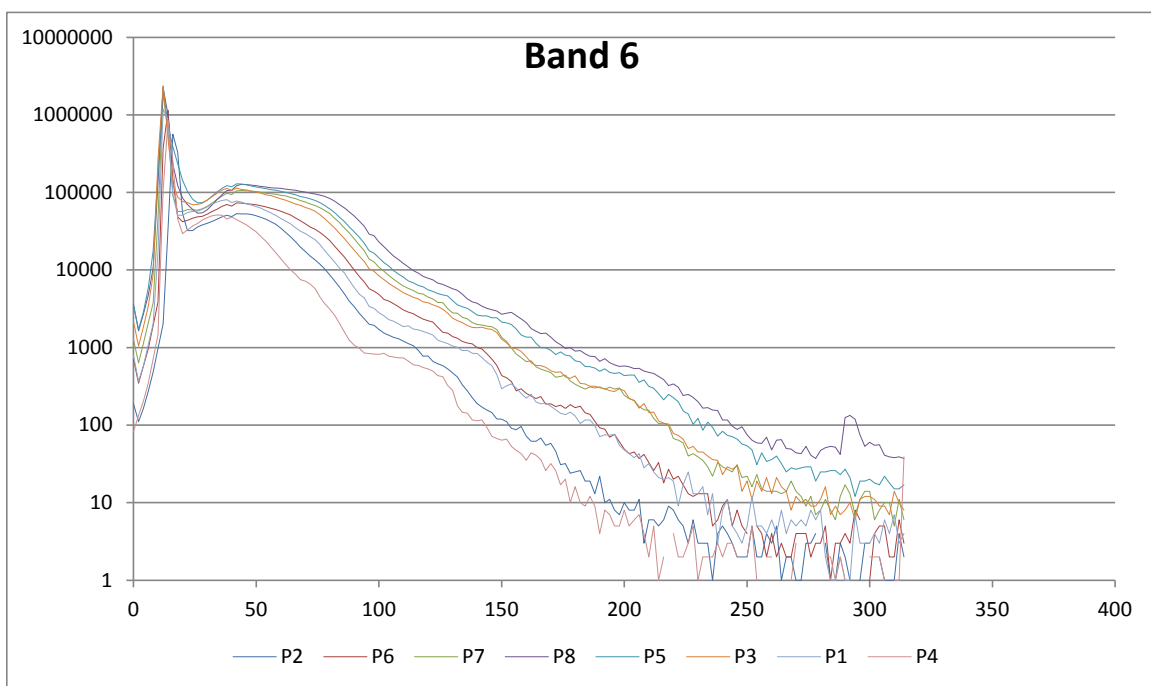
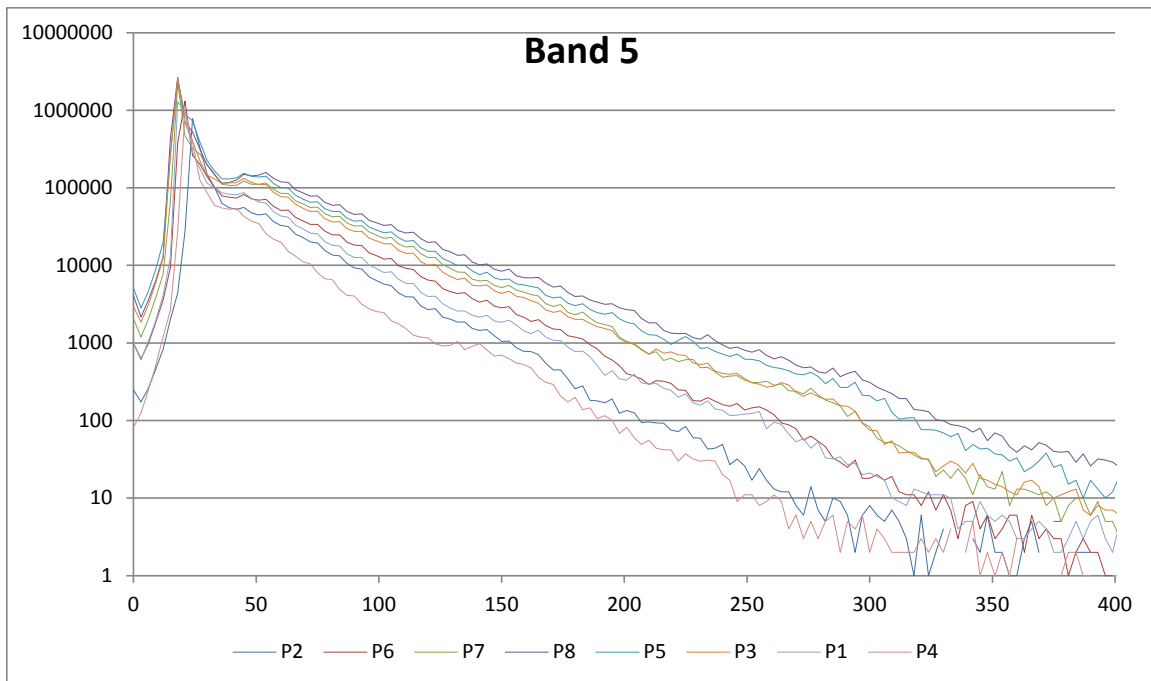
Following the previous multi-angle research referenced in Section II.C.1.b., the following histogram charts are provided. Each chart, generated for each band of the WV-2 sensor, displays the digital number (DN) histograms for each of the eight image geometries used in this thesis.

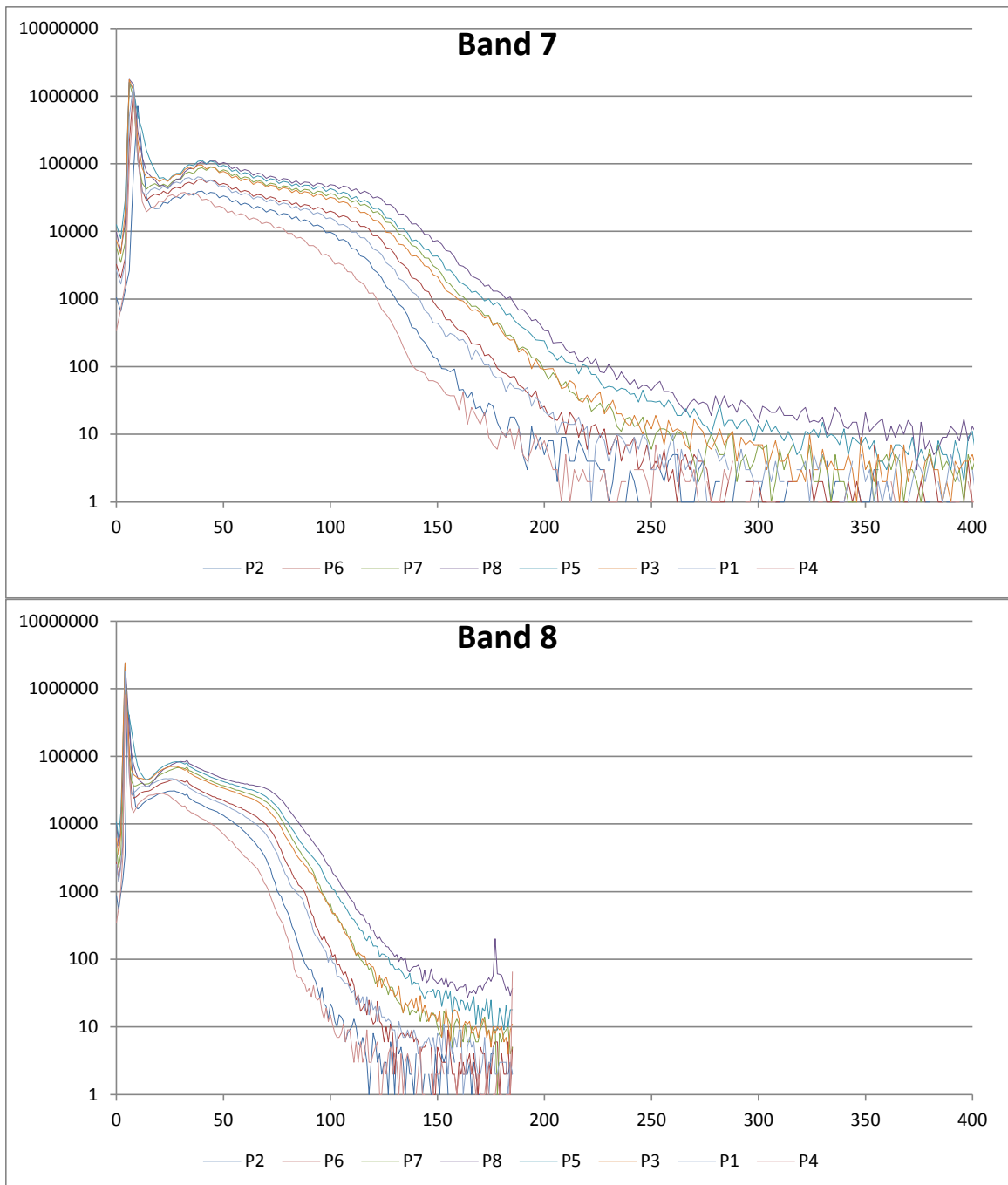
Two trends are noteworthy and can be analyzed with the findings in section IV. First, the peaks seen in the lower DN counts (on the left in each chart), occur at slightly brighter DN values for the off-nadir geometries (P2 and P4) and decrease to a minimum DN value for the most-nadir (P8) geometry. This behavior is an indication of the dominance of atmospheric scattering (path scattered radiance) in the darker pixel regions of the imagery. Second, as DN increases to the maximum plotted for each chart, the image geometry histogram plotlines switch relative to their positions in the first case: most-nadir geometry (P8) has higher DN counts than the off-nadir geometries (P2 and P4). In this case, ground reflected radiance is dominant in the brighter pixels.

[In each chart, x-axis: DN, y-axis: counts]









LIST OF REFERENCES

- Baldrige, A. M., Hook, S. J., Grove, C. I., & Rivera, G. (2009). The ASTER spectral library version 2.0. *Remote Sensing of the Environment*, 113, 711–715.
- Berk, A., Anderson, G. P., Acharya, P. K., & Shettle, E. P. (2011, May). *MODTRAN 5.2.2 user's manual*. Burlington, MA: Spectral Sciences. & Air Force Research Laboratory.
- Brooks, D. (2008, January). *Pyranometer protocol*. (Institute for Earth Science Research and Education). Retrieved from <http://www.instesre.org/Solar/PyranometerProtocol/PyranometerProtocol.htm>
- Budyko, M. I., & Kondratev, K. I. (2010). Atmosphere. In *The great Soviet encyclopedia*. The Gale Group. Retrieved from <http://encyclopedia2.thefreedictionary.com/Atmosphere+composition>
- Canisius, F., Chen, J. M. (2007). Retrieving forest background reflectance in a boreal region from Multi-angle Imaging SpectroRadiometer (MISR) data, *Remote sensing of Environment*, 107: 1-2. 312–321. Retrieved from <http://www.sciencedirect.com/science/article/pii/S0034425706004184>
- Chust, G., Sagarminaga, Y. (2007). The multi-angle view of MISR detects oil slicks under sun glitter conditions, *Remote sensing of Environment*. 107: 1-2. 232–239. Retrieved from <http://www.sciencedirect.com/science/article/pii/S0034425706004445>
- Coburn, C. (2006, January 3). *Measurement of BRDF*. (University of Lethbridge). Retrieved from http://people.uleth.ca/~craig.coburn/brdf/goni_page.htm
- CRISP. (n.d.). *Principles of remote sensing – Centre for remote imaging, sensing and processing, CRISP*. Retrieved from National University of Singapore Center for Remote Imaging, Sensing & Processing (CRISP) website: <http://www.crisp.nus.edu.sg/~research/tutorial/optical.htm>
- Davies, W. H., North, P. R. J., Grey, W. M. F., & Barnsley, M. J. (2010). Improvements in aerosol optical depth estimation using multiangle CHRIS/PROBA images. *IEEE Transactions on Geoscience and Remote Sensing*. 48: 1. 18–24. Retrieved from <http://ieeexplore.ieee.org.libproxy.nps.edu/stamp/stamp.jsp?tp=&arnumber=5256163&isnumber=5356246>

- D'Urso, G., Dini, L., Vuolo, F., Alonso, L., & Guanter, L. (2004). Retrieval of leaf area index by inverting hyper-spectral, multi-angular CHRIS/PROBA data from SPARC 2003. *Proceedings of the Second CHRIS/PROBA Workshop, 28–30 April 2004, ESA/ESRIN, Frascati, Italy (ESA SP–578, July 2004)*. Retrieved from http://earth.esa.int/workshops/chris_proba_04/papers/15_durso.pdf
- Deutsches Zentrum für Luft- und Raumfahrt (DLR). (n.d.) ATCOR Spectral Library [data file]. Licensed to ReSe Applications Schlaepfer for inclusion with MODO software package.
- DigitalGlobe, Inc. (2013, May). *DigitalGlobe's core imagery product guide*. Retrieved from http://www.digitalglobe.com/sites/default/files/DigitalGlobe_Core_Imagery_Products_Guide.pdf
- DigitalGlobe, Inc. (2013, June 3). *Whitepaper–The benefits of eight spectral bands of WorldView-2*. Retrieved from http://www.digitalglobe.com/sites/default/files/DG-8SPECTRAL-WP_0.pdf
- DigitalGlobe, Inc. (2013, June 3). *WorldView-2 datasheet*. Retrieved from http://www.digitalglobe.com/sites/default/files/DG_WorldView2_DS_PROD.pdf
- DigitalGlobe, Inc. (n.d.). *WorldView-2.png*. Retrieved August 9, 2013, from <http://www.digitalglobe.com/sites/default/files/styles/satellite/public/WorldView-2.png>
- ESA. (2011). *Space in Images–2011–10–Agile Proba-1 rolls in its orbit to take images*. Retrieved from http://spaceinimages.esa.int/Images/2011/10/Agile_Proba-1_rolls_in_its_orbit_to_take_images
- ESA. (2013). *Applications–Earthnet online*. Retrieved from ESA–Earthnet Online: <http://earth.esa.int/web/guest/missions/esa-operational-eo-missions/proba/instruments/chris/applications>
- ESA. (2013). *CHRIS–Earthnet online*. Retrieved from ESA–Earthnet Online: <http://earth.esa.int/web/guest/missions/esa-operational-eo-missions/proba/instruments/chris>
- ESA. (2013). *History–Earthnet online*. Retrieved from ESA–Earthnet Online: <http://earth.esa.int/web/guest/missions/esa-operational-eo-missions/proba/history>
- Google Maps. (2013). *Rio de Janeiro*. Retrieved August 31, 2013, from Google Maps: <https://www.google.com/maps?ll=-22.909306,-43.151808&spn=0.053366,0.104628&t=p&z=14>
- Griffiths, D. J. (1999). *Introduction to electrodynamics* (3rd ed.). Upper Saddle River, New Jersey: Pearson Education.

- Halliday, D., Resnick, R., & Walker, J. (2011). *Fundamentals of Physics* (9th ed.). Jefferson City: John Wiley & Sons.
- ITT Visual Information Systems, Inc. (2009, August). *Atmospheric correction module: QUAC and FLAASH user's guide*. Retrieved from http://www.exelisvis.com/portals/0/pdfs/envi/Flaash_Module.pdf
- Jaques, S. L., & Prah, S. A. (1998). *Irradiance*. (Oregon Graduate Institute). Retrieved from <http://omlc.ogi.edu/education/ece532/class1/irradiance.html>
- Jensen, J. R. (2007). *Remote sensing of the environment: An earth resource perspective* (2nd ed.). Upper Saddle River, NJ: Pearson Education, Inc.
- Lee, K. R. (2012). *Using multi-angle WorldView-2 imagery to determine ocean depth near Oahu, Hawaii*. (Master's thesis, Naval Postgraduate School). Retrieved from http://calhoun.nps.edu/public/bitstream/handle/10945/17399/12Sep_Lee_Krista.pdf?sequence=1
- Lucht, W., & Schaaf, C. (2006, July 12). *BRDF explained*. (Boston University). Retrieved from <http://www-modis.bu.edu/brdf/brdfexpl.html>
- McConnon, C. L. (2010). *High spatial resolution bidirectional reflectance retrieval using satellite data*. (Master's thesis, Naval Postgraduate School). Retrieved from http://calhoun.nps.edu/public/bitstream/handle/10945/5102/10Dec_McConnon.pdf?sequence=1
- NASA JPL. (2013). *MISR: EOS and Terra*. Retrieved from MISR–Multi-angle Imaging Spectroradiometer: <http://www-misr.jpl.nasa.gov/Mission/eosTerra/>
- NASA JPL. (2013). *MISR: Peer-reviewed publications*. Retrieved from MISR–Multi-angle Imaging Spectroradiometer: <http://www-misr.jpl.nasa.gov/publications/peerReviewed/>
- NASA JPL. (2013). *MISR: Viewing angles*. Retrieved from MISR–Multi-angle Imaging Spectroradiometer: <http://www-misr.jpl.nasa.gov/Mission/misrInstrument/viewingAngles/>
- Nave, C. R. (2000). *Blue sky and Rayleigh scattering*. (Georgia State University). Retrieved from <http://hyperphysics.phy-astr.gsu.edu/hbase/atmos/blusky.html>
- Nicodemus, F. E., Richmond, J. C., Hsia, J. J., Ginsberg, I. W., & Limperis, T. (1977, October). Geometrical considerations and nomenclature for reflectance. *NBS monograph*. Washington, DC. Retrieved from <http://graphics.stanford.edu/courses/cs448-05-winter/papers/nicodemus-brdf-nist.pdf>

- Olsen, R. C. (2007). *Remote sensing from air and space*. Bellingham, WA: SPIE–The International Society for Optical Engineering.
- Olsen, R. C., Kim, A. M., McConnon, C. (2011). High spatial resolution bidirectional reflectance retrieval using satellite data. *Proc. SPIE 8048 80480W-1, Algorithms and Technologies for Multispectral, Hyperspectral, and Ultraspectral Imagery XVII*. Retrieved from http://proceedings.spiedigitallibrary.org/data/Conferences/SPIEP/62014/80480W_1.pdf
- Ontar Corporation. (2009, August). *PcModWin manual*. North Andover, MA: Ontar Corporation.
- Saha, K. (2008). *The earth's atmosphere: Its physics and dynamics*. Berlin: Springer.
- Salby, M. L. (1996). *Fundamentals of atmospheric physics*. San Diego, CA: Academic Press.
- Sanz Fernández de Córdoba, S. (2013). *100km altitude boundary for astronautics*. (Fédération Aéronautique Internationale). Retrieved from FAI Portal: <http://www.fai.org/icare-records/100km-altitude-boundary-for-astronautics>.
- Schaepman-Strub, G., Schaepman, M. E., Painter, T. H., Dangel, S., & Martonchik, J. V. (2006). Reflectance quantities in optical remote sensing—Definitions and case studies. *Remote sensing of environment*, 103:1, 27–42. Retrieved from <http://www.sciencedirect.com/science/article/pii/S0034425706001167>
- Schott, J. R. (1997). *Remote sensing: The image chain approach*. New York: Oxford University Press.
- Serway, R. A., Moses, C. J., & Moyer, C. A. (1989). *Modern physics*. Philadelphia: Saunders College Publishing.
- Updike, T., & Comp, C. (2010, November 1). *Radiometric use of WorldView-2 imagery*. Retrieved from http://www.digitalglobe.com/sites/default/files/Radiometric_Use_of_WorldView-2_Imagery%20%281%29.pdf

INITIAL DISTRIBUTION LIST

1. Defense Technical Information Center
Ft. Belvoir, Virginia
2. Dudley Knox Library
Naval Postgraduate School
Monterey, California